UNIVERSITY OF CALIFORNIA

Santa Barbara

A role for strain-based mechanical feedback in establishing the myosin distribution driving *Drosophila* germ-band extension

A dissertation submitted in partial satisfaction of the

requirements for the degree

Doctor of Philosophy

in

Biochemistry and Molecular Biology

by

Hannah J Gustafson

Committee in charge:

Professor Sebastian Streichan, Chair

Professor Denise Montell

Professor Joel Rothman

Professor Boris Shraiman

June 2022

The dissertation of Hannah J Gustafson is approved.

_____
Denise Montell

_____
Joel Rothman

_____
Boris Shraiman

_____
Sebastian Streichan, Committee Chair

June 2022

A role for strain-based mechanical feedback in establishing the myosin distribution driving *Drosophila* germ-band extension

Hannah Jane Gustafson

Acknowledgements

There are a number of people that have been instrumental, both professionally and personally, to this dissertation; it would not have been possible without them, and for that I would like to extend my gratitude to the following people:

First and foremost, my advisor, Sebastian, whose guidance, support, and mentorship has been fundamental to this dissertation and my time as a graduate student. Having just joined the UCSB Physics Department, Sebastian took me on as a graduate student seeking a change from a lab which was not properly aligned with my professional and personal goals. Dedicated to supplement my understanding of the biological world with relevant concepts from physics and quantitative methods, Sebastian spent many hours tutoring me in the unfamiliar landscape of fluid mechanics and helping me troubleshoot MatLab scripts. I am also grateful for his financial support to allow me to focus on developing these new concepts in the context of this dissertation. Finally, for teaching me the fundamentals of light sheet microscopy, working with embryos, and data processing.

My committee members: Denise Montell, Joel Rothman, and Boris Shraiman, who made time in their incredibly busy schedules to serve on yet another committee and provided invaluable feedback and insight.

Members of the Streichan lab, past and present, who have provided useful discussions, problem solving support, and a positive lab environment. In particular, to Sophie, who was so helpful to me when starting work with fruit flies, always willing to provide additional assistance, and above all a kind presence.

Members of the Dogic lab who have shared equipment, lab and office space, and many lunches.

My fellow BMSE students, in particular my cohort, for their comradery during courses and TAships, FNS, and social activities.

Alessandro Mongera, who was pivotal in my introduction to research and responsible for my early training. I appreciate your mentorship, advocacy, and guidance over the years.

My siblings, Jack, Maximus and Ella, and my friends, in particular Masha, Claire, and Alex, who have supported me during my many years in graduate school, in some cases without fully understanding what I have been doing these years or why. I am forever grateful for your patience and understanding with my busy schedule and frequent absence from family or social events and for your love and friendship.

Finally, my partner Eric, who has stood by me during some of the most challenging times. It is difficult to list the ways that you have helped me over these few years, from teaching me something about work life balance and taking advantage of life in Santa Barbara, to making me grilled cheeses on the hard days. Suffice to say, it is likely that I would not be writing this dissertation today if it were not for you. And of course for your influence in getting our kitties Samira and Ember, who have been a constant source of joy, entertainment, and comfort, as well as my company during many long hours working from home. I have cherished the life we have built as a family and look forward to how it will grow beyond the confines of graduate school.

Curriculum Vitae

Hannah J. Gustafson

Education

Ph.D. Biochemistry and Molecular Biology, UCSB — Sept 2015 – June 2022

B.S. Biological Sciences, UCSB, *Magna Cum Laude* — Sept 2010 – June 2014

Language Immersion Study Abroad, University of Granada, Spain — Sept 2012 - July 2013

Publications

H.J. Gustafson, N.H. Claussen, S. De Renzis, and S.J. Streichan. 2022. Patterned mechanical feedback established a global myosin gradient. Under review.

M.F. Lefebvre, N.H. Claussen, N.P. Mitchell, **H.J. Gustafson**, S.J. Streichan. 2022. Geometric control of Myosin-II orientation during axis elongation. Submitted for publication.

A. Mongera, M. Pochitaloff, **H.J. Gustafson**, G.A. StookeVaughan, P. Rowghanian, S. Kim, and O. Campàs. 2022. Mechanics of the cellular microenvironment as probed by cells in vivo. Under review.

A. Mongera, P. Rowghanian, **H.J. Gustafson**, E. Shelton, D.A. Kealhofer, E.K. Carn, F. Serwane, A.A. Lucio, J. Giammona, and O. Campàs. 2018. A fluid-to-solid jamming transition underlies vertebrate body axis elongation. Nature.

Fellowships

Mellichamp Fellowship for Graduate Students in Systems Biology and Bioengineering — 2016

Professional employment

Graduate student researcher: Streichan Lab, UCSB — Jan 2018 – Jun 2022
Teaching Assistant: KITP Summer School 'Form, Fate, and Function' — Summer 2019
Teaching Assistant: Cell Biology — Fall 2017
Graduate student researcher: Campas Lab, UCSB — Jul 2016 – Sept 2017
Teaching Assistant: Introductory Biology Laboratory III — Spring 2016
Teaching Assistant: Introductory Biology Laboratory I — Fall 2015
Junior specialist: Campas Lab, UCSB — Jun 2014 – Sept 2015

Abstract

A role for strain-based mechanical feedback in establishing the myosin distribution driving *Drosophila* germ-band extension

by

Hannah Gustafson

The problem of understanding the complex sequence of morphogenetic processes that transform a single cell zygote into a fully formed and functional organism is at the heart of the field of developmental biology. Early progress in the field relied on detailed observations of the developing embryo to produce qualitative descriptions of the various morphogenetic processes, establishing a rough timeline for development and the relative sequence of events. Later, extensive genetic screens allowed researchers to identify critical genes in morphogenetic processes based on the observed defects, and with many iterations carefully piece together the genetic cascades that direct development. Nevertheless, shape is inherently a problem of mechanics, and therefore a thorough view of morphogenesis requires an understanding of the intimate interplay between genetics and mechanics. Although an appreciation for this role of the physical aspects of developmental biology predate our knowledge of genetics, its characterization has been much slower that its genetic counterpart.

Perhaps best characterized genetically is the example of the embryogenesis of *Drosophila melanogaster*, which therefore offers an ideal context within which to study the role of mechanics. In this dissertation, we aim to take advantage of the detailed genetic foundation to better understand the role of mechanics in development, in particular during the period of early gastrulation in the fruit fly. Extensive studies of the genetics and preliminary characterization

of the mechanics have been undertaken for the morphogenetic processes associated with this developmental stage, namely ventral furrow formation and germ-band extension.

We aim to build off this previous work utilizing *in toto* multi-view light sheet microscopy to image global dynamics of the developing embryo and take advantage of image processing techniques to allow rigorous quantitative analysis of strain and myosin rates. With these methods, we identify a strong correlation between strain and myosin dynamics across the embryo surface. We confirm the relationship at the level of single junctions with high spatiotemporal resolution confocal microscopy and demonstrate that a simple physical model with mechanical feedback as a key feature recapitulates the single junction observations.

We next utilize an optogenetic construct to pattern actomyosin contractility in order to induce physiologically relevant and minimally invasive ectopic strain rates and measure the resulting changes to the myosin dynamics. By altering the pattern of activation, we show that not only does a strain based mechanical feedback mechanism recruit myosin *in vivo*, but we further show that this mechanism is isotropic within the cell but spatially modulated along the D-V axis. We then adapt our model to predict the myosin distribution at the tissue scale and show that incorporating this D-V modulation of feedback strength provides an accurate prediction of the myosin profile.

Finally, we demonstrate the importance of this feedback mechanism for normal development by analyzing genetic mutants defective for a major strain generating process: ventral furrow formation. We find that these mutants have significantly reduced strain rates and proportional reductions in the myosin distribution. Notably, these embryos have an equivalent reduction in the rate of germ-band extension, which is known to depend on the myosin distribution, indicating the developmental relevance of this mechanism.

Contents

List of Figures

Chapter 1:

Introduction

A fundamental question in the study of developmental biology has been that of morphogenesis, or the process by which form is acquired, both on the scale of individual organs or structures and on the scale of the whole animal. The formation of an animal's body plan is the cumulation of many individual processes, each contributing to the final form. The initial strategy of developmental biology therefore, was to understand each of these processes independently. This first involved making detailed observations about the various steps in the process at the tissue scale, followed by the cellular scale, as permitted by advancements in microscopy. Later, the understanding of the critical role for genetics in instructing these processes opened a whole new approach in the field. The ability to induce mutations at random followed by large scale screens to identify phenotypic variants led to the identification of gene products necessary for particular morphogenetic processes. One salient example is the use of this strategy in

Drosophila melanogaster to identify the genetic cascades setting up the coordinate system of the embryo, for which Christiane Nusslein-Volhard and Eric Wieschaus were awarded the Nobel prize. Their work elucidated how maternal factors establish the two orthogonal embryonic axis to create a system in which each cell in the embryo has a unique identity which determines its fate[1] and served as the foundation for our genetic understanding of embryonic development in *Drosophila*.

Piecing together the genetic cascades downstream of positional information that direct cell fate led to the next major question: how do these pathways actually encode shape? Shaping tissues requires coordinated changes at the level of single cells to produce patterns of force generation and mechanical properties at the scale of tissues to enable tissue deformation in accordance with the target shape. Therefore, bridging gene networks with discrete shape changes requires an understanding of the ways that these physical properties are determined by cellular components downstream of genetic pathways. Consequently, the emerging field of Mechanobiology aims to address precisely this question. Significant progress has been made in identifying the molecules that tune a cell's mechanical properties, allow it to generate force, and transmit that force across tissues. Myosin motors are an example of one such molecule that is widely employed in a variety of contexts during development due to its ability to not only generate large amounts of force, but by nature of being part of the cytoskeleton, is linked to other cytoskeletal components that allow this force to be transmitted to other cells.

An understanding of force transmission in biological tissues combined with the growing prevalence of identified mechanotransductive processes raised more questions for our understanding of morphogenesis: how does the generation of force in one region affect the behavior of cells in another? And what role if any does this play in development? Attempting

to answer these questions requires a well characterized system in which the direct effects of genetic pathways can be distinguished from mechanosensitive responses, in order to determine their relative contributions to the larger process. Embryonic development of *Drosophila* melanogaster, and in particular early gastrulation, provides one such system in which the genetic cascades are largely characterized and significant progress understanding the downstream changes to tissue properties driving morphogenesis has been made. It is within this context that the work described herein is situated, and therefore we begin with a brief overview of the problem at hand.

1.1 The problem of morphogenesis

Morphogenesis, literally "the origin of form", is the process by which structures, organs, and whole animals acquire their shape and represents a major area of interest within the field of developmental biology. Each animal begins as a single fertilized cell that progressively attains its characteristic body plan over the course of development through a complex series of cell behaviors that shape the developing organism. Great strides have been made to understand the genetic instructions followed during development, yet our understanding remains incomplete without the connection to the tissue mechanics that ultimately drive shape change. The mechanics of living systems has therefore become a widely growing area of research that has begun to make invaluable contributions to further our understanding of development.

1.1.1 Insights from developmental biology: genetic patterning

From early transplantation experiments with animal embryos, it became clear that the identity of cells become fated at particular developmental stages and specific instructions based on

positional information must direct that unique identity. Understanding how an animal acquires its shape, therefore, begins with the fundamental question of how the body axes are determined, as later decisions rely on the positional information provided by these axes. The embryonic axes: Anterior-Posterior (A-P) or head-tail, Dorsal-Ventral (D-V) or back-belly, and Left-Right, establish a coordinate system in the embryo giving each cell a unique position and associated identity. This positional information is critical for determining the specific set of instructions followed by each cell and accordingly determines the behaviors adopted by the cell as it moves through the developmental program. Great strides have been made to tease apart the factors specifying different cell fates during development and at what stages these fates become sealed. An excellent example of an organism for which extensive screens have been carried out to elucidate the genetic cascades governing development is the embryo of *Drosophila melanogaster*.

In the fruit fly embryo, the A-P and D-V embryonic axes are first established during egg formation. Maternally deposited factors during oogenesis pre-pattern the embryonic axes before fertilization of the egg even occurs. The D-V axis is determined by the activity of the Dorsal gene product[2] (Figure 1.1). Although expressed in all cells around the D-V axis, Dorsal forms a gradient of nuclear localization on the ventral side of the embryo[3], where is acts as a transcription factor for ventral specifiers *twist* and *snail* and represses dorsal specifying genes *decapentaplegic* and *zerknüllt*[1,4]. The cascade that results in Dorsal nuclear translocation only in ventral cells begins with a symmetry breaking event in the developing oocyte in which the oocyte nucleus moves from a central posterior region of the oocyte to a dorsal anterior position[5,6]. This specifies the overlying follicular epithelium to dorsal fates through the activity of the *gurken* gene product, which is restricted to the dorsal side due to its fast degradation

time[7]. Translation of *gurken* activates a pathway that prevents Dorsal from entering the nucleus, thus creating the Dorsal gradient upstream of *twist* and *snail*.

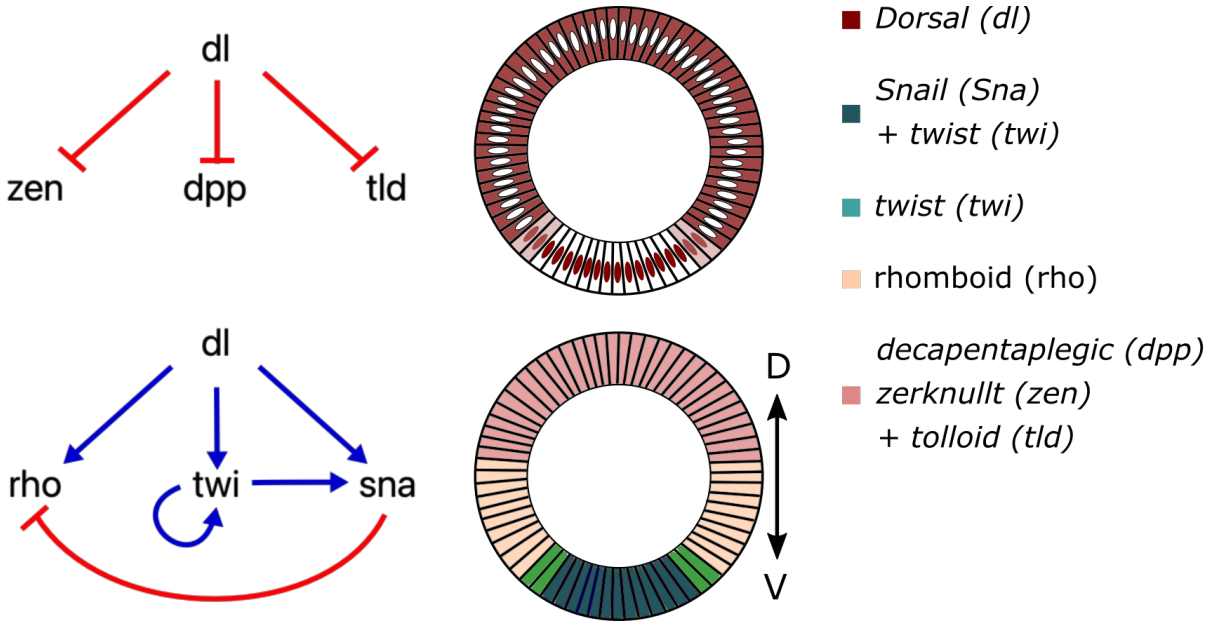

Figure 1.1: Establishing Dorsal (D)-Ventral (V) polarity in the *Drosophila* embryo
Left: Genetic pathways downstream of Dorsal that inhibit dorsal fate determinants (top) and activate ventral fate determinants (bottom). Right: Gradient of Dorsal nuclear localization establishes the D-V axis in the embryo (top). The genetic interactions shown to the left combined with the Dorsal gradient pictured at top right leads to the expression patterns of genes determining ventral (*twist* and *snail*), lateral (*rhomboid*) and dorsal (*decapentaplegic*, *zerknüllt*, and *tolloid*) fates.

In the case of the A-P axis, positional information is provided by gradients in the maternally deposited factors Bicoid and Nanos[8] (Figure 1.2). Both *bicoid* and *nanos* mRNAs are synthesized by nurse cells and transported into the oocyte, but each is tethered to one end of the embryo by various binding factors. *Bicoid* mRNA is anchored to the anterior pole, where is it translated. The Bicoid protein freely diffuses in the embryo but has a finite lifetime, leading to a gradient in protein levels. Similarly, *nanos* mRNA is bound to the posterior pole and translated, forming an opposing gradient. Bicoid and Nanos further refine the A-P axis through *hunchback* and *caudal*, whose mRNAs are expressed uniformly within the oocyte. Bicoid

activates *hunchback* mRNA translation while inactivating *caudal* mRNA translation; Nanos inactivates *hunchback* mRNA translation. The combined effects produced a region of high Hunchback at the anterior, which drops off gradually towards the posterior, and a gradient of Caudal that is slightly broader than that of nanos. Together with the terminal factor Torso, these proteins establish the gap genes expression profiles, whose complicated activating and repressing interactions[9] form the striped expression patterns of the pair-rule genes (PRGs) such as *even-skipped*[10,11] (Figure 1.2, right). The PRGs in turn specify segment polarity genes and Toll-like family receptors (TLRs)[12], as well as setting up the unique cell identities along the A-P axis. In most cases, the downstream genetic cascades have been largely worked out, yet much is left to be understood about how these pathways relate to the physical changes associated with the cell identity.

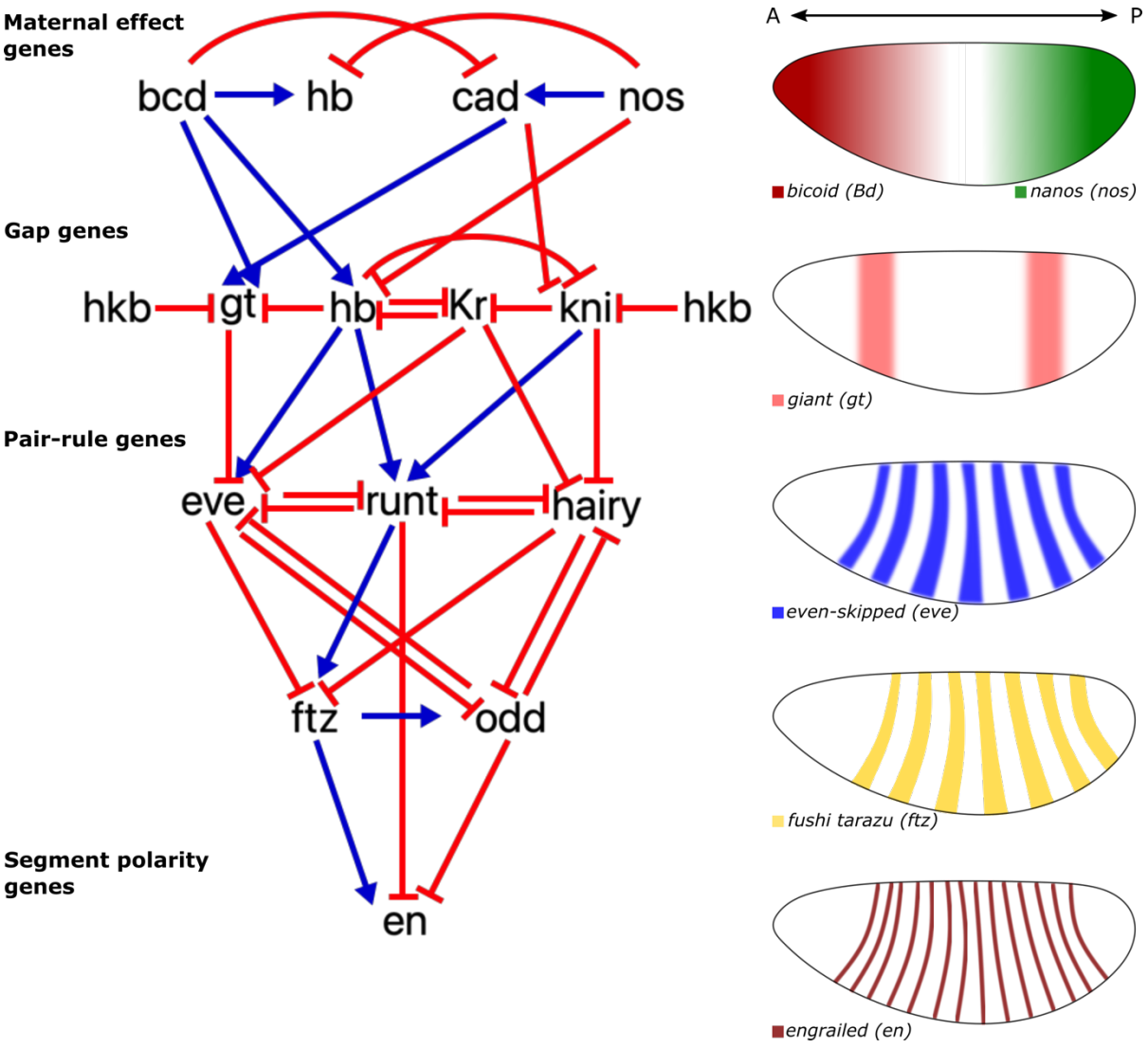

Figure 1.2: Establishing the Anterior (A)- Posterior (P) axis in the *Drosophila* embryo
Left: Simplified genetic cascade responsible for setting up the A-P axis. Blue arrows represent activating interactions while red lines represent inhibition. This refinement of positional information proceeds through a hierarchy of gene activity, beginning with the maternal effect genes *bicoid* (bcd), maternal *hunchback* (hb), *caudal* (cad), and *nanos* (nos). These interactions establish anterior and posterior gradients that then act at the level of the gap genes to establish the expression patterns of *huckebein* (hkb), *giant* (gt, shown), zygotic *hunchback* (hb), *Kruppel* (Kr), and *knirps* (kni). Pair-rule genes are at the next level and their regulation by gap genes and their interactions among themselves lead to stripes of expression along the A-P axis. Shown in the network are *even-skipped* (eve), *runt*, *hairy*, *fushi tarazu* (ftz) and *odd-paired* (odd), while the remaining pair-rule genes are not shown for simplicity. Finally, pair-rule genes establish segment polarity gene expression, which mark the anterior or posterior, as with *engrailed* (en), boundaries of each of the 14 body segments of the embryo, which correspond to the adult segments. Right: Example expression patterns of a subset of A-P patterning genes at different regulatory levels. From top to bottom these are: Bicoid and Nanos, *giant, even-skipped*, *fushi tarazu*, and *engrailed*.

1.1.2 Mechanics of tissues: bridging genes and the emergence of shape

The acquisition of shape is inherently a physical problem; deformation of biological tissues as with inert materials requires spatially patterned force production and/or mechanical properties. A thorough picture of morphogenesis, therefore, requires bridging the genetic pathways upstream of morphogenetic movements with the tissue mechanics that govern the final form. While it is intuitive that genetic pathways must be upstream of the cellular components governing physical properties, exactly which cellular components they are and how they affect the mechanical properties are less well understood[13]. Consequently, although the instructions upstream of the morphogenetic movements are often known, the specific ways that the cell translates these instructions into changes in cell behavior, and in particular those behaviors related to physical properties, remains poorly characterized.

Shaping tissues requires the generation of force, and in particular, in ways that produce non-uniform strains. There are two mechanisms to do so that can be utilized alone or in combination: application of a non-uniform force or application of force to a tissue of non-uniform material properties. It is therefore clear that the developing embryo must carefully regulate both force generation and mechanical properties in order to obtain the characteristic shape, as morphogenetic processes often build off the outcomes of previous events, and any misregulation can have devastating effects to the final form. Previous work in a variety of systems have demonstrated how patterned mechanical properties can play a critical role in determining the final shape[14], while others have shown the importance of graded or otherwise spatially varying force generation to determine shape[15,16]. In many cases, the dysregulation of

these patterned properties can be directly associated to malformations, including the relationship to known developmental defects.

As a result of the growing recognition for the importance mechanics, recent years has seen a significant increase in the research aimed at uncovering the connection between genetic and mechanics[17,18]. One such area of research is dedicated to measuring the properties of cells and attributing these properties to the underlying cellular structures or components. For example, techniques like AFM, micropipette aspiration and microindentation, magnetic tweezers, and myriad others, have begun characterizing the mechanical properties of biological tissues[19]. By perturbing various cellular components in combination with these techniques, it is possible to determine how particular molecules influence the mechanical properties of the cell. A second, complementary approach has focused on characterizing the forces generated by cells and the molecular components responsible[20,21]. There are a several strategies employed by cells to generate force, and one widely studied example, particularly for its role in shaping tissues, is actomyosin contractility[22–24].

1.2 Non-muscle myosin II and its role in development

Myosin is a motor protein capable of translating actin filaments relative to one another, which when coupled to the membrane, cell-cell adhesion complexes, or cell-substrate adhesion complexes, results in changes to cell shape[25]. Therefore, the distribution and activity of myosin, actin, and other cytoskeletal components have an important role in determining how individual cells change shape[22,25]. It is the collective behaviors of many cells, as well as force transmission through cell-cell contacts, therefore that leads to changes at the tissue scale.

1.2.1 Myosin motor function

Myosins are a family of actin associated motor proteins that convert chemical energy from ATP into mechanical work through the action of the motor domain[26]. While there are a variety of myosin motors with varying functions, we focus on the conventional myosin group known as class-2 myosins, which includes muscle myosin II, widely known for its role in muscle contraction, as well as non-muscle myosin II, a myosin motor known to play an important role in force generation in non-muscle cells and the myosin studied herein[27].

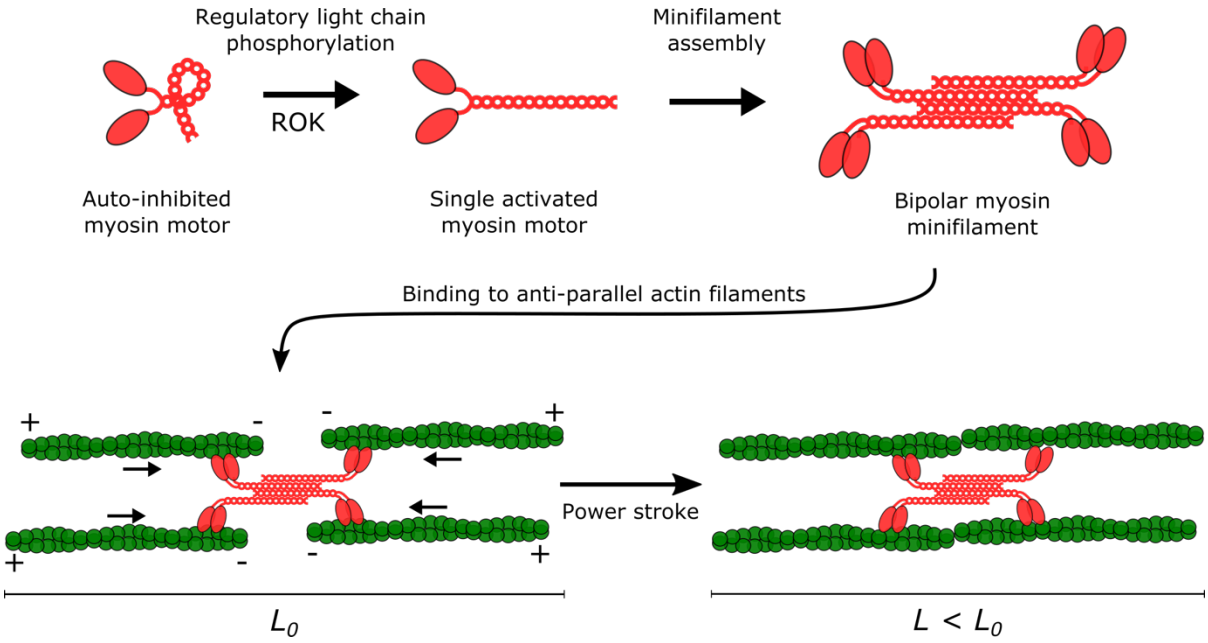

Figure 1.3: Myosin phosphorylation, minifilament assembly, and contractility
Top: Myosin motors form an autoinhibitory loop structure when in an inactive state in the cytoplasmic pool. Phosphorylation of the regulatory light chain by one of the associated kinases (here we focus on ROK) releases the motor from the inactive state and converts it to the active state. Activated myosin can associate with other myosin motors through tail-tail interactions to form bipolar minifilaments. Bottom: Myosin minifilaments can bind and cross-link various actin filaments. Anti-parallel arrangements of actin filaments resembling the structure of a sarcomere have the greatest potential for contractility.

The functional unit of a class 2 myosin motor is a hexamer consisting of two heavy chains, two essential light chains, and two regulatory light chains[23,26]. Each heavy chain has a globular actin binding head with ATPase activity and a tail forming a coiled-coil rod through which it interacts with the tail of the other heavy chain. These head and tail domains are

connected by the lever domain, and the lever domain of each heavy chain is associated with a pair of essential and regulatory light chain monomers. The rod domains of these hexamers can associate with the rod domains of oppositely oriented hexamers to form bipolar minifilaments[28,29] (Figure 1.3). The bipolar minifilaments are able to bind multiple actin filaments and can therefore serve as either crosslinkers or can use the work from ATP energy to translate the actin filaments, leading to contraction[23,30] (Figure 1.3).

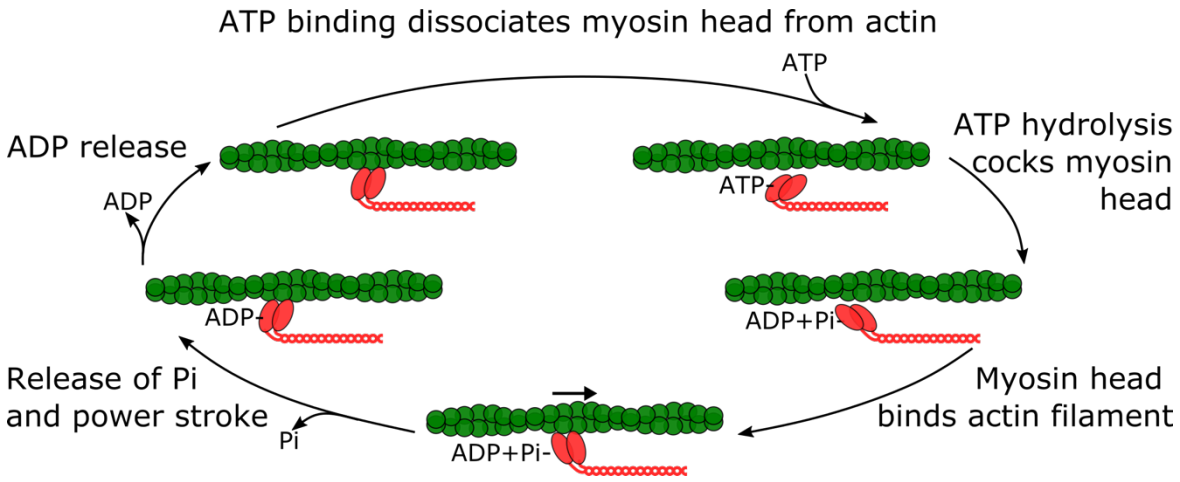

Figure 1.4: Myosin power stroke cycle converts chemical energy to mechanical work Clockwise from top left: myosin in its low energy state is bound to actin. Association of a new ATP molecule with the binding site causes the myosin-actin complex to dissociate. ATP hydrolysis cocks the myosin head to its high energy state. The myosin head then binds the actin filament at a new location. The power stroke occurs as the release of phosphate returns the myosin head to its low energy state, translating the associated actin filament as it does. Finally, ADP is released from the myosin head and the cycle can repeat.

The movement of actin filaments occurs via a five step process during which the head domain converts chemical energy from ATP hydrolysis into mechanical work[31]. These steps are: ATP hydrolysis, actin binding, power stroke, ADP release, and ATP binding (Figure 1.4). In the first step, ATP hydrolysis returns the head domain to the resting state. This allows for a high affinity interaction between the myosin head and actin filament, promoting the second step of binding or cross bridge formation. Once myosin has bound actin, the previously hydrolyzed phosphate is released, allowing a conformational change of the motor head,

resulting in the characteristic power stroke that causes sliding of actin filaments and produces work. In the next step, ADP dissociates, but myosin remains bound to actin. Finally, to restart the cycle, ATP binds to the myosin head, breaking the interaction between myosin and actin and allowing the cycle to repeat. The power stroke cycle is regulated by numerous factors, including the phosphorylation state of the myosin regulatory light chain and the organization of the actin cortex.

1.2.2 Regulation of myosin activity

Additionally, there are many regulatory elements determining a myosin motor's competence to enact its power stroke. There is a large cytoplasmic pool of myosin present in the cell at any time, similar to the pool of G-actin, which serves as a reservoir of pre-made myosin motors that can be utilized when the cell's activity demands quick addition of myosin motors to the cortex. When in this cytoplasmic pool, myosin motors are present in an inactivated state: the single motors form an auto-inhibitory loop, preventing them from being able to associate with other myosin motors to form bipolar minifilaments or with actin filaments[23,32] (Figure 1.3). Release from auto-inhibition relies on the activity several kinases that phosphorylate the regulatory light chain, breaking the loop and activating the myosin motor for minifilament assembly and actin binding[33]. For the purpose of this dissertation, we focus primarily on the activity of Rho-associated Kinase (ROK), which is one such kinase activating myosin[34–36]. The activity of ROK is in turn governed by the activity of the upstream activator Rho, which binds ROK to increase its kinase activity[37]. Rho is a membrane anchored small GTPase that activates actomyosin contractility by activating myosin through ROK and promoting actin polymerization through the formin Diaphanous (Dia)[38,39] (Figure 1.5).

Rho is in its active state when it is both membrane associated and GTP bound, a state that is primarily determined by the relative activity of three main classes of molecules: Guanine nucleotide exchange factors (GEFs), GTPase-activating proteins (GAPs), and Guanine nucleotide disassociation inhibitors (GDIs)[40]. Rho cycles between GTP and GDP bound states; Rho is active in its GTP bound state and inactive in its GDP state (Figure 1.5). GEFs activate Rho by facilitating the removal of GDP, opening up the binding site for another GTP molecule to bind[41]. As a GTPase, Rho has the basic function to hydrolyze GTP to GDP, leading to its own activation. Nevertheless, the intrinsic GTPase activity is low and efficient hydrolysis therefore requires the association of a GAP to promote GTP hydrolysis. Consequently, GAPs are responsible for the return of Rho to an inactive state. Finally, GDP bound Rho can be extracted from the membrane and bound in an inhibited state in the cytoplasm by GDIs (Figure 1.5). As a result, the activity of Rho depends on the relative abundance and activity of these three species.

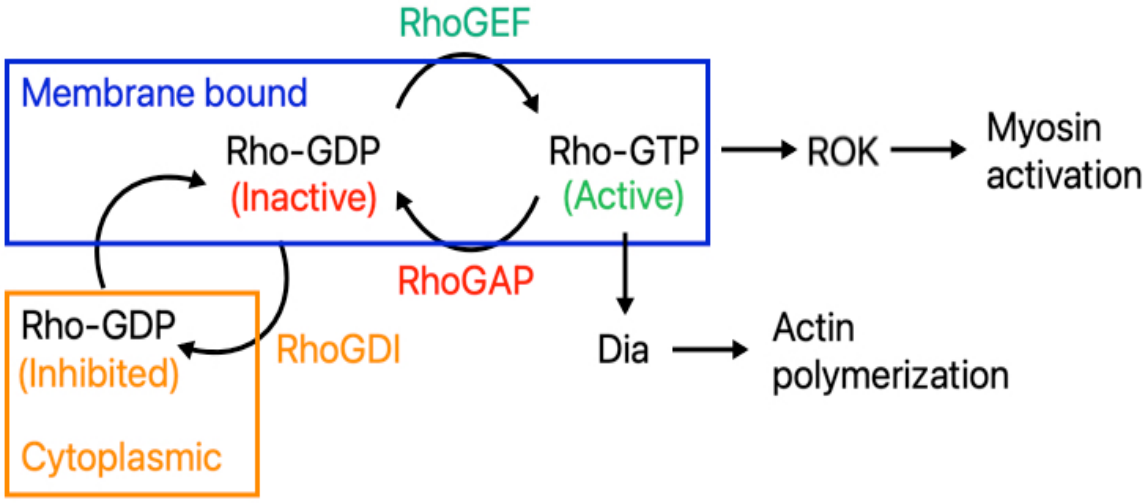

Figure 1.5: Regulation of Rho activity and downstream actomyosin contractility
Rho activity is dependent on the relative activities of RhoGDIs, RhoGAPs, and RhoGEFs. Active Rho promotes actomyosin contractility by activating myosin through ROK and increasing actin polymerization through Dia.

1.2.3 Force generation and transmission

While the regulation of the phosphorylation state of myosin is largely responsible for its ability to assemble into minifilaments and undergo a power stroke, the net effect of the powerstroke depends on a number of factors relating to the organization and linkage of the actin cortex[42]. How actin filaments are organized in the cortex greatly affects the amount of force that myosin motors can generate. Actin filaments are polarized with a plus and minus end[43], and myosin motors are plus end directed motors[27] (Figure 1.3). As a result, the relative organization of actin filaments greatly affects the outcome of myosin motor activity. Actin filaments can be branched, due to the activity of formins like Arp-2/3, creating a meshwork organization[44] that has less potential for contraction. Unbranched filaments, due to the activity of formins like Diaphanous[45], have more potential for contraction, but the organization is still critical. Highly organized actin networks, resembling that of a sarcomere in which oppositely oriented actin filaments are bound by myosin minifilaments near their minus ends[46,47], have the greatest potential for net translation, and when coupled to other components of the cortex, the greatest force generation[23,48,49] (Figure 1.3).

Furthermore, the actin filaments can be crosslinked by various actin binding proteins that will impact the ability of myosin motors to exert force based on the type and concentration of crosslinkers. For example, non-contractile actin bundles are tightly crosslinked by fimbrin, which is short enough to preclude myosin binding between filaments[43]. Alternatively, alpha-actinin is another common crosslinker that favors contractile bundles. The spacing between filaments permitted by alpha-actinin is permissive for myosin binding[43] and therefore this crosslinker acts to create a more organized actin network that can be bound by myosin. Furthermore, the connectivity of the network provided by crosslinkers like alpha-actinin is

important for the translation of motor activity into contractility[50]: without some amount of crosslinking, motor activity leads to movement of actin filaments without net changes in the organization. On the other hand, excessive crosslinking prevents the filaments from moving at all. Therefore, the contractile ability of myosin depends on the identity and abundance of crosslinkers.

Finally, producing changes to cell shape from myosin contractility requires strong linkages between the cortex and the cell[30]. Actin filaments need to be anchored to cell-cell linkages, which in the case of epithelial tissues like the *Drosophila* blastoderm, occurs primarily at adherens junctions[51]. Actin filaments are mechanically coupled to adherens junctions through the activity of a number of junctional proteins, including alpha-catenin[52], allowing myosin generated forces to alter cell shape and, when regulated across many cells, tissue architecture[25]. Furthermore, actin plus ends are enriched at adherens junctions through their interaction with alpha-catenin, promoting an actin organization that is conducive to maximal contractility[46].

Adherens junctions not only allow force to be coupled to the cell within which the force is generated to change shape, but the cell-cell linkages mediated by cadherins allow forces to be transmitted to neighboring cells and even across tissues[25]. This force transmission is critical for coherent cell movements to shape tissues but also creates a possibility for activation of mechanosensitive processes in morphogenesis.

1.3 Mechanotransduction and implications for development

A growing field of research has shown over the last few decades that many ways in which a cell's behavior can be influenced by the mechanical inputs it experiences[53,54]. This

phenomenon, generally referred to as mechanotransduction or mechanosensation, encompasses a wide range of downstream cell behaviors with the common feature that the behavior is triggered by a physical stimulus that is perceived by the cell to activate the associated response. These stimuli can include, but are not limited to: pressure, stiffness, force, and geometry[54].

Given the crucial role for force generation during morphogenesis, it stands to reason that force sensitive processes in the cell may be activated during development[55]. While this could constitute a non-specific response with little relevance to the process at large, it is also plausible that these responses feedback on to the developmental process in a manner that is relevant to the final outcome. In the latter scenario, mechanotransduction may represent an effect that is explicitly accounted for during morphogenesis rather than an unintended consequence. One possible role for such a developmentally relevant force sensitive response is that of myosin.

Among the accumulating evidence for various mechanosensitive processes are several works which provide preliminary evidence that myosin is recruited in response to increases in edge tension. The most striking example comes from a study in cell culture, in which stretching cells or ectopically increasing cell contraction with pharmacological myosin activation lead to further increases in myosin on cell edges[56]. A similar response has been demonstrated *ex vivo* in *Drosophila* wing discs[57], but as with the former experiments, it is unclear whether these results translate to intact systems such as developing embryos. Some evidence for a correlation between myosin and tension exists in the context of the developing embryo[58,59], but strong evidence for true causality is still lacking. For example, myosin also generates tension, and therefore it is unclear from the observed correlation whether high myosin levels are the cause

or result of increased tension. As a result, two important questions remain unanswered: first, a definitive causal relationship for tension dependent myosin recruitment has yet to be indisputably demonstrated. Secondly, if such a mechanism does exist and act in the developing embryo, it is uncertain what significance such a mechanism has for normal development. Many experiments measuring the cell's response to mechanical perturbations rely on highly invasive methods that cause damage to the tissue. In these cases, it is clear that the cell exerts a response, yet it is less clear if this same response is ever provoked under normal conditions. Therefore, addressing these question requires novel techniques to induce tension in a developing embryo in a manner that can be unambiguously distinguished from the underlying dynamics. Additionally, this method should mimic the natural conditions of strain generation in the tissue and be minimally invasive, such that the observed response is clearly distinguishable from a wound response[30,60].

1.4 *Drosophila* gastrulation as a model to understand the role of mechanics in development

1.4.1 Motivation

Morphogenesis involves substantial tissue rearrangement in an extremely short period of time, making the process highly dynamic. In the example of the *Drosophila* embryo, the entirety of embryonic development occurs in just 24 hours. As an even more dramatic example within this already impressively dynamic system, VF formation and the fast phase of GBE, during which the majority of axis elongation occurs, lasts only around 30 minutes. These processes highlight the rapid nature of the tissue deformations that are required to shape a developing

organism. Consequently, large amounts of tissue strain are inevitably generated. Yet whether the levels of strain reached during normal development are high enough to trigger such mechanical feedback mechanisms has yet to be thoroughly characterized.

1.4.2 D-V patterning and ventral furrow formation

In *Drosophila*, gastrulation begins following the completion of cellularization, the process that transforms the single, multinucleated cell of the syncytial embryo into approximately 6,000 individual cells forming a continuous epithelium on the surface of the embryo[61]. The resulting cellular blastoderm is a uniform sheet of cells without any obvious differences in cellular phenotype, with the exception of the pole cells. The formation of the cephalic furrow, a thin groove effectively demarcating the future head region from the trunk of the embryo, therefore causes the first visible change in the blastoderm[62]. Almost simultaneous with the appearance of the cephalic furrow is the onset of gastrulation, beginning with ventral furrow (VF)

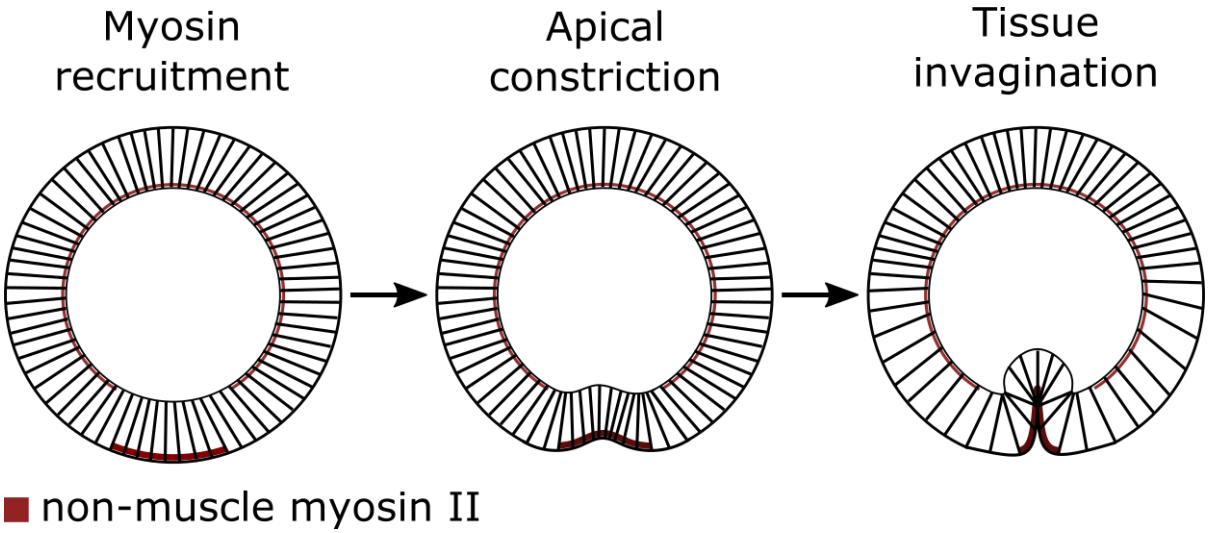

Figure 1.6: The ventral furrow (VF) is formed by apical constriction downstream of D-V patterning of apical myosin
Cells in the expression domain of *twist* and *snail* (Figure 1.1) remove myosin from their basal pool and accumulate myosin apically. This apical pool constricts, leading to tissue bending and eventual invagination to form the presumptive mesoderm during the process of VF formation.

formation, making it the first major morphogenetic movement in the embryo. In this process, cells at the ventral midline accumulate myosin at their apical surface downstream of the dorsal-ventral patterning genes *twist* and *snail*. These transcription factors have sharp expression domains in the ventral region: *Twist* is strongly expressed in the 18 cells centered about the ventral midline, and *snail* is expressed in a domain about 2 cells narrower than that of *twist*[63] (Figure 1.1). Together, *twist* and *snail* lead to the apical recruitment of myosin in the ventral domain (Figure 1.6), acting through *folded gastrulation* (fog)[64] and *concertina* (cta)[65], to recruit RhoGEF2[66], which in turn activates Rho[64,67].

The recruitment of myosin to the apical cortex through Rho signaling causes 8-10 cells at the ventral pole to undergo apical constriction, leading to tissue bending and subsequent invagination[68] (Figure 1.6). Approximately 1000 cells, about one sixth of the total cells in the embryo, leave the surface of the embryo at this time as they are internalized into the VF to form the presumptive mesoderm[61]. As a result, the remaining cells along the circumference of the embryo must accommodate for the reduced number of cells now spanning the same area by stretching. In this way, the epithelium is able to maintain its integrity in the face of such dramatic tissue changes. How exactly it does so it an open question.

1.4.3 A-P patterning and germ-band extension

As the ventral furrow is still forming, the process of germ-band extension (GBE) begins. This convergent-extensive tissue movement produces the elongation of the body axis[62] through directional cell intercalation[69] driven by an anisotropic myosin distribution[70] in the germ-band (Figure 1.7). This distribution, in which cell junctions parallel to the D-V axis are heavily enriched with junctional myosin while junctions parallel to the A-P axis are almost completely

devoid of myosin, leads to contraction of those edges enriched in myosin and subsequent elongation in the opposite direction in a process known as a T1 transition[70] (Figure 1.8). In this way, cell intercalation leads to narrowing of the germ-band - the lateral trunk region of the embryo, later giving rise to the segmented portion of the embryo - in the D-V direction and lengthening in the A-P direction. This tissue rearrangement, in combination with the pull from the invaginating VF, leads to the movement of the lateral tissue away from the dorsal pole, which soon becomes occupied by the posterior end of the embryo as the lengthening of the body axis causes the embryo to fold on itself and move onto the dorsal side[71] (Figure 1.7).

In total, the process of GBE produces an approximately 2.5-fold increase in the length of the embryo, with the majority occurring in the first 30 minutes, referred to as the fast phase of GBE[62]. The remaining elongation occurs much more slowly over a period of about 2 hours

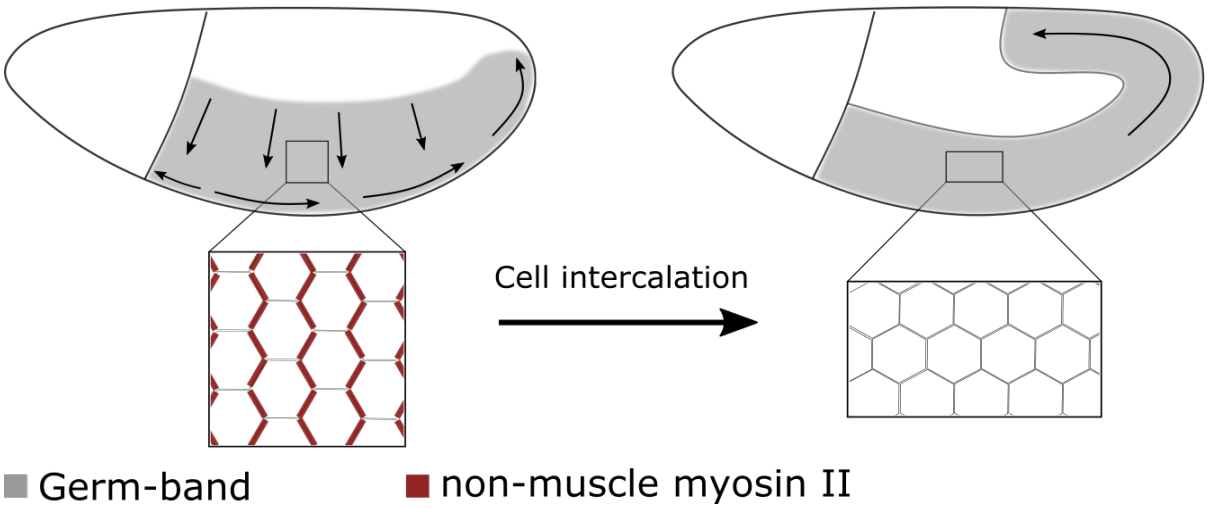

Figure 1.7: Germ-band extension elongates the body axis through directional cell intercalation
Germ-band extension is the convergent extensive process through which the germ-band (gray) narrows along the D-V axis and extends along the A-P axis. This process is known to be driven by directional cell intercalation mediated by the anisotropic myosin distribution (inset, dark red). This myosin distribution is known to depend in part on A-P patterning elements, such as Eve (Figure 1.2). As the germ-band elongates, it wraps onto the dorsal side of the embryo. Arrows show direction of flow.

during the slow phase of GBE. The highly dynamic nature of the dramatic tissue rearrangements required to elongate the tissue nearly 2-fold in just 30 minutes, all the while maintaining epithelial integrity, makes this process an ideal context within which to study the role of mechanics in development.

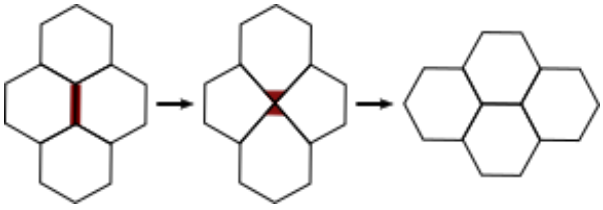

Figure 1.8: A T1 transition is the minimum unit of cell intercalation
Cell intercalation during GBE occurs through many individual T1 transitions. In this process, an edge enriched in myosin (dark red) contracts to a point. A new cell edge forms in the orthogonal direction, resulting in a change of aspect ratio and new neighbor relationships.

1.4.4 Current models and open questions

The accumulation of myosin on junctions parallel to the D-V axis and removal from those parallel to the A-P axis is known to be downstream of the A-P patterning system of the embryo, established by the maternally deposited factor bicoid[69]. This maternal gradient establishes the gap genes which in turn establish the striped expression patterns of pair-rule genes such as even-skipped and runt. Pair rule genes (PRGs) establish an even more refined striped pattern of Toll-like family receptors (TLRs), which in turn lead to anisotropic myosin localization[12].

While these genetic dependencies have been shown, much remains unknown about the details of the mechanism establishing myosin anisotropy from these striped patterns. Early work establishing the role of PRGs in GBE demonstrated that even the most severe A-P patterning mutants still undergo the initial germ-band elongation much as wild type embryos do. It is only during the period of slow germ-band extension that a significant phenotype is observed[69]. This suggests that the establishment of the myosin profile is maintained in these

mutants and therefore perhaps rather than establish myosin anisotropy, pair rule genes may actually act to maintain the myosin distribution once already established.

Furthermore, it is as yet unclear how the Toll-family receptors interact to produce an anisotropic myosin distribution from their own isotropic distribution. It was originally hypothesized that a positional code established by differences in Toll receptor composition lead to myosin accumulation at interfaces of differing Toll composition through heterotypic binding[12]. However, There are a number of inconsistencies with this hypothesis, as described in a recent review[72]. Firstly, it is unclear how a heterotypic activation mechanism could preclude myosin recruitment at horizontal interfaces. For example, if a cell expresses Toll-2 and 6, and its neighbor expresses Toll-8, then Toll-2 and Toll-6 could form heterotypic interactions at the vertical interface with Toll-8 in the neighboring cell. However, Toll-2 and Toll-6 in that cell should be able to form heterotypic interactions with one another on horizontal interfaces with the cells above or below. Secondly, triple mutants exhibit stronger phenotypes than double mutants, but a heterotypic activation model predicts an equivalent effect in double and triple mutants. While the authors propose additional mechanisms, each has similar inconsistencies that leave many open questions to resolve the TLR based model for myosin anisotropy. It is therefore clear that despite great advances in the knowledge of the genetic patterning directing VF formation and GBE, some factors are as of yet unidentified, that may be additional genetic factors or different inputs entirely.

Besides genetic patterning, several works have suggested mechanical interactions between the morphogenetic processes occurring simultaneously contribute to the process of GBE. One such work has identified a decrease in strain rate and cell intercalation in *twist* mutants, indicating a role for VF formation in elongation, which they hypothesize to be a

potential extensile role of the internalized mesoderm undergoing intercalation and pulling the ectodermal tissue with it[73]. A later work suggests instead a role for the invagination of the posterior midgut to generate a pulling force on the germ-band that contributes to GBE[74]. However, these results are also consistent with a scenario in which the PMG getting displaced anteriorly makes space for intercalation and GBE to proceed unimpeded. Additionally, fog mutants, which were first characterized as having a specific defect for PMG invagination[75] and later to have a mild VF defect[76], continue to elongate fully, although the normal wrapping onto the dorsal side is disrupted, suggesting that the PMG acts as a symmetry breaking for the elongation of the germ-band, rather than a pulling force. Finally, a more recent work examining the myosin distribution during GBE measured a substantial reduction in the myosin anisotropy driving GBE in *twist* mutants[16]. Combined with the earlier work characterizing the reduced strain and cell intercalation in these mutants, these results suggest, as hypothesized by the authors, that the VF generates strain that recruits myosin through a mechanical feedback mechanism, which contributes to the myosin anisotropy and the subsequent cell intercalation. It is the hypothesis proposed therein that serves as the foundation for this dissertation.

1.5 Thesis

In this dissertation, we describe a quantitative, global approach to address some of the open questions in the current knowledge of the process of GBE, its dependence on an anisotropic myosin distribution, and the establishment of this myosin distribution. In particular, this work represents an experimental test of theoretical ideas proposed previously[77] and implicated by initial experimental evidence[7316]. Briefly, the former proposes that mechanical feedback for myosin recruitment is a prerequisite for mechanical stability of biological tissues. The latter

works suggest a role for the VF in establishing the anisotropic myosin distribution driving GBE, which could be through activation of just such a feedback mechanism. We take two main approaches toward testing these predictions: 1) rigorous characterization of the wild type dynamics of strain and myosin during the period of development corresponding to VF formation and the fast phase of GBE and 2) optogenetic and genetic perturbations to these wild type dynamics to measure the resulting changes in the myosin profile.

For the first approach, we utilize in toto light sheet microscopy to measure the global dynamics of strain and myosin across the entire embryo surface and further compare these large-scale dynamics to those at the scale of individual junctions with high resolution confocal microscopy. Careful analysis of the resulting data sets enabled quantification of strain rates and myosin rates over time and space and the subsequent identification of a strong correlation between these two quantities. We show that the observed dynamics can be recapitulated with a simple physical model incorporating mechanical feedback, bringing us to the second approach to test this model and the underlying hypothesis.

For the second approach, a potential causality beyond the strong correlation identified with the first approach was tested by introducing changes to the endogenous pattern of strain rate using both optogenetic and genetic perturbations and measuring the changes in the myosin distribution from the previously characterized wild type profile. With optogenetics, ectopically high strain rates were induced in a variety of contexts using light activated regulators of actomyosin contractility. Using these methods combined with the quantitative approaches developed to enable the characterization of the WT embryos, we determined a causal link between strain rate and myosin rate. These perturbations not only showed that an increase in strain rate causes a proportional increase in myosin rate, confirming a mechanical feedback

mechanism for myosin recruitment, but also uncovered a D-V modulation of the feedback strength. Genetic mutants were used to remove endogenous sources of strain, namely the VF, and therefore reduce strain rates in the embryo, leading to a subsequent reduction of the associated myosin rates. Finally, we quantitatively relate these changes to a significant defect in a key morphogenetic process, supporting the relevance of this feedback during the course of normal development. To conclude, we discuss these results in the context of the current literature and the implications directing future studies.

Chapter 2:

Technical and methodological foundation for a quantitative study of mechanical feedback

Our scientific endeavors, at least experimentally, have always been limited by the tools available at the time. With each advancement comes a wave of new understandings made accessible by the improvements in technologies as well as the strong foundation laid by previous research. In the case of *Drosophila* embryogenesis, this began with the advent of mutagenic screens identifying developmental mutants and was later furthered by immunohistochemistry and fluorescence microscopy. For many years, these methods have represented the standard in the field, and while they have provided numerous insights, limitations in available tools, including microscopy, image processing and analysis, and techniques for local, non-invasive perturbations, have constrained the full range of potential

discoveries. Consequently, more recent years have fostered a growing appreciation for the need to obtain dynamic data that is amenable to rigorous, quantitative analysis in order to expand on these earlier insights and better understand the highly dynamic and global problem of morphogenesis.

This work benefitted greatly from many key advancements in the field, without which it would not have been possible. The development of these tools and techniques, with the exception of the design of the optogenetic activation protocols, was entirely the work of others who are credited in the corresponding sections. Although we merely took advantage of those developments, given their importance to enable the work presented in this thesis, we describe them in brief in the following chapter including the basic concepts and how they were incorporated into this work. The most notable methods that will be described in the following sections are light sheet microscopy, dimensionality reduction, and optogenetics.

2.1 Light sheet microscopy

While the particulars of our light sheet microscope have been detailed in ([78]), herein we briefly describe the concept, improvements from earlier iterations, and utility for the study of developmental biology. Light sheet microscopy offers a variety of advantages over other widely used imaging techniques, in particular confocal microscopy, which is a standard in the field, including fast imaging times, gentle imaging settings, and the ability to image entire samples in 3D over long time periods. While several of these advantages are inherent to the modality of light sheet microscopy, others are attributed to advances in our specific setup. In this work, we make extensive use of a more advanced form of light sheet microscopy known as multi-view single plane illumination microscopy (Mu-Vi SPIM) for whole embryo imaging.

We will therefore discuss features general to all forms of light sheet microscopy as well as those specific to Mu-Vi SPIM.

The basic principle of light sheet microscopy is to generate a sheet of light passing through the sample to illuminate a single plane at a time, which is then imaged in its entirety by a detection objective oriented orthogonal to the sheet. This light sheet can be generated from a laser using a cylindrical lens or, as is the case in our set-up, by rapidly scanning a gaussian beam vertically to the desired height to create a digital light sheet, which will create optical sections of the sample with height and width set by the camera field of view and depth determined by the waist of the sheet, in the case of our scope approximately 540 x 540 x 1 um. Larger 3-D image volumes can then be created by translating the sample through the sheet to image at varying depths with the lower limit of the step size restricted by the width of the beam, which is in turn determined by the numerical aperture of the illuminating objective. While the diffraction of light therefore limits the axial resolution of the light sheet as with confocal microscopy, light sheet microscopy has the distinct advantage of being able to overcome this limitation by rotation of the sample, effectively swapping the lateral and axial directions. In this way, the resolution in all directions is equal and set by the numerical aperture of the detection objective.

One of the most significant advantages of light sheet microscopy attributed to its unique design is the compatibility with large samples; imaging large 3D volumes with very decent resolution is incredibly fast by comparison. In confocal microscopy, for example, imaging occurs pixel by pixel as the laser rasters across the sample to form an image, and higher resolution comes at a huge cost in acquisition time. As a result, imaging larger samples, such as an entire *Drosophila* embryo, with adequate resolution for meaningful analysis occurs on

timescales that are incompatible with cellular and even developmental processes. While our light sheet boasts a modest 0.26 um resolution in all directions, this is more than adequate to address the question posed here and allows us to image the full embryo from multiple angles in under 20 seconds. Naturally, the total acquisition time depends on a number of factors, such as the exposure time, number of views, step size, and camera frame rate, yet we find that very little compromise must be made in terms of image quality to achieve this time frame. Previous iterations of our setup, as described in ([78]), have produced similar images in about 75 seconds, which while still more than fast enough for developmental processes leaves plenty of room for reducing acquisition times to be compatible with cellular processes. Therefore, several improvements were implemented to our scope, namely the installation of significantly faster cameras, as the bottleneck for acquisition rate is the camera frame rate. Nevertheless, with fast enough cameras, new bottlenecks arise, for example, the speed at which the images can be written and saved. While imaging from two cameras at once halves the acquisition time, it doubles the data to be written within that time. This can create problems if the write speed is incompatible with the acquisition speed, leading to a backlog of data and slowing the processing. As a solution, individual images are dumped into TIFF stacks without sorting to save on data writing times. Each image has a tag containing all relevant information regarding camera, view, time point, z slice and channel, allowing a simple script to automatically sort and save the images into smaller TIFF stacks for each timepoint, channel, and angle. While this adds another step and several hours processing time, the reduction in imaging time is more than worth the added effort. Together, these advances allow whole embryo imaging on timescales comparable to imaging a single smaller and shallower region on a confocal, giving light sheet microscopy a huge advantage in imaging speeds.

Unlike conventional microscopy modalities, including epifluorescence and confocal microscopy, in which the sample is illuminated and imaged from the same direction, in light sheet microscopy, the detection arm is perpendicular to the illumination arm, with two important consequences. Firstly, photobleaching of the sample is greatly reduced. When the sample is illuminated and imaged from the same direction, the entire Z depth is exposed in order to excite the region at the focal plane to be imaged. In contrast, the entire focal plane of the detection objective is illuminated and imaged at once in a light sheet such that only the region being imaged is exposed to light. Therefore, the total light exposure of the sample is drastically reduced, resulting in substantially less photobleaching. Secondly, while the confocal microscope has addressed the issue of out of focus light with the introduction of a pinhole, which significantly reduces the total light captured and consequently requires much higher laser powers, the nature of light sheet microscopy makes such implementations unnecessary, as the illumination of Z planes outside of the focal plane is virtually absent. Illuminating with a digital light sheet rather than a static one offers a few additional advantages to reduce photobleaching and scattering. The total exposure time of each X (vertical) position within the sheet is slightly less, leading to a further reduction in the effects of photobleaching. More consequently, we implement a method of imaging termed “confocal mode”, in which the camera acquisition is synced with the beam scanning rate such that only a subset of the full vertical height is imaged at a time, which corresponds to the region illuminated by the scanned beam at any given time[79]. The result is a significant reduction of in plane scattering and a substantial increase in image quality. In addition to these benefits, the unique setup of light sheet microscopes offers a variety of advantages over other modalities that are particularly useful in the field of developmental biology.

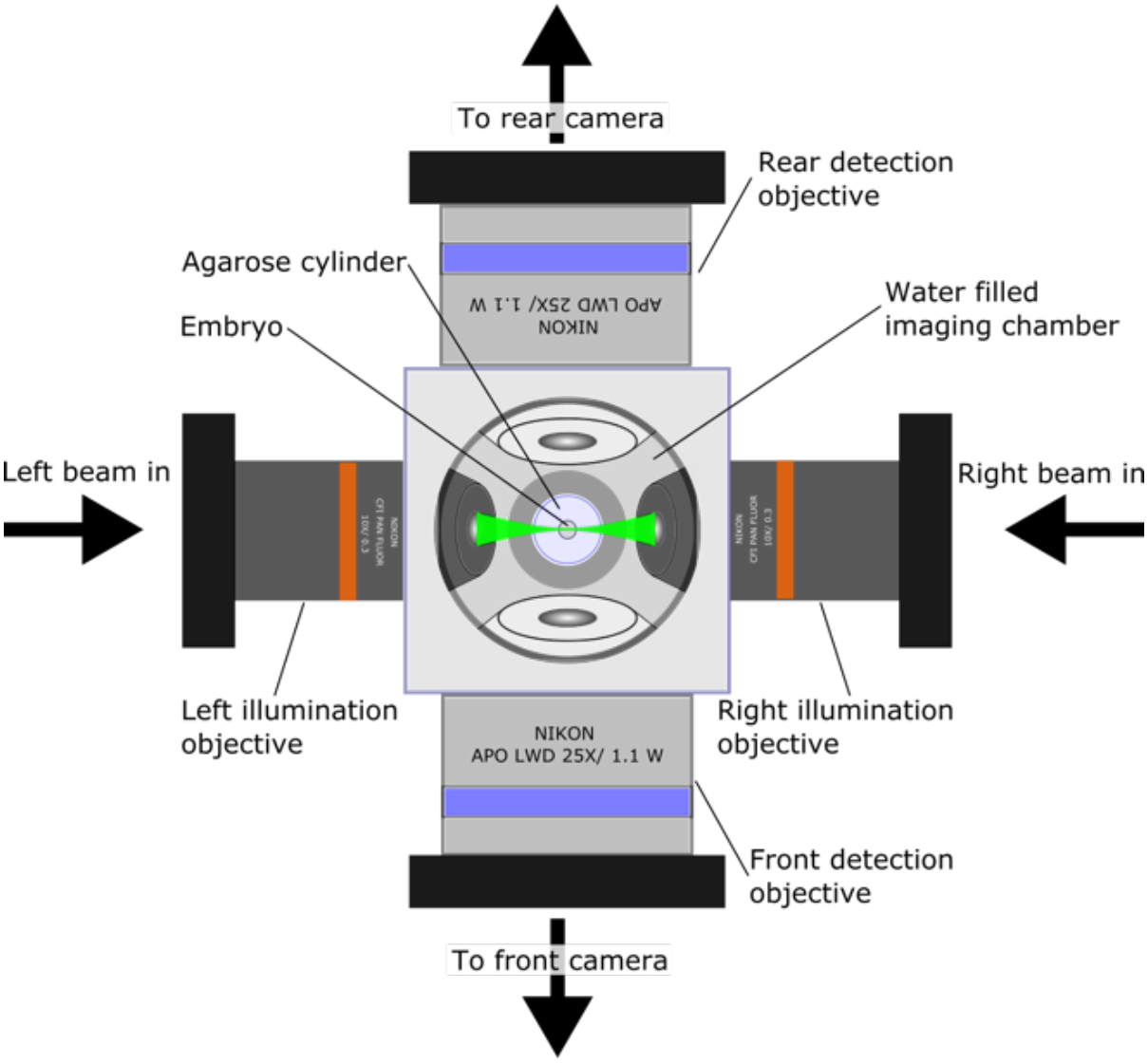

Figure 2.1: Mu-Vi SPIM setup
Top-down view of the objectives and imaging chamber of the light sheet microscope. A multi-view SPIM setup duplicates that of a standard SPIM such that it consists of two illumination arms, each composed of a low NA objective through which the laser is focused, and two imaging arms, each composed of a high NA detection objective coupled to a high-speed camera.

In the case of many biological samples, including the *Drosophila* embryo, imaging the full depth of the sample is greatly hindered by scattering due to the optical properties of the sample, autofluorescence of the yolk in the case of the fruit fly embryo. While this is a limitation general to all forms of light microscopy, multi-view light sheet microscopy offers a

unique advantage to overcome this issue. In Mu-Vi SPIM, the illumination and detection arms are duplicated such that the sample is illuminated from either side, and the resulting excitation is detected from the other two directions, which are perpendicular to the sheet (Figure 2.1). This allows for half of the sample to be imaged from the corresponding side to minimize the effects of scattering on the resulting image. To further increase the image quality, the sample is then rotated about its long axis and imaged again. This can be repeated for any number of angles such that each portion of the sample surface is represented by an image of optimal quality. While many rounds of imaging from a variety of angles would no doubt produce a final image of outstanding quality, each subsequent round contributes to two of the major disadvantages of light sheet microscopy: imaging time and large data size. Each angle imaged produces two image stacks, whose size depends on the depth imaged and optical section used, in a discrete time period, generally limited by the camera acquisition rate. The total data size and imaging time is therefore each of these values for the single position multiplied by the number of positions. In this way, the size of individual datasets and the length of time per acquisition can become entirely incompatible with available storage on the machine operating the microscope and developmental timescales, respectively. We have therefore found that the ideal compromise between optimizing image quality and minimizing data size and acquisition time is to image each sample at 4 positions with a 1.5 um z section. This produces 8 images total acquired at 45 degree intervals, offering more than adequate coverage of the surface while still completing the imaging period in less than 20 seconds. Furthermore, the nature of rotating the sample leads to an isotropic point spread function and therefore a final image resolution in all directions given by the numerical aperture of the detection objective, in our case 0.2619 um.

In order to obtain a single, 3D image from the individual views, image fusion and deconvolution are performed. Fluorescent beads suspended in the mounting agarose serve as fudicial markers for point detection and mapping to determine the precise transformation required to align each of the eight images into the same reference frame[80]. The pixel information from each image is weighted according to the proximity to the detection objective, and deconvolution uses the point spread function measured from the beads to remove some of the effects of diffraction from the final image[81]. The resulting image is a 3D image stack containing the entire embryo with isotropic resolution. For time lapse imaging, the same procedure is repeated at the desired time interval (typically 30-60 secs for our experiments) and for the duration of the process of interest (in our case, VF formation and fast GBE, approximately 40 minutes).

2.2 Pullbacks: 2D images from 3D datasets

Although light sheet microscopy offers an advantageous system to quickly and gently image entire 3D samples, meaningful downstream analysis, especially of a quantitative nature, represents a formidable challenge to a more widespread implementation of light sheet microscopy. The resulting images are very large, such that viewing a single time point can be cumbersome, let alone trying to view the sample over time. Even viewing distinct regions within the same time point becomes a burden when 3D rendering is too resource intensive to be feasible. Therefore, we utilize the methods developed in ([82]) to perform dimensionality reduction and generate pullbacks that capture the entire embryo surface in a single 2D projection (Figure 2.2). This technique, termed Tissue Cartography, allows for the surface of a defined 3D object to be represented in 2D using a projection appropriate to the downstream

analysis. As the world map can be represented in a variety of projections depending on what regions and features are to be accurately portrayed, for example angles vs distances, we can use different projections of the embryo surface for different purposes. In this work, analysis is focused entirely on the trunk region containing the germ-band and ventral furrow. This region can be closely approximated as a cylinder, and therefore we use a cylinder projection, which has minimal distortions in this region. Furthermore, in downstream analysis, the metric tensor, which relates the projection to the 3D surface, is used to correct distortions in measured lengths or angles. Finally, with this pipeline, we are able to conveniently compare images of different embryos, as the pipeline allows us to produce images of a given convention that is consistent across all samples (Figure 2.2).

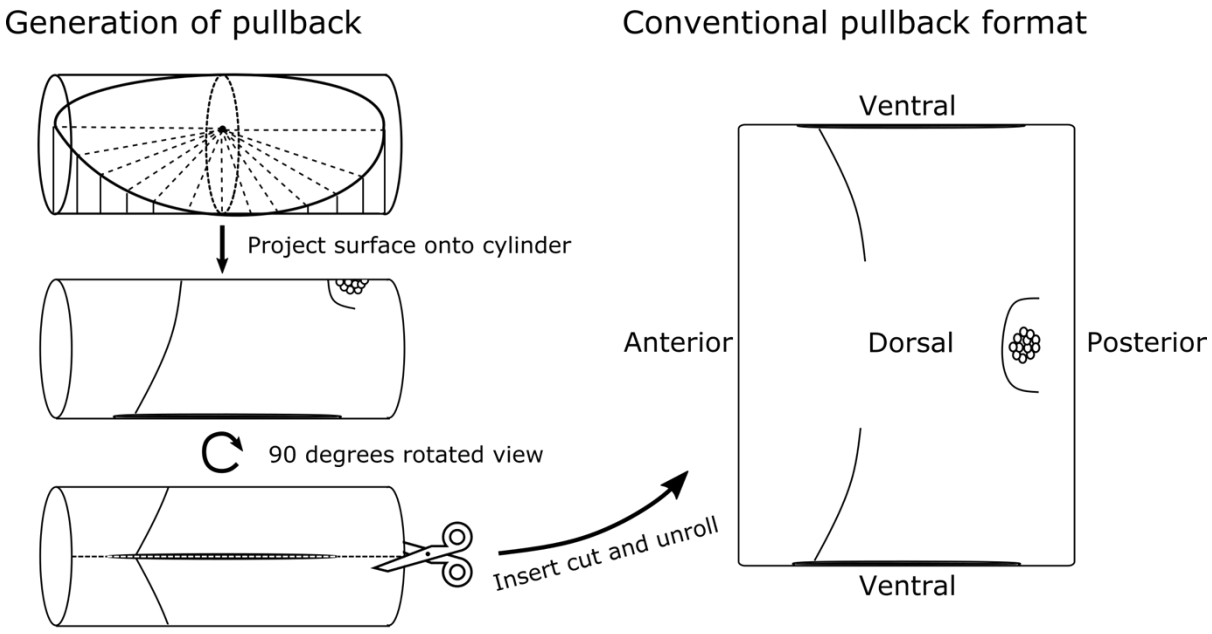

Figure 2.2: Schematic representation of 2D pullback generation from 3D light sheet data sets
Embryo surface is detected and fitted to a cylinder, onto which the intensity data is projected. A cut is inserted into the cylinder along the long axis at a set location, in our images always at the center of the VF. This allows the cylinder to be "unrolled" into a 2D pullback representing the full embryo surface in a single image. By convention, all pullbacks are oriented such that anterior is left, posterior is right, the dorsal side is in the center, and the ventral side is on top and bottom. Unless otherwise stated, all pullbacks represented in later sections are full embryo surface images following this convention.

These pullbacks are obtained using a detection and fitting protocol called ImSAnE[82]. A machine learning algorithm for pixel classification in ilastik is used to detect the embryo surface as the boundary between the class defined as background and the class defined as the sample[83]. This results in a 3D point cloud approximating the embryo surface (Figure 2.3.a). Each cross section is then fit by an ellipse to generate the surface that will be projected onto the plane. Furthermore, the surface can be normally evolved in either direction to generate pullbacks of variable depth relative to the embryo surface (Figure 2.3.b). While the resulting pullbacks adequately represent the embryo surface for many purposes, our analysis relies on detecting junctional myosin, which is restricted to the slightly subapical band of the adherens junctions. Due to small deviations between the detected and fitted surface resulting from the limitations of fitting an ellipse, however closely fitted, to a complex biological sample like an embryo, the pullback may not pass through precisely the same depth of all cells across the embryo surface. Consequently, such pullbacks obtained from the cylinder projection may contain the adherens junctions in some regions but pass above or below them in other regions (Figure 2.3.c). Attempting to measure the junctional myosin from such images would therefore give inaccurate and/or incomplete quantification. In order to address this issue and ensure that the projected surface represented the same depth in all cells across the embryo, we employed a secondary fitting step to generate a refined surface projection (Figure 2.3.c').

A 3D image stack through the embryo surface is generated by normally evolving the fitted surface from the step above by 2 pixel increments for 25 steps outward (away from the embryo center) and inward (towards the embryo center), producing a total of 51 layers representing a stack of approximately 26 microns roughly centered about the cell height corresponding to the adherens junctions. A pixel classification workflow in ilastik is again used

to detect the surface (Figure 2.3.d), which is then fit by a thin plate spline (Figure 2.3.e). Several layers on either side of the surface are obtained by normal evolution of the fit. From these layers, a maximum intensity projection of the 6 layers most closely corresponding to the adherens junctions, as evidenced by the strong junctional myosin signal, is taken as the final image used for analysis. The MIP represents an image stack of 2.6 microns, which is approximately the width of the adherens junction.

For each of the above steps, once the surface is detected and fitted, it can be applied to an entire time lapse data set to produce 2D pullbacks of the surface over time. Because the embryo is confined to its shape by the vitelline membrane, the position of the surface is constant over time, meaning that the same surface projection can be used to generate a pullback for all time points. In this way, a 4D time lapse data set corresponding to several hundred gigabytes can be visualized in a single TIFF stack of less than a gigabyte.

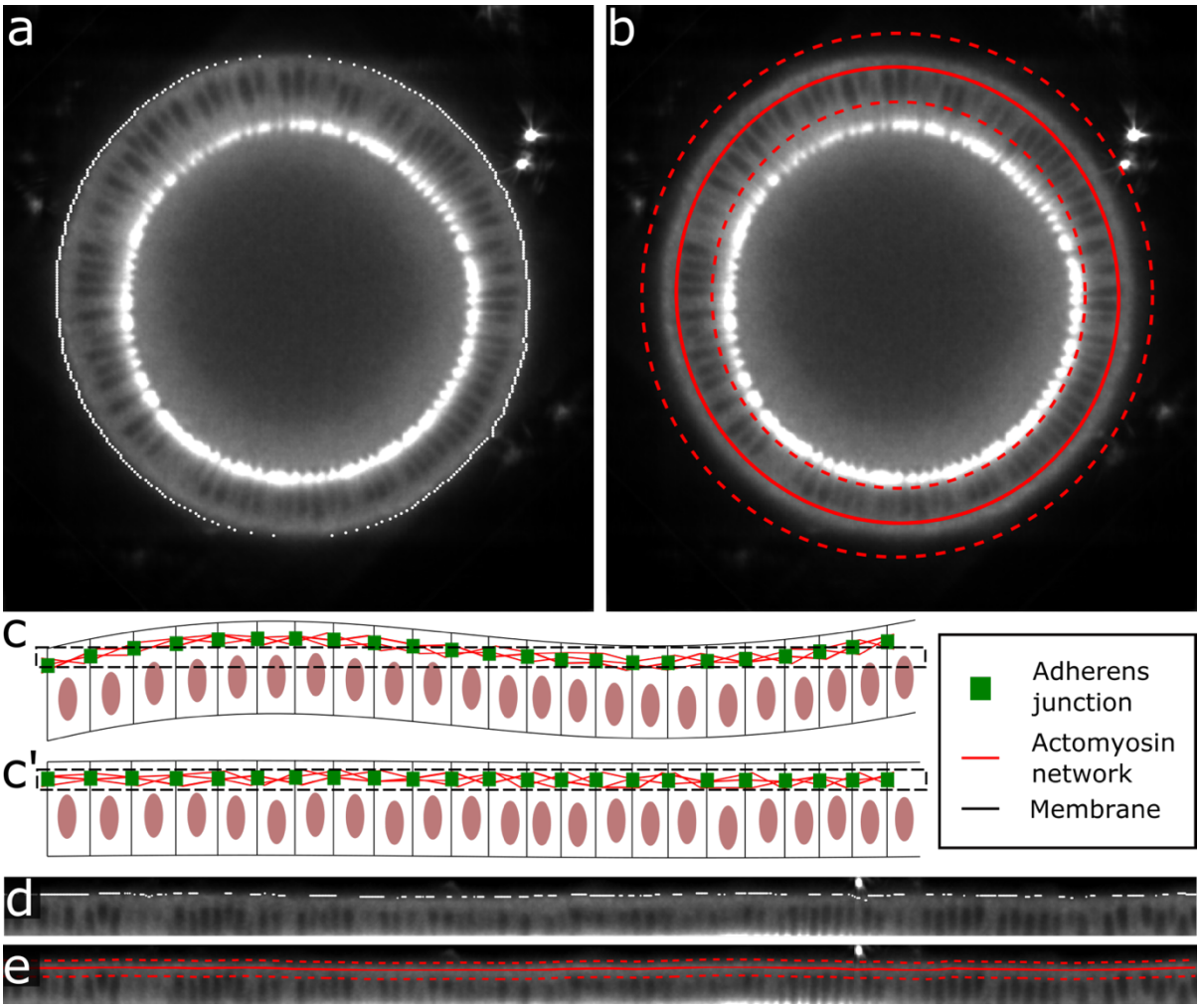

Figure 2.3: 2D Pullbacks of adherens junctions from whole embryo light sheet data
a. Example of a cross section through the approximate midpoint of an embryo along the A-P axis. White dotted line shows point cloud of surface detected from ilastik training. b. Same cross section showing the surface fit from the point cloud after shifting the surface basally. Red dashed lines show the inner and outer most layers taken to form the 3D image stack for the refined fitting step. c. Cartoon representation of the pullbacks from the first step, in which the adherens junctions are not contained within the image substack. c'. Representation of refined pullback which now contains adherens junctions at the same height. Black dashed box represents image substack from which the final MIP is made for downstream image analysis. d. Cross section of the image stack obtained from the previous step (b). White dotted line shows point cloud of surface detected from ilastik training. e. Red line shows surface fitted from the point cloud in (d). Red dashed lines indicate inner and outermost layers normally evolved from the fitted surface.

2.3 Optogenetic control of actomyosin contractility

The discovery of light sensitive proteins from plants and their subsequent incorporation into non-plant systems, generally referred to as optogenetics, has added a powerful tool to many fields, not least of all developmental biology[84]. Prior to this, a significant obstacle in understanding embryogenesis has been the lack of tools to induce perturbations to specific gene products in highly controlled manners either in time or space but ideally both. Genetic knockout has offered invaluable insights into the genetic cascades that drive development, yet a more thorough understanding of the function of the associated gene products has been limited by the all-or-nothing nature of knockouts. In particular, it is challenging to understand the role of genes in a given process if that process relies on the completion of an earlier step also requiring that same gene. For example, myosin is required for the formation of the VF, yet the VF cannot form without the completion of cellularization, which also relies on myosin. Maternal mutants for myosin, therefore, cannot be used to study its role in VF formation. In *Drosophila*, the development of tools like the UAS/GAL4 system and the FLP/FRT system have allowed some control in space and time, but still lack the desired level of control, particularly in regard to embryonic development.

Pharmacological agents have been widely used to overcome the temporal challenges of genetic perturbations, yet they lack spatial control and often exhibit toxicity that makes them less than ideal for long term studies. For studies in this field, drugs inhibiting or over activating components of the cytoskeleton are often utilized to affect force generation or tissue mechanical properties, and therefore how they respond to force. However, because these components are also crucial to the cell's normal function and must be applied systemically, it is difficult to attribute observed cell behaviors under such conditions to native processes.

Additionally, determining the right dosage that will alter the tissue properties without inducing widespread cell and tissue damage is challenging. Finally, in the case of applying these compounds to *Drosophila* embryos, the vitelline membrane acts as a barrier that is impermeable to such drugs, therefore requiring that they be injected through the vitelline membrane. Even if great care is taken in the process, it is difficult to ensure that no damage is caused to the embryo in the process that could contribute to the observed cell and tissue response.

The introduction of optogenetics to animal systems therefore provided an extremely valuable tool to overcome many of the shortcomings of previously available tools. Light sensitive proteins undergo a conformational change in response to excitation by light of a particular wavelength. This change often results in differences in that protein's activity level or ability to interact with one or more binding partners. By creating transgenic proteins tagging a protein of interest to one of the components of a light sensitive system, precise control over the target protein's activity, localization, or degradation can be obtained using only carefully controlled light.

In this work, we use an optogenetic construct developed and characterized previously[85,86] based on the light sensitive interaction of Cry2 and CIB to allow spatial and temporal control of actomyosin contractility. Cry2 is protein that undergoes a conformational change when illuminated with 488 nm wavelength light (Figure 2.4). This conformational change opens up the binding site for its partner, CIB. When the light source is removed, this interaction has a half life of about 5 minutes, meaning that in the absence of continuous illumination, the perturbation is transient. This system can therefore be used to control the interaction of two species, by tagging one to Cry2 and one to CIB, or can be used to induce a

specific subcellular localization of a species of interest by anchoring CIB in a specific structure. The latter strategy is utilized for the system employed herein, in which CIB is anchored to the inner leaflet of the membrane and Cry2 is fused to Rho-GEF2 (Figure 2.4).

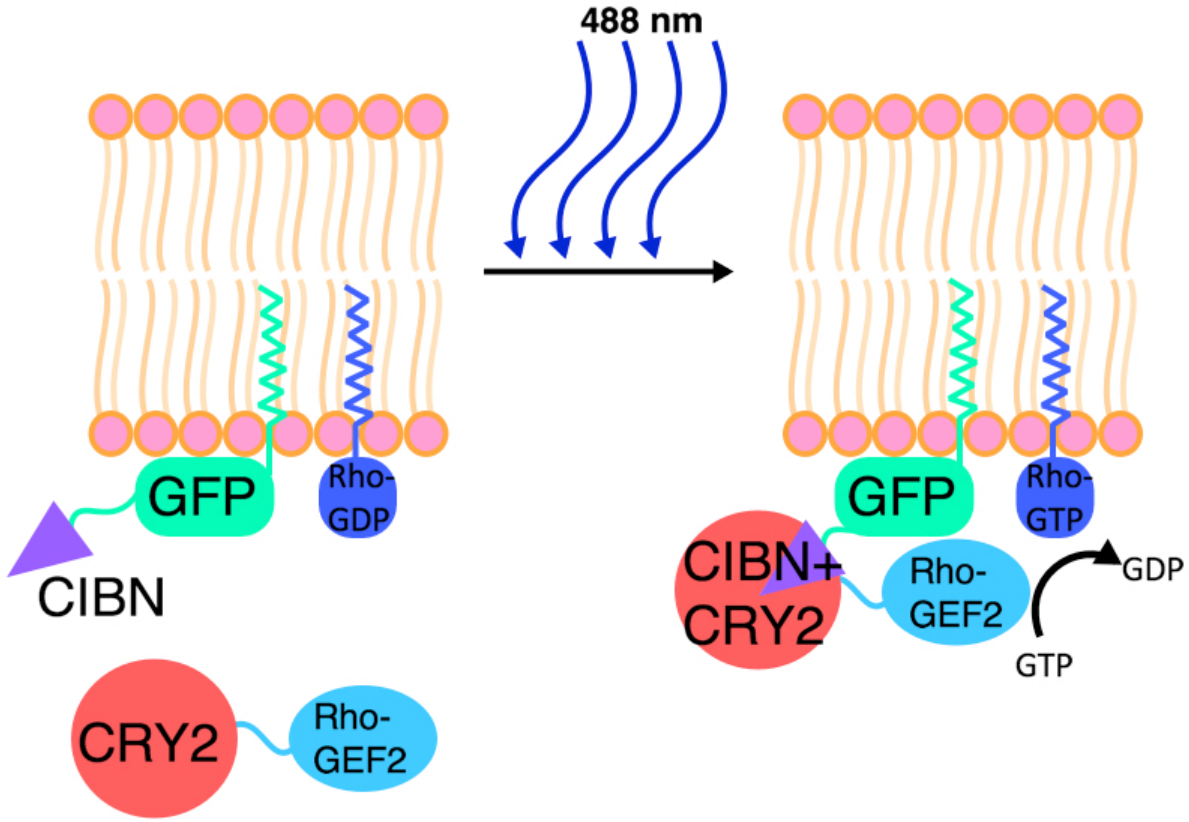

Figure 2.4: Cry2/CIBN optogenetic system for actomyosin contractility
Left: in the dark state, the binding site for CIBN on Cry2 is closed, and the Cry2-RhoGEF2 fusion remains in the cytoplasm, where Rho-GEF2 is unable to interact with Rho. Upon illumination with 488 nm wavelength light, Cry2 undergoes a conformational change, exposing the binding site for CIBN. This high affinity interaction results in the efficient membrane localization of the Cry2-RhoGEF2 fusion. Once at the membrane, RhoGEF can interact with its target Rho to promote the disassociation of GDP from GDP bound Rho, its inactive form, and allow for Rho to bind GTP, its active form.

As described in the introduction, RhoGEF is an upstream regulator of actomyosin contractility that activates Rho, which in turn activates ROK. As Rho in its competent form is localized to the membrane, Rho-GEF localized to the cytoplasm is unable to activate Rho. However, when Cry2 undergoes its conformational change in response to light, it is recruited

to the membrane, where its binding partner CIB is localized, translocating the fused Rho-GEF along with it. Once at the membrane, Rho-GEF activates Rho, leading to actomyosin contractility. This system, therefore, offers a method to pattern actomyosin contractility in time and space using only light, which we utilize to induce strain in a physiologically relevant manner that addresses many of the shortcomings of previous methods.

Many of the common techniques to probe or disrupt the mechanics of living systems thus far have relied on highly invasive methods with limited similarity to forces experienced by the embryo during the course of development. Examples of such methods are laser ablation, micropipette aspiration, explant stretching devices, and laser cauterization, all of which induce significant damage to the embryo in the process. It is therefore difficult to ascertain whether the tissue responses to such perturbations are indicative of endogenous processes at work during embryogenesis or whether they represent something more similar to a wound response that is not active during normal development but becomes activated when something goes awry. Because we are interested in the role of mechanics during normal development, we sought a method to induce strain that was both minimally disruptive to the tissue and that closely resembled the native mechanisms generating strain in the embryo. Actomyosin contractility is one such way that strain is endogenously generated in the embryo, as with apical constriction during VF formation, and we therefore chose this as a natural method to induce ectopic strain in a manner that is most relevant to the normal developmental process. The basic premise behind the experimental design is to induce actomyosin contractility in a given region, such that the region undergoes constriction (Figure 2.5.a-b). As it does so, the change in area of the activated region must be compensated for by the adjacent tissue, causing the cells contained therein to stretch (Figure 2.5.c). We can then measure the myosin signal in this

stretched tissue, outside of the activation, to determine whether subjecting these cells to strain results in significant changes in the levels of junctional myosin (Figure 2.5.d).

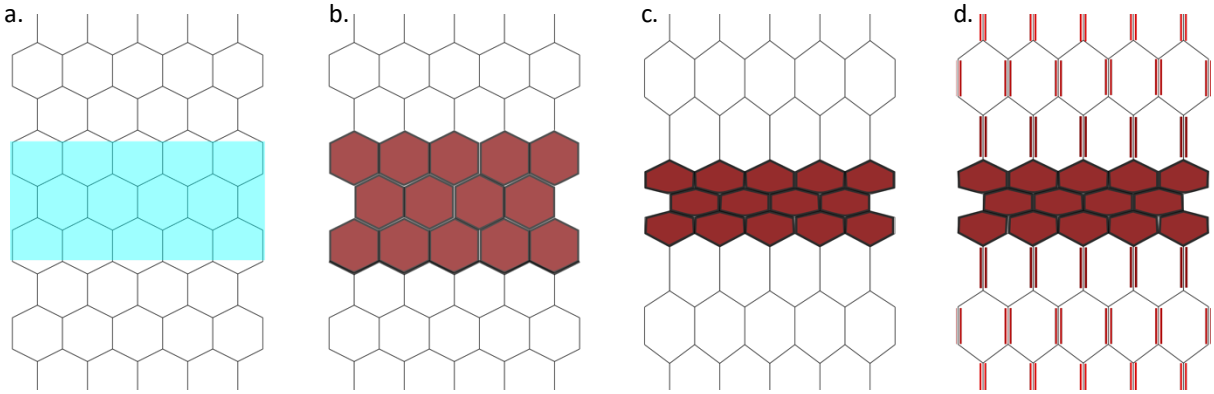

Figure 2.5: Conceptual basis for optogenetic experimental design
a. A local region of the embryo is illuminated to activate the optogenetic construct (blue rectangle). b. The region activated recruits myosin as a direct result of activation. c. The activated cells undergo actomyosin contractility, leading to a reduction in cell area. Adjacent cells are stretched to accommodate for the activated cells' change in area. d. According to our hypothesis for a mechanical feedback mechanism for myosin recruitment, the stretched cells will recruit myosin in response to the imposed strain, leading to significant increases in junctional myosin on the strained edges.

While pharmacological agents are often used in this context to increase or decrease strain generated via actomyosin contractility, as mentioned previously, these lack precise control in space and, to a lesser extent, time. In contrast, the spatial patterning of optogenetically activated actomyosin contractility is limited only by the ability to pattern the illuminating light in the experimental setup. Ideally, a digital micromirror device can be incorporated to allow for arbitrary light patterns, although we have not yet been able to implement such a feature into our setup. While our current light sheet setup therefore somewhat limits the feasibility of creating more complex patterns of light, it still allows ample degrees of freedom to induce strain in a variety of patterns. For example, as our setup uses a digital light sheet, the amplitude and origin of the scanned beam can be adjusted to illuminate only a

subset of the sample. Furthermore, the sample can be precisely positioned and moved through the beam to control the height and depth of activation.

An important consideration for the experimental setup was to ensure that the optogenetic construct is not activated outside of the intended region, as we are interested in measuring the changes in myosin outside of the activated domain in response to the activation. There are two potential sources for stray activation: weak activation by ambient light and activation due to scattering of the illuminating light. To address the former, it is important to protect the embryo from any ambient light during the entire course of the preparation and experiment, as even white light could activate the construct at low levels due its mixed wavelength composition. Accordingly, all work with optogenetic flies and embryos was performed in the dark, using only red light sources. To address the latter, we coupled a two-photon laser to the light sheet. The two-photon effect relies on the principle that the energy of two photons is combined when they meet at precisely the same location[87]. In this way, a light sensitive protein can be activated by light of twice the wavelength, or half the energy, as that required to induce the light sensitive response with a single photon. In our case, we use a femto-second laser tuned to a wavelength of 941 nm, which sufficiently activates the Cry2 fusion for recruitment to the membrane[85]. The focus of the beam ensures that only a very narrow region meets the criteria for this effect. As a result, the probability of two photons meeting at the exact same spot after scattering, i.e. outside of this narrow waist, is near zero, the chances of stray activation become near zero as well. This same effect also means that the region activated at any given point in time is very limited. While this offers an advantage in terms of very precise spatial control, it also creates the disadvantage of having such precise spatial control. Activating a given region requires placing that particular region directly in the waist of the

beam. While this is straightforward for a single position, activating a larger region requires each position within that region to pass exactly through the waist as well. The nature of the microscope setup and the shape of the embryo make this inherently challenging, particularly within the timescale permitted by the rate of development.

In addition to this minimum requirement for the entirety of the area to be activated to pass precisely through the beam waist, there were a variety of other criteria that our activation strategy should fulfill to address our questions. Firstly, it was desirable to induce strain of variable strength to recapitulate the range achieved during development. This can be accomplished by altering the length of activation, where longer activation times will result in more activated myosin and therefore more contractility. However, the optogenetic construct changes only the activation of myosin rather than the overall levels of myosin in the cell, so there is some limitation to the level of activation that can be achieved only by increasing the activation time. Furthermore, the amount of contraction produced by a single cell, and consequently the strain it can generate, is limited by the area it occupies. The total amount of strain generated can therefore be further increased by activating a larger region. Secondly, we wanted not only to determine whether myosin levels could be increased above their endogenous levels in response to increases in strain, but also whether myosin could be observed in contexts in which it is not normally observed by inducing ectopic strain in those contexts. One possibility is to do so based on the developmental stage. For example, at the time between the end of cellularization and the beginning of ventral furrow formation, the anisotropic myosin pattern driving GBE has not yet been established, and there is very little junctional myosin compared to the cytoplasmic pool. This brief time window therefore offers one context in which it is possible to recruit junctional myosin prematurely. For this reason,

many of the activations were planned for this time period after the epithelium has formed but before gastrulation has begun. A second possibility is to activate in regions which normally exhibit low levels of junctional myosin to see if these regions are competent to recruit myosin. For this, we chose the dorsal pole. Throughout GBE, the dorsal pole exhibits very little, if any, junctional myosin, and only much later, during dorsal closure, does this area demonstrate a pronounced accumulation of myosin. Activating adjacent to the dorsal pole during early GBE therefore represents another context in which de novo recruitment of myosin could potentially be observed. Finally, a third possibility is to determine whether a characteristic myosin distribution can be significantly altered by the ectopic induction of strain. The germ-band offers one such context, which we chose to exploit. During GBE, the characteristic myosin distribution is anisotropic, with junctions parallel to the D-V axis highly enriched in myosin and orthogonal junctions devoid of myosin[88]. Furthermore, the direction of strain during this period is in line with the myosin anisotropy, creating a scenario in which ectopic strain can be generated in the orthogonal direction to observe whether those junctions usually devoid of myosin will recruit myosin in response to the added strain.

Taking these factors into consideration, we designed two activation strategies that would meet the desired criteria (Figure 2.6). The simplest implementation of this experimental design, and therefore the one that we started with, takes advantage of the setup of the light sheet microscope to create relatively small perturbations that are reminiscent of the VF and can be applied to test the first two of the above contexts. This method involves positioning the embryo at some predetermined position and illuminating that position with the two-photon laser. The result is the activation of a single plane cutting through the embryo, equivalent to imaging a single Z slice. Because the intersection of the elongated embryo with the plane of

the light sheet forms an ellipse with long axis parallel to the embryo long axis, this method of activation effectively creates two nearly parallel lines of cells with activated myosin. The cells within these lines constrict, stretching the cells between them. Therefore, the primary direction of strain generated by these activations is perpendicular to the lines of activation, or parallel to the D-V axis of the embryo (Figure 2.6.b).

The lines of activation can be varied in width, position, and distance between them. The width of the activation can be increased by moving the embryo in the Z direction while illuminating, which will activate additional planes through the embryo according to the number of steps taken and step size. Positioning the embryo with the sheet closer to or farther from its surface will, respectively, decrease or increase the distance between the two lines. Finally, the approximate position of the lines can be set by rotating and translating the embryo until the desired region falls within the beam waist. This strategy can generate a moderate range of strain in a variety of locations, but the strain generated with this setup is always primarily directed perpendicular to the activation lines, which is parallel to the D-V axis.

To address the final context described above, therefore, requires an activation scheme that generates strain in the orthogonal direction. To this end, we decided to activate the entire head region, causing contraction towards the anterior pole and resulting in strain generated along the A-P axis of the embryo (Figure 2.6.c). There were two important considerations for the success of this strategy. Firstly, the head deviates strongly from the cylinder that approximates the rest of the embryo, and therefore having all of the head pass through the waist of the beam for uniform activation required many additional positions than typically defined for imaging. Secondly, the formation of the VF generates a huge amount of strain in the embryo during this period, and therefore inducing strain in the orthogonal direction requires a

perturbation strong enough to overcome the ventrally directed flow. This was accomplished in part through the relatively large activation area of the entire head and further by extending the activation period much beyond those used for the previous strategy. In this way, a strong activation was achieved that was able to induce a significant anteriorly directed flow. Activation of exclusively the head region was possible by lowering the embryo on the manual X stage until only the head was within the illumination field (Figure2.6c, center). The embryo was then activated by illuminating with the two-photon laser in a manner analogous to the normal imaging protocol but with several additional positions. After illumination, the embryo is returned to its pre-activation position for subsequent imaging (Figure 2.6c, right).

With these two activation strategies, we were able to induce strain in a variety of ways in order to test whether we observe a mechanical feedback mechanism for myosin recruitment, and if so, under what circumstances it acts to recruit myosin. The experimental design further allowed us to induce a variety of strain rates within the range experienced during the course of normal development which will provide positive support for a mechanism that is relevant to morphogenetic processes.

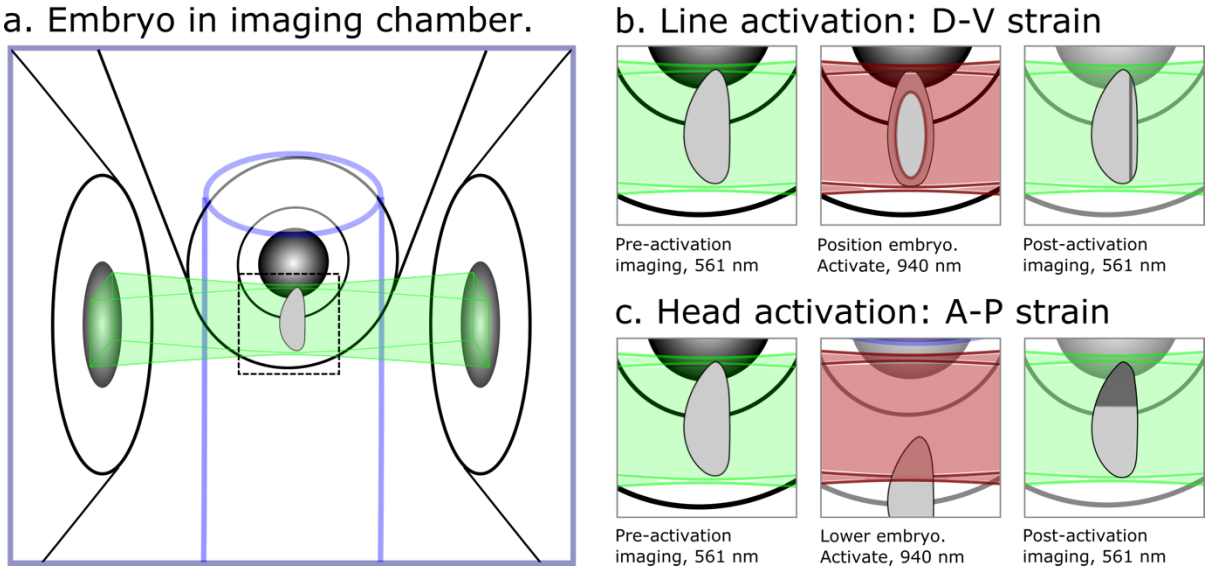

Figure 2.6: Schematic of optogenetic experimental procedure
a. Side view (from perspective of front detection objective, see Figure 2.1) of embryo mounted in agarose cylinder in the imaging chamber illuminated by the light sheet. b. Example of activation in two lines generating strain parallel to the D-V axis. Left: Embryo is imaged before activation with 561 nm illumination. Center: Embryo is positioned such that the sheet passes through the embryo at a given depth from the surface. 940 nm laser shutter is opened to activate. Right: Embryo is imaged after activation. Darker gray region indicates area activated. c. Example of head activation generating strain parallel to the A-P axis. Left: Same as above. Center: Embryo is manually lowered until only the head region falls within the light sheet. Embryo is then imaged from many angles with 940 nm illumination to ensure uniform activation in head. Right: Embryo is raised to the starting position and imaged after activation. Dark gray indicates area activated.

Chapter 3:

Characterization of wild type strain and myosin dynamics during early gastrulation

As discussed in the previous section, past descriptions of the processes during *Drosophila* gastrulation have been based on observations made from local and/or static views. While these individual snapshots can in principle be stitched together to create an approximation of the global dynamics, precisely aligning such tiles in time and space is very challenging and generally does not allow for reliable analysis. With the powerful combination of light sheet microscopy and image dimensionality reduction, we have addressed this limitation by generating time lapse data sets of the entire embryo with sufficient temporal resolution to quantitatively characterize the dynamics. We begin with a detailed analysis of the wild type flow patterns during the period beginning just before VF formation initiates through the fast

phase of GBE. The pattern of flow determines the strain profile, which we characterize by tracking the length of junctions over time. We next characterize the time course of the myosin distribution across the entire embryo surface using a quantity we term the junctional myosin accumulation. By comparing the strain profile to that of the myosin, we show a strong correlation across the embryo that we later test for a causal relationship, described in Chapter 4. Finally, we turn to high temporal and spatial resolution analysis to determine the relationship between the strain and myosin dynamics on individual junctions and compare it to that at the tissue level.

3.1 Characteristic flow during wild type gastrulation

During the period of development studied, there are three characteristic flow patterns that correspond to each of the major morphological events. These have been described previously[16], but we summarize them again briefly as they relate to the generation of the corresponding strain profiles characterized in the following section. For the duration of cellularization, there is no flow within the plane on the surface of the embryo, as the cells are in the process of forming and therefore not undergoing significant deformation. At the completion of cellularization, the onset of flow is marked by a slight shift dorsally, characterized by a ventral source and dorsal sink (Figure 3.1, left). The developmental significance of this motion is not well known but may simply be a consequence of the changes in myosin distribution that accompany VF formation.

The well characterized apical accumulation of myosin in the ventral region is preceded by the disassociation of myosin from the basal pool that remains from the cellularization front[16]. The resulting discontinuity in the basal pool will produce an imbalance of forces that

would lead to contraction on the opposite side of the embryo, likely responsible for the dorsal flow during this period. Shortly thereafter, these same cells redistribute the myosin to their apical surface, leading to strong apical accumulation of myosin in the ventral region which marks the transition to a second, distinct flow pattern, corresponding to VF formation (Figure 3.1, center). The cells at the ventral midline undergo apical constriction to initiate tissue bending and invagination[76], creating a reversal in the flow fixed points from the previous flow field, which now consists of a dorsal sink and ventral source. This flow pattern emerges because the region that internalizes during VF formation results in a reduction in the number of cells spanning the embryo circumference by about 1/6th. As a result, the remaining cells are stretched considerably to cover the vacated area while maintaining a continuous epithelial sheet across the embryo surface.

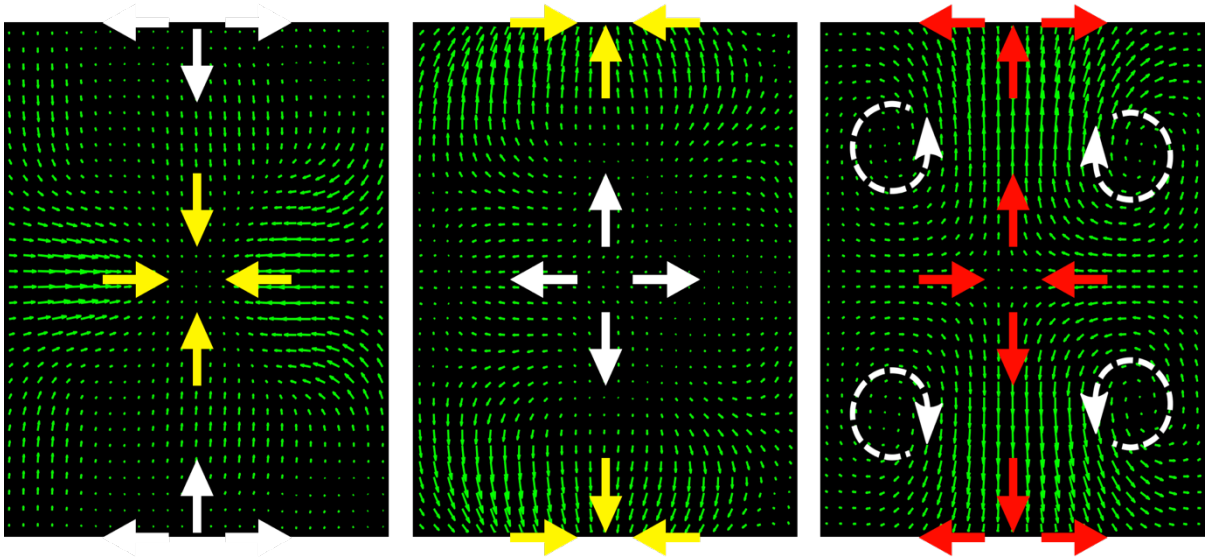

Figure 3.1: Flow fields for the three distinct flow patterns during gastrulation
Left: 5 minutes before CF formation. Flow field is characterized by a dorsal sink and ventral source. Center: 10 minutes after CF formation, during VF formation. Sink and source swap places from previous flow pattern, now characterized by a ventral sink and dorsal source. Right: 20 min post CF, characteristic flow during GBE corresponding of two hyperbolic fixed points (saddles), one dorsal and one ventral, creating four vortices, one in each quadrant. Arrows show primary flow directions. White = source, yellow = sink, red = saddle, white dashed = vortex. Note: magnitude of velocities are scaled to allow visualization, not uniformly across timepoints.

Shortly after VF formation initiates, the third characteristic flow pattern emerges with the onset of GBE (Figure 3.1, right). During GBE, cell intercalation produces flow toward the ventral midline and then onto the dorsal side of the embryo, producing a flow field exhibiting two saddles, one each on the dorsal and ventral poles, and four vortices, one in each quadrant formed by the A-P and D-V axes. The dorsal and ventral saddles are of opposing directions such that ventrally flow is toward the ventral pole from the lateral midline and away from the ventral pole toward the anterior and posterior poles and dorsally flow is away from the dorsal pole along the lateral midline and towards the dorsal pole from the anterior and posterior poles. These saddles create the four vortices in each of the quadrants bounded by the flow lines, with the direction of each vortex mirrored across both the lateral and dorsal midlines.

While flow in itself does not inherently generate strain, factors specific to the experimental system, such as non-uniform flow velocities and boundary conditions, determine the strain profile resulting from a given flow field. In our case, the embryo represents a closed, 3D system in which flow inherently generates strain either due to local forces inducing flow in a non-uniform manner or due to the way that the irregular shape of the embryo influences a uniform flow pattern. The presence of fixed points in the flow fields clearly illustrates this, as the embryo is a continuous surface and therefore flows must be coupled. In the following section, we discuss the strain profile associated with each of these distinct flow patterns.

3.2 Characterizing the strain profiles generated by tissue flows

3.2.1 Justification for measuring strain rate

Understanding how cells respond to stress in the context of mechanotransduction requires a method to detect when tissues are subjected to stress as well as a method to observe the

induction of the force sensitive cell behavior. While a significant area of research over the last decade has been dedicated to developing methods to precisely measure forces in living systems, such as traction force microscopy, FRET probes, and oil microdroplets, and to characterize the mechanical properties of tissues, such as magnetic droplets, micropipette aspiration, optical traps and tissue compression devices, each has its unique technical limitations or challenges that have prevented them from becoming widely generalizable to a variety of experimental systems[19–21]. Measuring strain instead offers a more accessible metric to study how tissues respond to force, as it does not require any prior knowledge or assumptions about the absolute magnitude of force or the mechanical properties[20]. Strain, generally defined as the deformation of an object in response to an applied stress, is the measure of how a material responds to a given force. Therefore, while answering certain questions, such as the force a single motor can produce, requires methods to precisely measure stress, for many other questions, such as the one that is the foundation of this thesis, the strain is more than sufficient to study how a cell responds to stress, irrespective of the absolute magnitude of that stress.

Strain is measured as the relation between the change in length and the initial length:

$$\epsilon = \frac{\Delta L}{L_0}$$

Defined as such, strain can readily and directly be quantified from reference points in the tissue, without a need to measure the stresses responsible for the measured deformation. While strain is calculated independent of time, the strain rate defines a time dependent measure of strain:

$$\dot{\epsilon} = \frac{\Delta L}{\Delta t \cdot L_0}$$

In this work, we consider the strain rate rather than strain for several reasons. Development is inherently a time dependent process: some processes occur very gradually over

long periods while others happen quickly over short time periods. While the total strain generated in two circumstances may be the same, the time over which that strain is generated, and therefore the strain rate, may vary greatly. Considering that many non-living materials exhibit time dependent behaviors and biological systems are inherently time dependent, it stands to reason that the rate of strain rather than strain itself be the more relevant quantity. Furthermore, cells and tissues are active materials that lack a reference configuration; at the cellular scale, the cytoskeleton undergoes remodeling and at the tissue scale, cells rearrange, divide, or are extruded over relatively short time periods to relax stresses and effectively create new reference configurations. As a result, over timescales longer than that of stress relaxation, it is unclear how relevant the total strain generated is for determining cell behavior. Without a defined reference state or some form of memory of the initial state, it is difficult to conceive how the cell would a) "remember" its initial state and b) measure the change between the initial and final states. On the other hand, strain rate can be measured without reference to an initial state and can be calculated between any two timepoints. This enables comparison of cell and tissue scale dynamics, as shown later in this chapter. We therefore consider strain rate as the relevant metric in this work.

3.2.2 Measuring strain rate

To measure the strain rate in the embryo, we track individual cell edges across the entire surface and measure their change in length over time. Segmenting and tracking cells in complex datasets like a developing embryo is notoriously challenging for any imaging modality, and light sheet microscopy, due to the very large number of cells (6,000 on the surface of the *Drosophila* embryo at the onset of gastrulation, all of which are visible in a

single pullback) and the relatively poor resolution compared to high NA confocal microscopy (our resolution in light sheet experiments is 0.2619 um compared to 0.08 um in the confocal datasets), is far from an exception. Nevertheless, we developed a pipeline to enable cell segmentation and tracking for a large majority of the cells in the embryo over the course of observation. First, we employ the Autocontext (2-stage) workflow in ilastik to generate a cell segmentation from the myosin fluorescence[83]. Myosin can be associated with the cell cortex

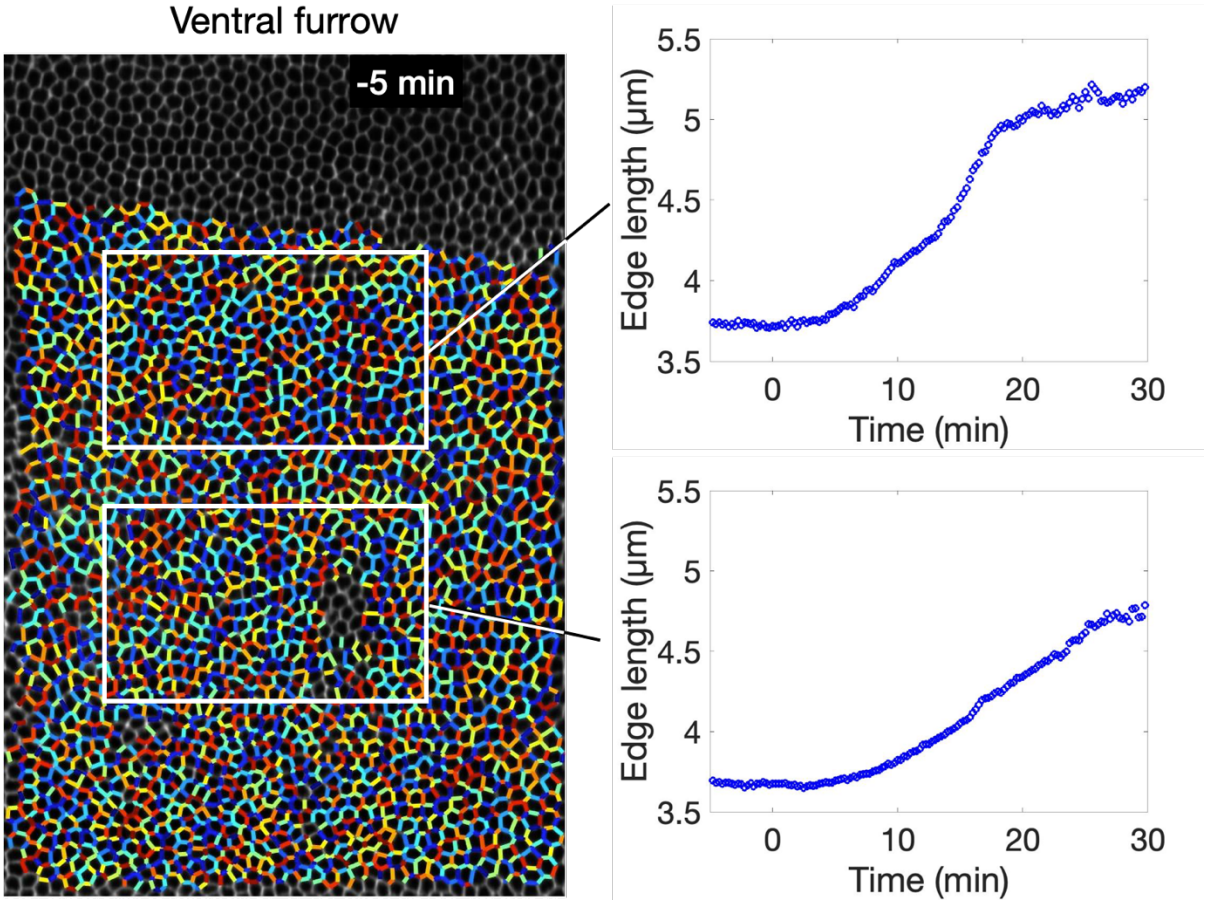

Figure 3.2: Example of cell segmentation and resultant cell edge tracking
Image shows region in germ band adjacent to VF (top) with pseudo-colored cell junctions from automated tracking superimposed. Only junctions which are tracked for the duration of the movie are labeled (note for example, the absence of labeled junctions in the top region due to the fact that those cells are internalized into the VF as it forms, and therefore their tracks are lost). The white boxes designate two regions within which the average junction lengths over time were measured, shown in the corresponding plots on the right. From these plots, it is clear that edge length increases over time, with the rate of increase larger in regions closer to the VF (top vs bottom plot).

or present in the inactive form in the cytoplasm, but it is excluded from the nucleus. Even for cell edges that don't accumulate significant levels of junctional myosin, such as the edges parallel to the A-P axis in the germ-band during GBE, there are low levels of myosin associated with the cell cortex to make up the base level actomyosin cytoskeleton, which is detectable over the cytoplasmic pool, although not without some difficulty. Therefore, the classifier can be trained to distinguish the three levels of myosin intensity to facilitate segmentation: (relatively) high intensity values at the cell edges, moderate intensity values in the cytoplasm, and low (background) intensity levels in the nuclei. The resulting cell segmentation is then input into a custom MATLAB script which identifies the cell edges in each time point (Figure 3.2, left) and matches them between timepoints based on proximity. The edge endpoints are used to measure the edge length over time, from which the strain rate is calculated (Figure 3.2, right), and this method is used to characterize the global strain profile over time.

3.2.3 Description of strain profile

At the initiation of gastrulation, there is no detectable strain in the embryo due to the absence of flow at this time. Even the small, dorsal flow following the completion of cellularization barely influences the strain profile in the embryo, as the flow is relatively weak and therefore stretches the cells very little. The first detectable strain generated in the embryo occurs at the ventral midline when apical constriction to form the VF begins. These cells exhibit a strongly negative strain rate as they rapidly constrict along the D-V axis. As they do so, they stretch the cells to which they are connected, inducing a positive strain rate, as these cells undergo lengthening along the D-V axis. This effect begins as a modest increase in strain rate in only the cells directly adjacent to the VF. However, over time, as more of the ventral cells are

internalized into the forming furrow, the effect propagates as more and more cell stretching is required to compensate for the cells leaving the surface. Within a single timepoint, this is clearly visible by the gradient in cell strain along the D-V axis, which is highest in the region directly adjacent to the VF and lowest at the dorsal pole. Cell eccentricity, which can be used as a readout for the degree of cell stretching, provides a useful metric to visualize this process.

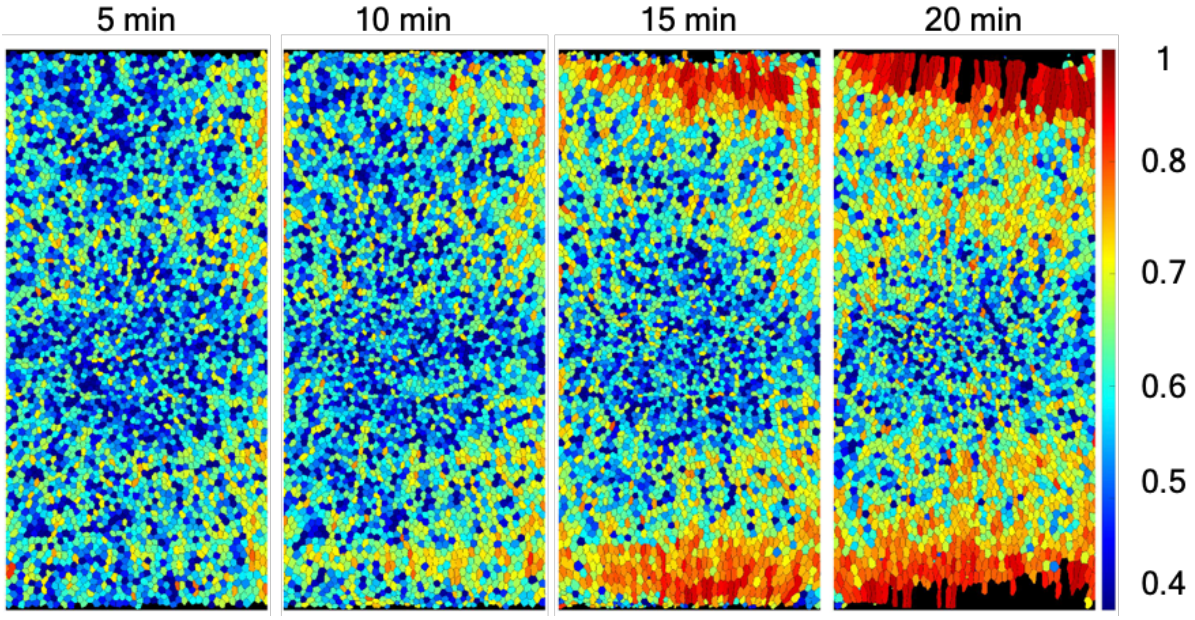

Figure 3.3: Heat map of cell eccentricity as readout of cell strain during VF formation
Each panel corresponds to the same region: height is full circumference along the D-V axis and width is 250 um immediately posterior to the CF, corresponding to the germ-band. Time stamps are given relative to CF formation. At the onset of VF formation (left), cell eccentricity, and therefore strain, is low (cells are not stretched) in all regions. As VF formation progresses (left to right), cell eccentricity increases beginning adjacent to the VF and moving dorsally over time, as the internalization of cells at the ventral midline to form the VF stretch the remaining cells along the D-V axis, generating the observed strain gradient.

If cells are stretched preferentially along one axis, then their aspect ratio will increase, indicating that they are deformed and therefore strained. This effect can be seen clearly in a heatmap of cell eccentricity (Figure 3.3) in which all cells in the central, or trunk, region of the embryo have low aspect ratios and are consequently unstretched (left) prior to initiation of VF formation. However, as the VF forms, cells closest to it begin to undergo stretching, evidenced

by the increase in eccentricity, and over time the degree to which cells are stretched as well as the distance from the furrow at which cells still experience stretching increases (left to right). The appearance of this gradient and its steepening over time can be understood by examining the rate of strain along the D-V axis. The strain rate is greatest in the regions just dorsal to the VF and decreases monotonically along the ventral to dorsal axis (Figure 3.4).

This pattern is consistent with the propagation of force by the internalizing VF. Cells are mechanically coupled through adhesive complexes, allowing forces to be propagated across tissues. While such a force propagated in an elastic material without dissipative forces would create a uniform pattern of strain along the circumference, the embryo has been shown to experience dissipation due to frictional forces between the apical surface of the epithelium and the vitelline membrane[89]. This leads to a decay in the magnitude of force with increasing distance from the source, with the result being a gradient in the strain generated along the D-V axis, the steepness of which is determined by the amount of friction.

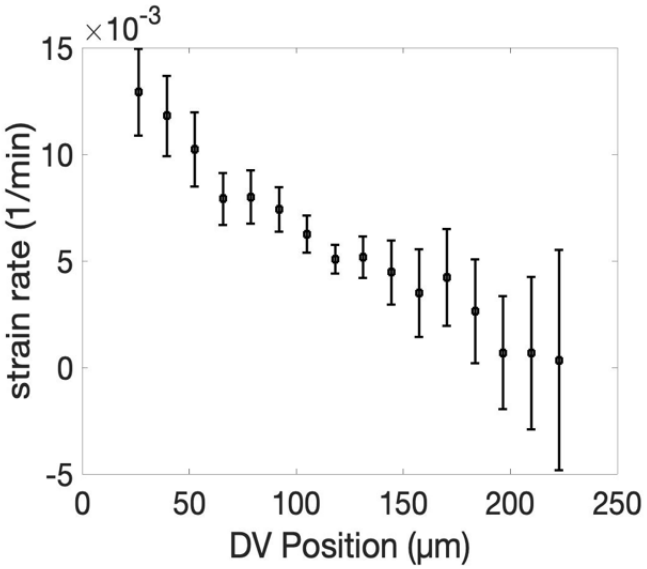

Figure 3.4: Strain rate as a function of position
Embryo is divided into discrete bins along the D-V axis, and strain rates are averaged within each bin, producing a clear D-V gradient.

3.3 Measuring myosin dynamics across the entire embryo surface

While the myosin anisotropy driving GBE has been widely studied, the characterization of this distribution outside of a small range of developmental times and space has been limited.

However, understanding how the myosin distribution relates to the global strain profile requires a complete view of the myosin dynamics, from the onset of anisotropy through the fast phase of GBE. To this end, we performed in toto time lapse imaging of embryos expressing a fluorescently tagged NMII regulatory light chain (spaghetti squash) and quantified the myosin profile across the entire embryo surface.

3.3.1 Measuring myosin accumulation

There are a variety of metrics one can use to measure changes in the myosin signal over time and space, and there are several important factors to consider when choosing a metric. One factor to consider for time lapse image is photobleaching; even though light sheet microscopy is a much gentler form of imaging compared to confocal microscopy, some amount of bleaching of the fluorophores is inevitable. Therefore, comparing total intensity of earlier time points to later time points is not a reasonable approach without some form of normalization to account for the gradual reduction in fluorophore intensity over time. In addition to allowing comparison within a sample over time, the method of normalization should enable comparison across embryos. Even when the same fluorescently tagged protein construct is imaged with the same setup and settings, many factors can contribute to the total intensity levels in different embryos.

To address these factors, we define the junctional myosin accumulation (m) as:

$$m = \frac{I_{junction} - I_{cytoplasm}}{I_{cytoplasm}}$$

(Figure 3.5), and the rate of change of the junctional myosin is given by:

$$\dot{m} = d\frac{m}{dt}$$

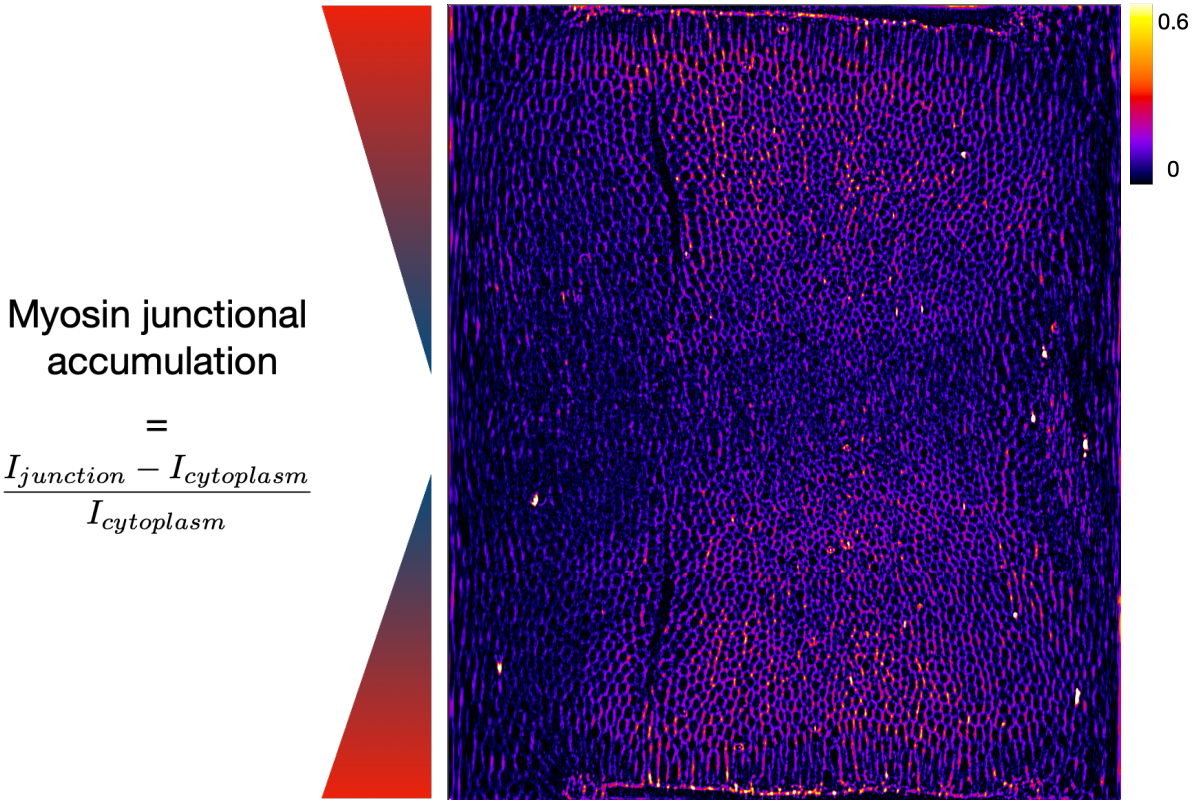

Figure 3.5: Heat map of junctional myosin accumulation
Junctional myosin accumulation, calculated according to the equation on the left, for a timepoint just before the onset of GBE. Triangles serve as a visual aid to highlight the gradient in junctional myosin visible along the D-V axis, with high levels adjacent to the VF (top and bottom) and baseline levels at the dorsal pole (center).

Previous studies of the myosin distribution during GBE have typically quantified myosin with a measure that compares the intensity on vertical (D-V parallel) to horizontal (A-P parallel) junctions to determine the so called enrichment of myosin on vertical edges. While this metric proves useful for describing the myosin anisotropy at any given point during GBE, it has several shortcomings when applied more broadly to describe the myosin profile over time and space. Firstly, such measures do not account for total myosin intensity on junctions, only the relative intensity between junctions. Therefore, cells uniformly expressing high junctional myosin levels and uniformly expressing low junctional myosin levels can have similar values, despite the potentially drastically different total myosin levels. Secondly, many

changes in myosin distribution can be effectively masked by this type of measure; for example, increases in myosin levels on vertical junctions or decreases in myosin levels on horizontal junctions will result in similar changes to the enrichment value. A thorough understanding of the myosin dynamics, however, requires the ability to distinguish between the various changes, particularly in the context of a strain dependent myosin recruitment hypothesis. The junctional myosin accumulation allows us to quantify the changes of myosin on all junctions independently of other junctions, while normalization to the cytoplasmic pool enables comparison over time and across embryos.

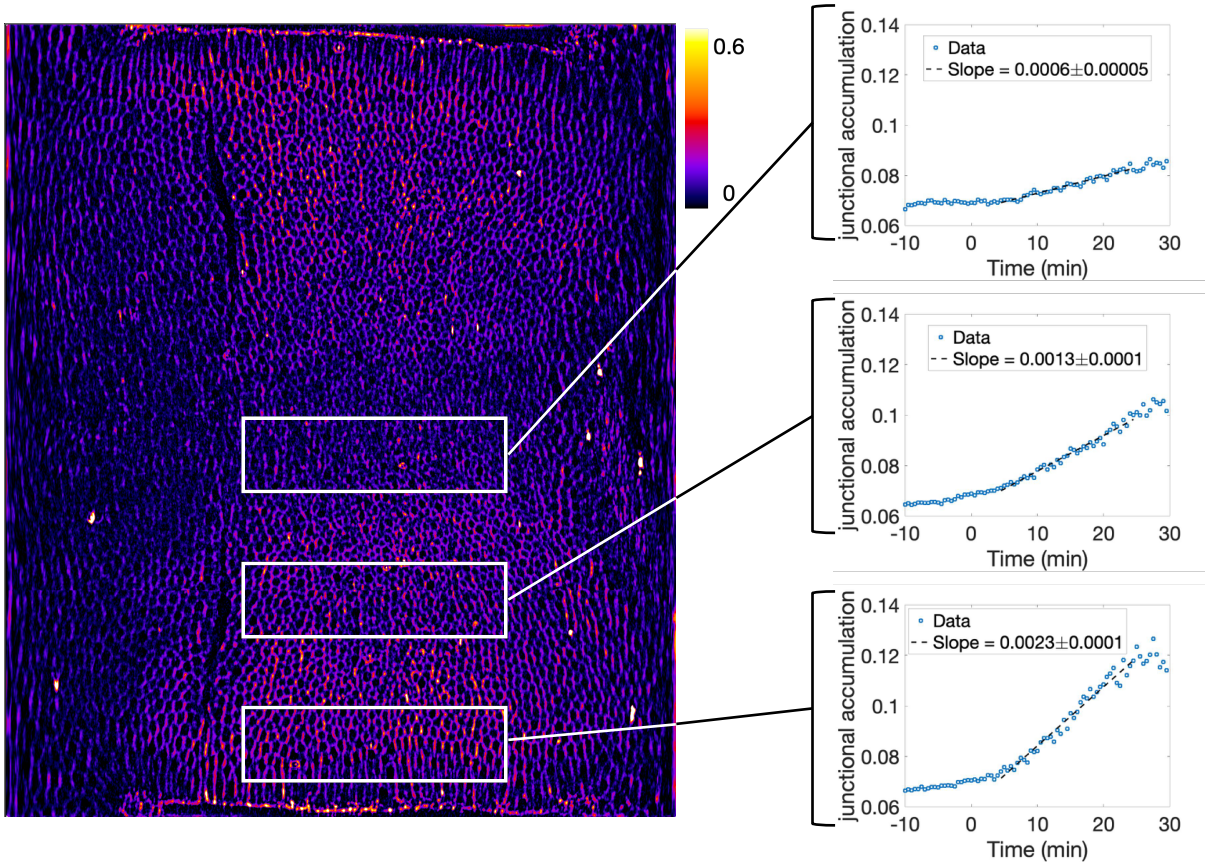

Figure 3.6: Junctional myosin accumulation over time for discrete regions along the D-V axis

Same heat map as Figure 3.4. The D-V axis is subdivided into regions (white boxes) within which the junctional myosin accumulation is averaged for each time point to produce the corresponding plots (right) of the junctional myosin accumulation over time. The slope for the linear region of the graph, roughly corresponding to the period of VF formation, is shown in each inset, and increases from dorsal (top right) to ventrolateral (bottom right).

3.3.2 Description of myosin profile across space and time

With the exception of ([16]), descriptions of the myosin profile driving GBE have been restricted to small regions in the central germ-band, typically taken around embryonic stage 8, well after the myosin profile has been established and, consequently, GBE has begun. As a result, little is known about how this profile evolves over time and space. We therefore set out to thoroughly quantify the myosin dynamics during this time period over the entire surface of the embryo. At the completion of cellularization, there is very little junctional myosin accumulation anywhere in the embryo. The onset of gastrulation is marked by the apical accumulation of myosin in the ventral region, initiating formation of the VF. Shortly after this process begins, and the ventral cells begin constricting to cause tissue bending and invagination, junctional myosin accumulation becomes detectable in the germ-band and increases as VF formation proceeds. Interestingly, the junctional myosin accumulation increases more quickly, i.e. has a higher rate, for edges adjacent to the VF than it does for those farther away, which is visible by the slope of the myosin accumulation over time (Figure 3.6). This gradient of myosin accumulation rate (Figure 3.7) produces a clear gradient in the level of junctional myosin accumulation along the D-V axis (Figure 3.5).

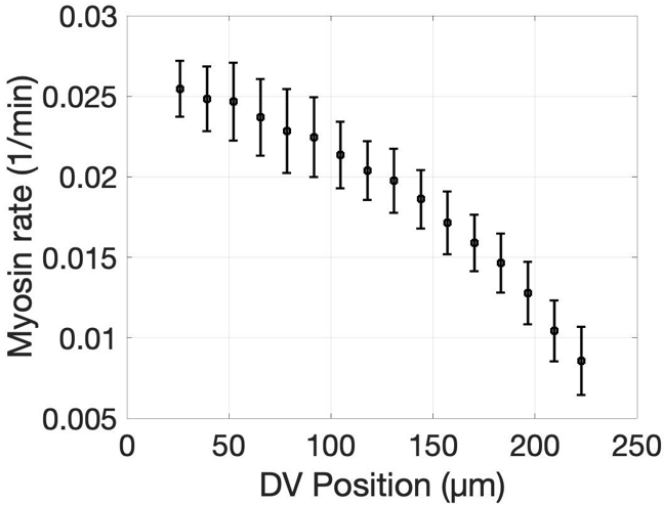

Figure 3.7: Myosin rate as a function of position
Myosin rate averaged across the D-V axis for the same regions as the strain rate in Figure 3.4. As with strain rate, myosin rate exhibits a clear D-V gradient.

3.4 Comparison of strain rate and myosin rate profiles

The strain and myosin profiles show a clear gradient: the rates of both monotonically decrease from ventral to dorsal regions following a very similar trend. Indeed, plotting the myosin rate as a function of strain rate produces a near linear relationship, which appears to saturate at the upper end of the strain rate range. While further studies would be required, it suggests a limit to the amount of myosin recruited in response to large deformations which could be due to saturation of myosin binding to actin filaments, depletion of the cytoplasmic pool, or full extension of the strain sensor such that additional strain input cannot be translated to additional myosin (such as a protein that unfolds in response to stress but has a discrete number of domains that can undergo unfolding). Addressing these possibilities would be of great interest, although as they in part depend on the underlying mechanism for myosin recruitment, we instead turn toward a further examination of the possibility of strain dependent myosin recruitment. Based on the strong correlation evident in the prior analysis, we asked whether such correlation was due to a causal relationship. To this end, we designed an experimental procedure to induce ectopic strains and measure the resulting changes, or lack thereof, in the myosin distribution. While this analysis is the subject of the next chapter, we first turn to a single junction analysis of strain and myosin dynamics to better understand the nature of the observed correlation.

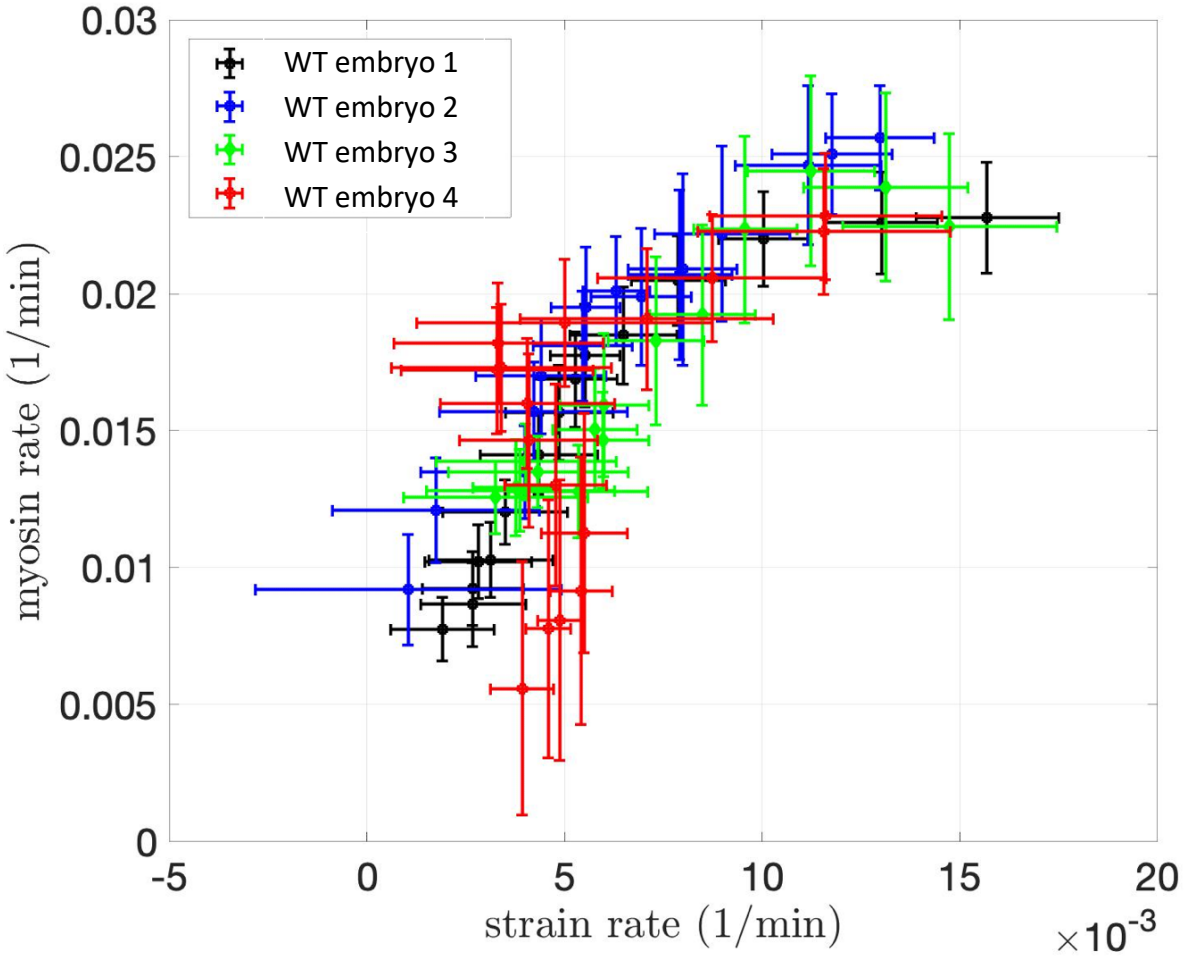

Figure 3.8: Plot of myosin rate vs strain rate for wild type embryos
Strain rates and the corresponding myosin rates measured as in Figure 3.4 and 3.7. Colors correspond to individual embryos. Each data point corresponds to a region along the D-V axis at a given time. Error bars represent SEM. Data points largely fall on a single line, particularly in the middle range of the values, indicating a strong correlation between strain rate and myosin rate across the embryo in space and time.

3.5 Single junction analysis of strain and myosin dynamics

The embryo scale analysis shows a clear correlation across space in the strain and myosin dynamics, yet a more thorough understanding of the short time and length scale behavior is necessary to elucidate details of the dynamics that may otherwise be hidden. Although the temporal and spatial resolution for the light sheet microscope is more than adequately high for the purpose of developmental dynamics, cytoskeletal remodeling can happen on much shorter timescales, and therefore may be averaged out in our embryo scale analysis. To examine this possibility, we turned to confocal imaging for higher temporal and spatial analysis of strain and myosin dynamics. We imaged regions of the germ-band in embryos expressing a membrane tagged cherry fluorescent protein and a GFP fused myosin light chain (spaghetti squash) over the period beginning before the VF has initiated through the fast phase of GBE (Figure 3.9). Strain, measured in the same way as before, and myosin, quantified as the line density on a cell edge over time, are measured simultaneously at a temporal resolution of approximately 5 seconds. This time scale is comparable, if not significantly faster than, the time scales at which the cytoskeleton undergoes remodeling and is therefore adequate to capture processes that may be occurring at rates faster than the temporal resolution of the light sheet.

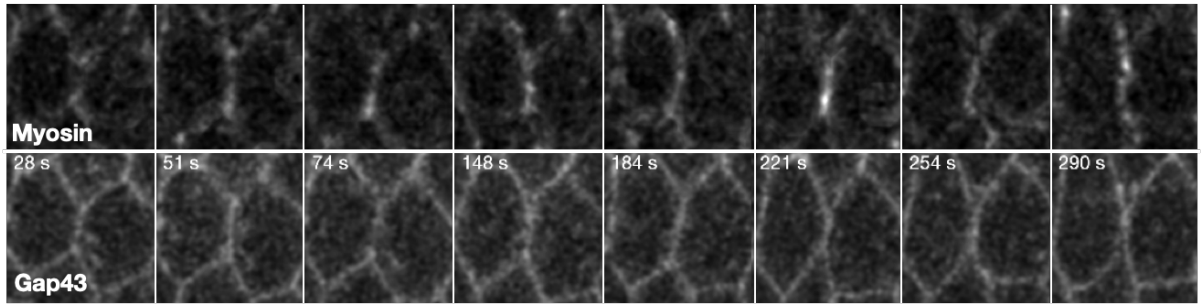

Figure 3.9: Confocal time course of cell expressing membrane and myosin markers
Example of typical cell edge acquired by high spatial and temporal resolution confocal time lapse imaging from which single edge strain and myosin dynamics are measured. Time points are chosen to demonstrate significant changes in junction length and myosin signal.

In this way, we observe that both strain and myosin intensity are seen to oscillate, even as average junction length decreases, as during a cell intercalation event. A representative junction (Figure 3.9) and the associated junction length (Figure 3.10a) and myosin intensity (Figure 3.10b) traces are shown. Using these time traces to calculate the strain and myosin rates shows that these values also appear to oscillate with some regularity (Figure 3.10c). While these oscillations are clear from the raw data, further analysis is required to extract patterns, if any, from the oscillatory behavior. We consequently perform auto- and cross- correlation analyses (Figure 3.10d). Autocorrelation of both the strain rate (black) and myosin rate (red) gives a minimum with a time shift of +/- 37 seconds, indicating that each undergo regular oscillations with a period of 74 seconds. Cross-correlation of strain rate and myosin rate (green) shows a maximal positive correlation with a time shift of 30 seconds and a minimal, negative correlation with a time shift of -7 seconds. This indicates that the strain rate and myosin rate undergo oscillations that are phase-shifted by almost half a period and are therefore nearly anti-correlated. These out of phase oscillations are consistent with the effects of cell stretching, which will dilute the concentration of fluorescently tagged myosin motors on that junction, and myosin recruitment to a cell edge, which will cause subsequent contraction of that edge. Furthermore, the cross-correlation of strain rate with the rate of change of the membrane marker (gray) exhibits no significant correlations with any time shift, supporting a specific relationship between the strain rate and myosin rates.

We next asked about the response of myosin to deformation on the same edge. To this end, we aligned the strain and myosin rate traces from various edges to significant peaks in strain rate and averaged the resulting peak aligned strain and myosin rate traces (Figure 3.10e). As expected, this produces a strain rate curve with a global maximum at 0 flanked by global

minima on either side at approximately +/- 30 seconds, consistent with the previous analysis. The myosin rate exhibits a minimum at about -7 seconds and a global maximum at about 30 seconds, which is again consistent with the autocorrelation analysis. However, the first myosin rate minimum following the strain rate peak does not occur until just over 100 seconds, representing a significantly elongated cycle compared to the 74 seconds given by the autocorrelation. Therefore, a significant peak in strain rate not only precedes a peak in myosin rate but also increases the period of the myosin rate oscillations for at least the half cycle immediately following the strain peak. The effect can additionally be seen when observing the

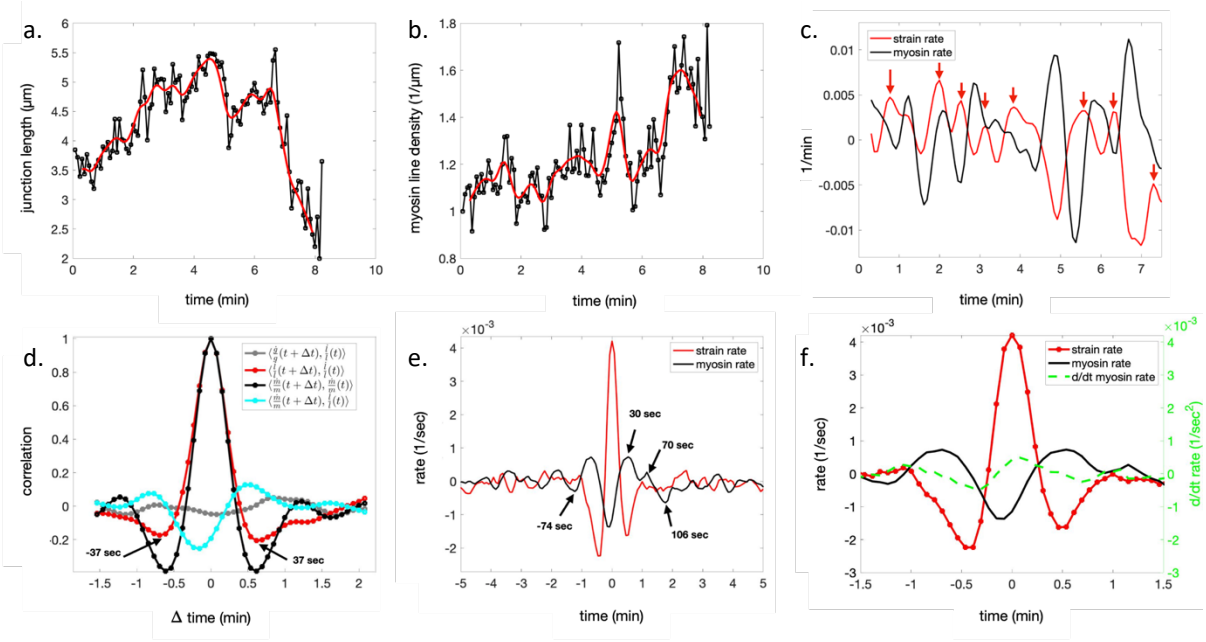

Figure 3.10: Single junction dynamics of strain and myosin from confocal data
a. Length of junction shown in Figure 3.9 over the course of acquisition. b. Myosin line density for the same junction measured in (a). c. Strain and myosin rates obtained from the junction length and myosin line density, respectively. Red arrows show significant peaks in strain rate. d. Correlation analysis. Auto-correlation of strain rate (black) and myosin rate (red) both show minima at +/- 37 seconds. Cross correlation of strain rate with myosin rate (green) has a minimum at -7 seconds and a maximum at +30 seconds, while the cross-correlation of strain rate with membrane rate (gray) does not show any significant correlation. e. Strain peak aligned average strain rate (red) and myosin rate (black) curves. Arrows mark minima and maxima with associated time stamp. f. Same plot in (e) zoomed in on the time frame corresponding to one myosin cycle before and after the strain peak. Green dashed line shows the change in myosin rate.

change in myosin rate, or myosin acceleration, over time (Figure 3.10f). The myosin acceleration begins to increase shortly after the strain rate begins to increase and peaks shortly after the strain rate peaks. Furthermore, after the initial peak in myosin acceleration, the rate does not become significantly negative again for at least the next minute, corresponding to the elongated myosin rate cycle following the strain peak, which persists for just over 100 seconds. Together, these results support the embryo wide correlation between strain and myosin rates to suggest that there is a causative relationship. We therefore set out to test the potential causality in the strain and myosin dynamics through an optogenetic method to induce ectopic strains, which is the topic of Chapter 4. But first, we turn to physical modeling in an attempt to capture these observations and furthermore to explore the predicted effects of incorporating mechanical feedback.

3.6 An oscillator model incorporating mechanical feedback recapitulates single junction dynamics

Our observations of the antiphasic relationship between strain rate and myosin rate led us to ask whether we could capture these dynamics, in an effort to better understand them, with a simple physical model. In the most basic representation, cell edges can be thought of as elastic springs that can be elongated by external tension or contracted by the motor activity of myosin. The change in edge length is therefore determined by the balance of external and internal forces, while oscillations between states of contraction and elongation are sustained by the effects of concentration/dilution, non-linearity, and myosin turnover. Previous work has captured the dynamics of the apical myosin pool and oscillations of cell area using a concentration oscillator model based on the interplay of these factors[90]. As a cell edge

contracts, myosin becomes more concentrated, therefore driving the contraction phase further. Conversely, as a cell edge is stretched, the myosin concentration is lowered due to dilution, such that the edge elongates even faster. Neither of these situations is stable, and therefore any tension fluctuations would lead to runaway junction length change in one direction or the other.

The model therefore introduces two additional features. The first is a non-linearity in the form of strain-stiffening, which acts to balance the tension in the edge to halt elongation or contraction. The second is myosin turnover which acts to restore the myosin concentration to the equilibrium value in the form of myosin on and off rates[77]. As a result, when the edge is contracted and the myosin concentration is therefore much higher than the equilibrium value, turnover will lead to myosin being removed from that edge. As it does so, the external tension on the edge is no longer balanced, and the edge will begin to elongate. In the opposite situation, edge elongation leads to myosin dilution, and turnover will act by adding myosin to the cell edge to reach the equilibrium value. As additional myosin motors are added, the internal tension on the edge by the myosin motors increases above the external tension, leading to edge contraction. In this way, stable oscillations about an equilibrium myosin value and junction rest length can be achieved.

However, our single junction data shows oscillations about an average myosin level and junction length that change over time. We therefore asked if we could also capture the observed changes in average junction length on longer time scales. In close collaboration with Nikolas Claussen, who performed the theoretical modeling and associated simulations, we adapted the concentration oscillator model by incorporating viscoelastic-relaxation and mechanical feedback, as proposed in ([77]) to determine whether the adapted model could recapitulate our data. The former represents turnover of the cytoskeleton, which acts to adjust

the junction rest length, while the latter acts to change the equilibrium myosin level in response to strain.

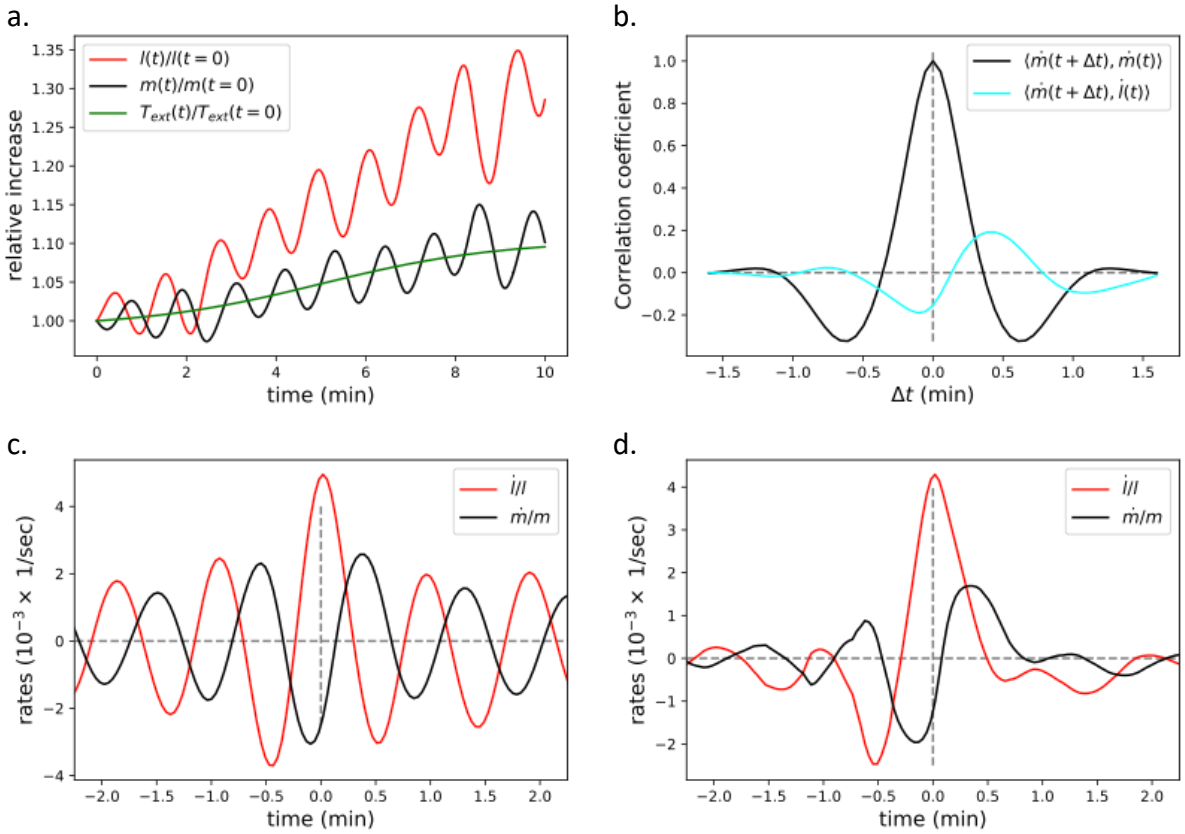

Figure 3.11: Simulation results from adapted concentration oscillator model with mechanical feedback
a. Average relative increase of strain rate (red) and myosin rate (black) in response to the imposed external tension (blue). b. Autocorrelation of myosin rate (black) and cross correlation of strain rate and myosin rate (green) analysis calculated from traces in (a). c. Average strain rate (red) and myosin rate (black) curves after aligning to strain rate peaks (as in Figure 3.10.e,f) for simple oscillation model. d. Same as in (c) but simulated with extended model incorporating viscoelastic relaxation and mechanical feedback.

Edge dynamics and myosin levels are simulated for cell edges according to the equations of the model (details of the model and simulations are described in the supplementary information in Gustafson et al 2022). The extended oscillation model (incorporating viscoelastic relaxation and mechanical feedback) recapitulates the oscillations in junction length and myosin levels as well as the change in average levels in response to

external tension (Figure 3.11.a). The correlation coefficients for the myosin rate autocorrelation and the strain rate and myosin rate cross-correlation analysis also recapitulate those calculated from the single junction data (Figure 3.11.b, compare to Figure 3.10.d). Whereas the simple oscillation model (without viscoelastic relaxation and mechanical feedback) shows stable oscillations in the strain peak aligned strain and myosin rate curves (Figure 3.11.c), the extended model exhibits dampening oscillations, which captures the measured dynamics including key features in the curves (Figure 3.11.d, compare to Figure 3.10.e,f). Of note, the simulation accurately reproduces the asymmetry in the myosin curve, compared to the nearly symmetric curve in the simple model, in which the period of the myosin cycle is extended following the strain rate peak, which we had attributed to strain rate based myosin recruitment in the experimental data. Overall, our model provides strong theoretical support to suggest that mechanical feedback can account for the experimentally observed dynamics.

3.7 Discussion

By examining both the strain profile and myosin distribution globally, we are able to observe several patterns that have not been described previously, despite the abundance of research concerning the establishment of the myosin anisotropy during this period. First, we identify a gradient in the rate of strain along the D-V axis that is consistent with the effects of force propagation and stress relaxation from the internalizing VF. The loss of a significant portion of the cells around the circumference of the embryo combined with the need to maintain epithelial integrity leads to substantial stretching of cells across the D-V axis in order to compensate for those cells lost from the surface. The degree of stretching is highest in the cells

directly adjacent to the VF and decreases towards the dorsal pole, which accounts for the observed strain gradient. We next characterized the myosin distribution and observed a striking gradient in both myosin accumulation and rate that closely resembles the gradient in strain, providing initial positive support for the hypothesis proposed in this thesis. Previous works characterizing the myosin distribution driving GBE have not described such a gradient in the myosin profile, or in the PRGs or TLRs reported to be upstream of it, likely because the local nature of previous analyses inhibited its identification. Intriguingly, recent work of a similarly quantitative global view has explored the expression levels of PRGs and TLRs along the D-V axis and found that they qualitatively resemble that of the myosin distribution[91]. Furthermore, their model to predict myosin distribution based on combinatorial effects of various PRGs and TLRs recapitulates the D-V gradient in the myosin profile while failing to capture the characteristic shape of the myosin profile along the A-P axis. Combined with the results presented here, this creates an intriguing possibility that TLRs are associated with establishing the D-V gradient of myosin rather than the anisotropic distribution itself.

While this possibility may at first seem to contradict the previous literature indicating an important role for TLRs in establishing the anisotropic myosin profile, it rather suggests that TLRs indeed contribute but that additional inputs are likely necessary to fully account for the myosin distribution. In fact, this is consistent with previous work examining PRG mutants in which a significant portion of myosin anisotropy is maintained[12] and the fast phase of GBE is unaffected[69]. This discrepancy remains to be reconciled, yet the similarity between the strain and myosin profiles, as well as other preliminary evidence, supports a potential role for a mechanical feedback mechanism for myosin recruitment. We examine this possibility further in light of additional results presented in the following chapter.

The relationship between strain and myosin is further corroborated by the single junction analysis, which suggests that a strong deformation leads to an accumulation of myosin. The cell scale data therefore helps elucidate the physical mechanism by which strain rate recruits myosin, and physical modeling consistent with this mechanism accurately recapitulates these dynamics. Importantly, a simple concentration oscillator model does not fit some of the key features of the strain and myosin dynamics, whereas an adapted version including two additional, biologically plausible features- viscoelastic relaxation and mechanical feedback- does with surprising fidelity, providing further support that mechanical feedback is acting in the system[77]. Confirming this prediction requires carefully designed experiments to test causality, and therefore, the next chapter details our findings from the experimental design detailed in Chapter 2 Section 3 to test precisely this potential causation.

Chapter 4:

An optogenetic method to demonstrate strain rate dependent myosin recruitment

The embryo wide quantification described in the previous chapter permitted us to uncover a strong global correlation between strain and myosin rates that is supported by the dynamics at the level of single junctions, leading us to ask whether this might be a causal relationship. Indeed, previous works have strongly implicated a role for stress in recruiting myosin, although definitive evidence remains inadequate. Therefore, demonstrating causality requires a method to induce strain in a way that addresses the previous shortcomings and allows unambiguous interpretation of the myosin response. Chapter 2 Section 3 describes these shortcomings as well as our experimental design to address them, while the following chapter details the findings from these experiments. As discussed in that section, our setup and experimental

criteria makes the precise positioning and timing extremely challenging, but performing many such activations results in adequately similar experiments. Additionally, the same versatility that makes reproducibility more challenging provides interesting opportunities to examine how the embryo responds to deformations of varying regions, strengths, and times. Furthermore, we are able to distinguish general responses from those that are specific to the given experimental parameters. Notably, in all cases that strain is induced by the activation, we observe a corresponding increase in myosin, yet we observe differences in this response according to the region probed. This chapter therefore characterizes the observed response as well as some of the additional details of the mechanism uncovered by the various activation strategies.

4.1 Inducing strains along the D-V axis

As described previously, activating in one or more planes will create two lines of variable thickness that constrict, generating strain along the D-V axis. These experiments offer a relatively simple proof of concept, so we began here. An example of one such experiment can be seen in Figure 4.1, in which the activation has created two thin lines of actomyosin contractility approximately centered about the dorsal midline. As the cells within each activation line contract, they form thin furrows and stretch the adjacent cells.

The result of such an activation is clearly evidenced by observing the changes in cell shape and flow following activation. Tracking cells for the time period before activation shows that there is little net movement of cells and therefore very little flow (Figure 4.2, top left). In contrast, a significant flow is induced immediately following activation indicated by the cell trajectories, showing cells flowing toward each of the activation lines flanking the region (Figure 4.2, bottom left). This opposing flow stretches the intervening region, leading to a

significant increase in cell eccentricity following activation as compared to before (Figure 4.2, top vs. bottom right). This increase in cell eccentricity indicates that the induced flow is causing elongation of the cells, i.e. they are being strained. These two measurements therefore serve as confirmation that the optogenetic activation strategy is functioning as designed to induce ectopic strains and that the primary direction of strain is parallel to the D-V axis.

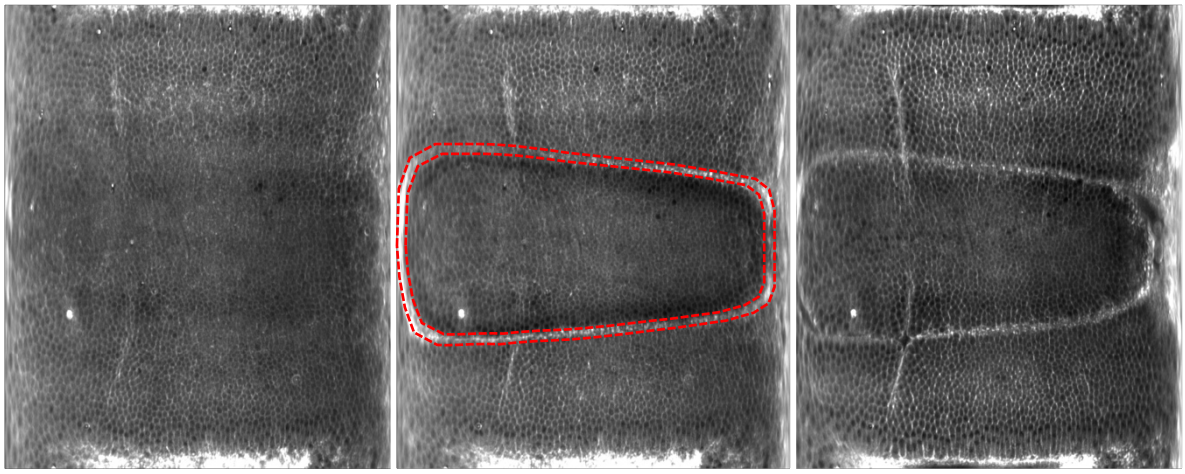

Figure 4.1: Example of raw pullbacks from optogenetic perturbation in a single plane Pullbacks generated from 3D light sheet images of an embryo expressing the optogenetic construct and a cherry fluorescent protein tagged myosin light chain (spaghetti squash) activated in a single plane centered about the dorsal pole. Left: 1 minute prior to activation. Center: Immediately following activation. Right: 10 minutes post activation. Red dashed lines show approximate outline of activated region.

The formation of these small furrows and resulting induction of strain leads to a visible accumulation of myosin in the direction of stretch. To quantify this effect, we again use the junctional myosin accumulation to characterize the myosin levels before and after activation (Figure 4.3). Before activation (t = -1 min), junctional myosin accumulation is low everywhere and comparable to control embryos. Upon activation, myosin is strongly recruited to the activated region (t= 0 min), leading to contraction of those cells (t = 1-7 min). Consequently, a significant increase in junctional myosin is observed in the tissue outside of the activated region on junctions that are perpendicular to the activation line (t = 1-7 min). In striking

contrast, control embryos exhibit very low myosin accumulation on any junctions (Figure 4.3, bottom), consistent with the low levels of dorsal myosin measured in the previous section. This result demonstrates that changing the strain profile by inducing ectopic strain leads to measurable changes in the myosin profile. In particular, locally increasing strain rates leads to increases in myosin accumulation in the direction of strain.

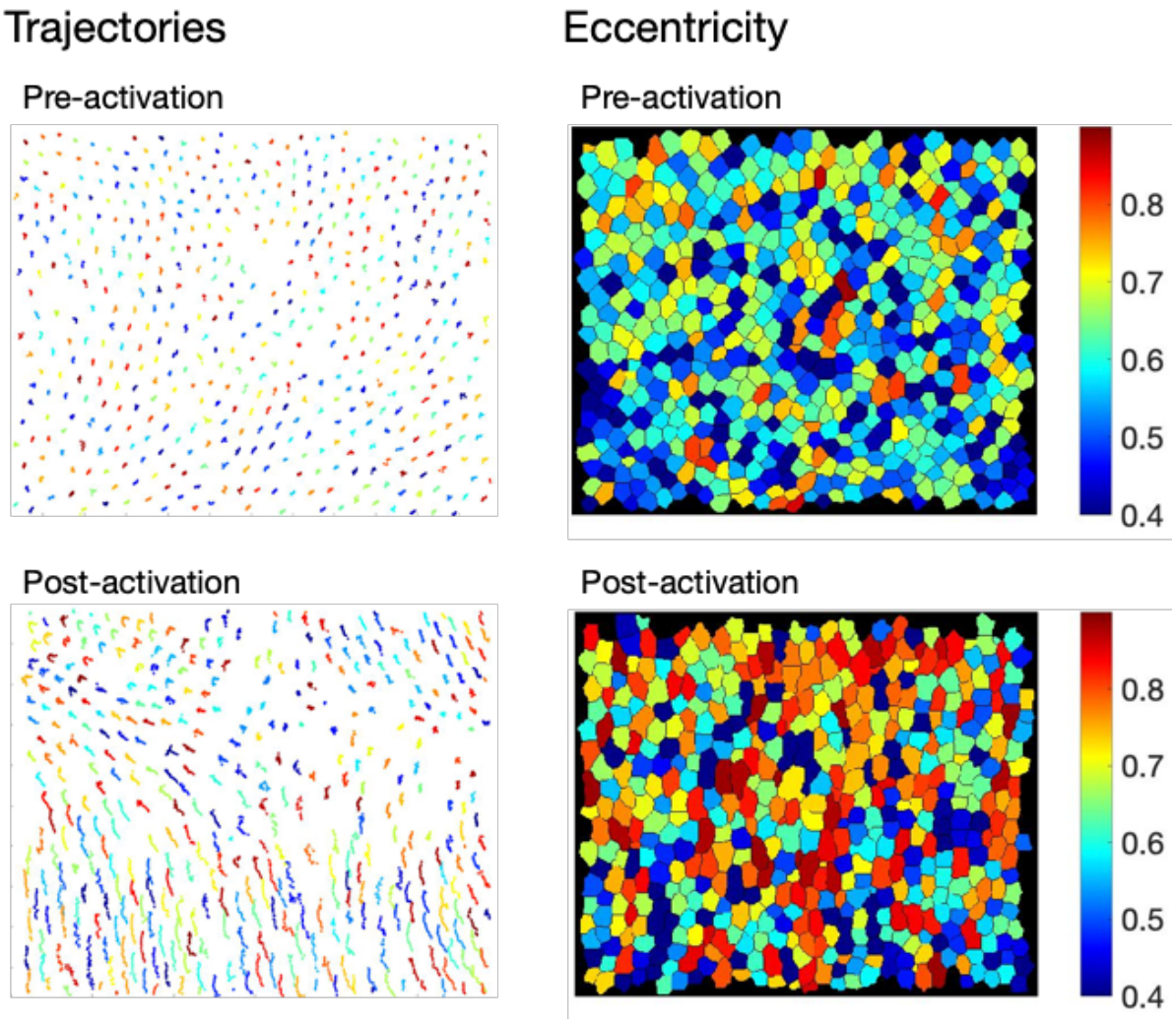

Figure 4.2: Confirmation of strain induced by optogenetic actomyosin contractility
Left: Cell trajectories show tracking of cells for the 5 minutes before (top) and 5 minutes following (bottom) activation. Right: Heat maps of cell eccentricity 1 min before (top) and 5 min after (bottom) activation. All panels show same region located between lines of activation on the dorsal pole of an embryo activated in a plane.

We repeat these experiments for many embryos and quantify the strain and myosin rates before and after activation in one or more regions of each embryo. By plotting the myosin rates as a function of strain rate for these regions pre- and post- activation, we observe in all cases that an increase in strain rate is measured following activation, a proportional increase in myosin rate is also observed (Figure 4.4). Interestingly, the data points from both before and after activation fall on the wild type curve described previously (Figure 3.8).

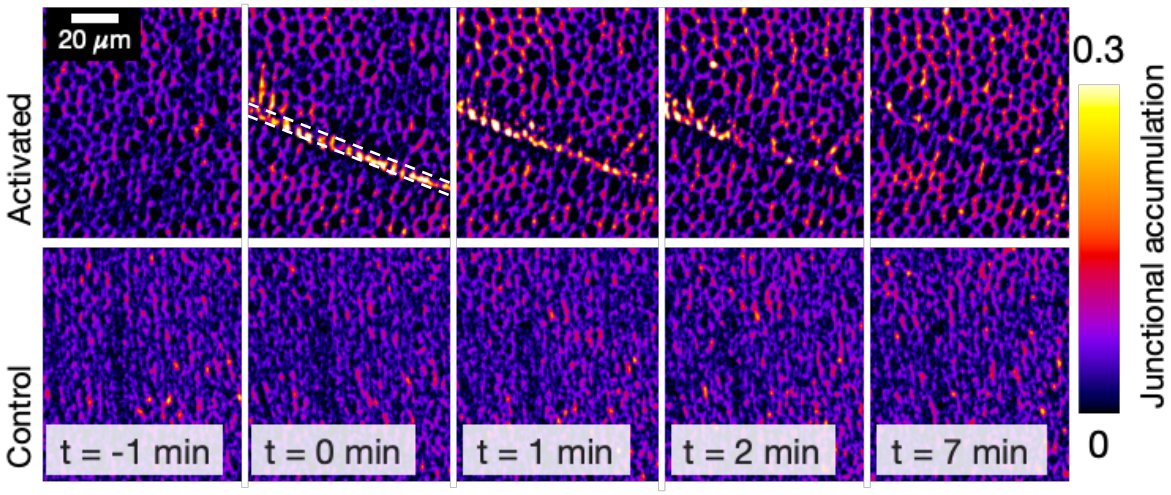

Figure 4.3: Junctional myosin accumulation in optogenetically activated embryo
Top: Region on the dorsal side of an embryo activated in two lines (only a portion of one line is shown). White dashed lines give approximate outline of activation. Bottom: Same region from an unactivated control embryo of equivalent time.

From these experiments, we conclude that strain based mechanical feedback is recruiting myosin, where junctions parallel to the induced strain have increased myosin accumulation. With the activation strategy utilized, this strain is always primarily directed along the D-V axis. As the VF generates strain along the D-V axis as well, the ectopic strain is parallel to the endogenous strain direction during this stage. Therefore, we have thusfar demonstrated the accumulation of myosin due to ectopic strain in contexts in which significant myosin accumulation is not normally observed, i.e. on the dorsal pole; nevertheless, the induced myosin accumulation follows the same pattern as the normal myosin profile. It is

therefore conceivable that while strain from the invaginating VF recruits myosin during GBE, the A-P patterning elements previously identified as having a role in the myosin anisotropy are involved in this mechanical feedback mechanism, for example by patterning one or more of the components required to enact this response. The implication of this possibility is that mechanical feedback should act only in the direction permitted by A-P patterning, or on junctions parallel to the D-V axis. To address this possibility, we next devised an activation strategy that would induce strain orthogonal to the endogenous strain profile.

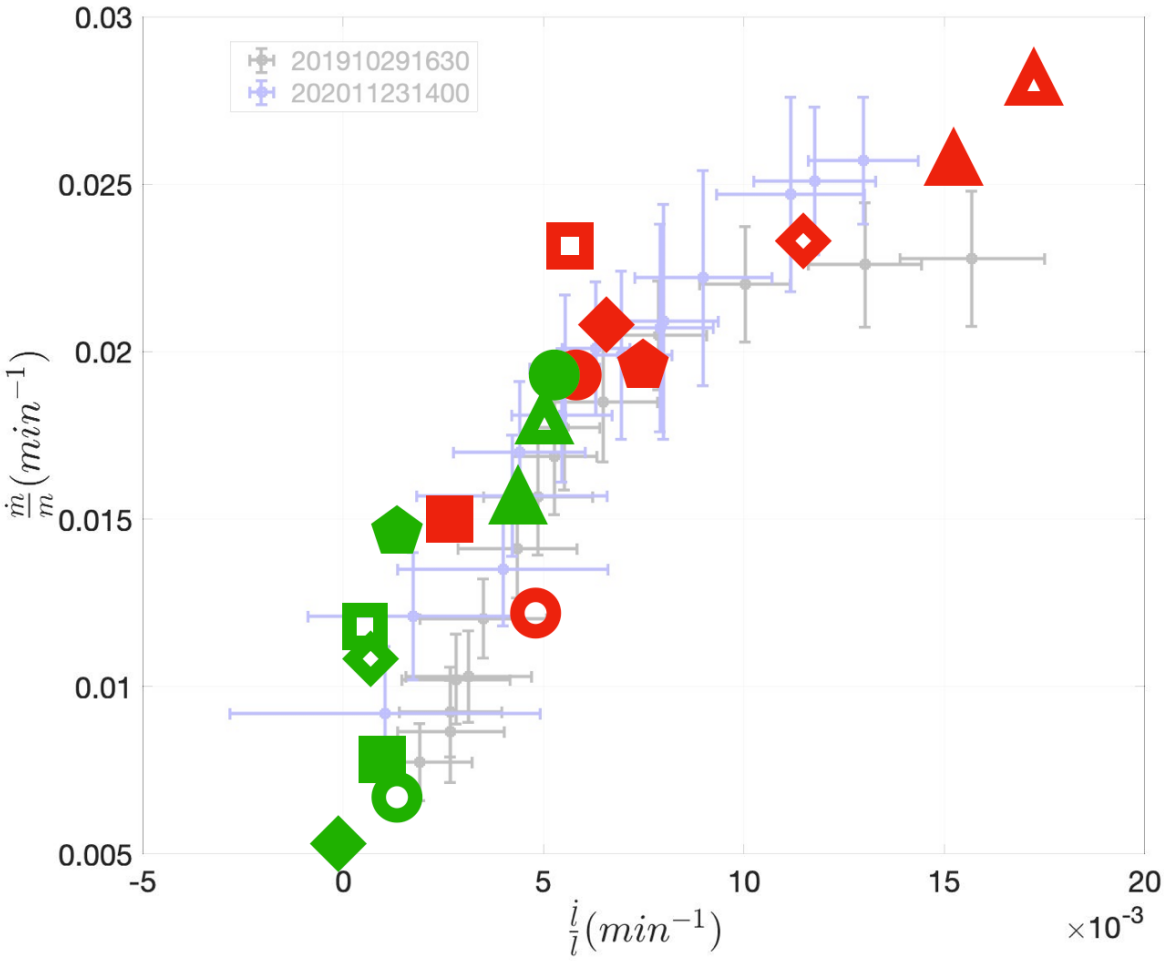

Figure 4.4: Changes in strain and myosin rates induced by optogenetic perturbations
Each data point corresponds to a particular region in which the strain rate and myosin rate were measured before (green) and after (red) activation. Different shapes represent different experiments, where the filled and open shapes represent distinct regions within the same experiment. Optogenetic data are plotted over wild type strain rate vs myosin rate curve.

4.2 Inducing strain along the A-P axis

Testing whether mechanical feedback acts independently of junction orientation necessitated a strategy which would induce strain perpendicular to the endogenous strain direction, or parallel to the A-P axis. To do so essentially requires a redirection of tissue flows in order to overcome those already present in the embryo due to the formation of the VF, which dominates the early strain profile. As a result, we designed an activation strategy in which the entire head is activated to generate a substantial flow in the A-P direction that is comparable to that induced by the VF. This ensures that the activation produces detectable strain parallel to the A-P axis.

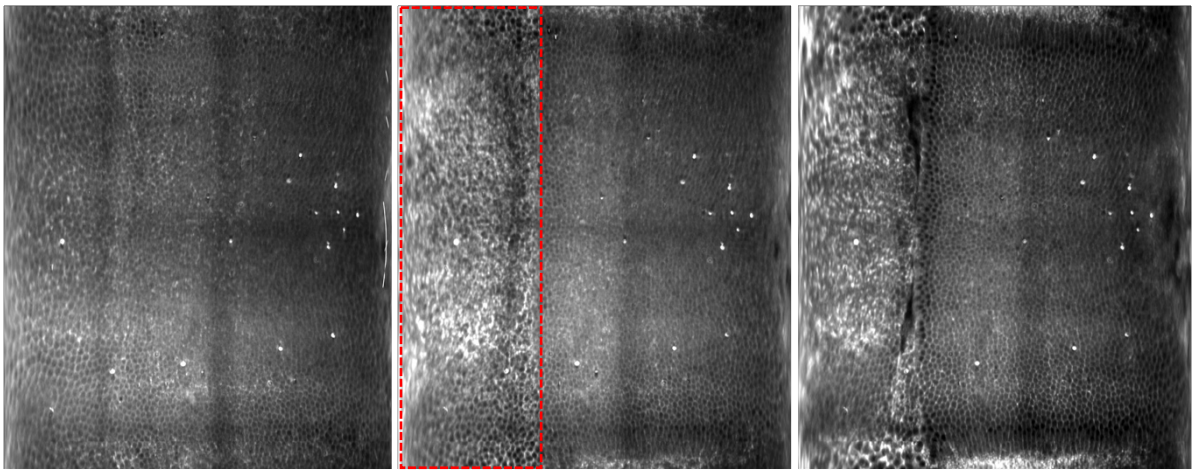

Figure 4.5: Example of raw pullbacks from optogenetic activation in head region
Pullbacks generated from 3D light sheet images of an embryo expressing the optogenetic construct and a cherry fluorescent protein tagged myosin light chain (spaghetti squash) activated in the head. Left: 1 minute prior to activation. Center: Immediately following activation. Right: 10 minutes post activation. Red dashed box shows approximate outline of activated region.

Figure 4.5 shows an example of such an activation, where the entire head region is activated, leading to contraction towards the anterior pole and subsequent stretching of the trunk region. The induction of flow is evidenced by the cell trajectories immediately following activation. Compared to wild type embryos, which have flow primarily directed toward the VF

during this stage (Figure 4.6, top left), head activated embryos show a strong anteriorly directed flow, which is essentially superimposed over the wild type flow (Figure 4.6, bottom left). This flow is further evident by a redirection of cell orientation in line with the imposed flow. Before activation, cells are primarily oriented in line with the D-V axis, as described earlier, in the direction of straining by the forming VF (Figure 4.6, top right). As a result of the anteriorly directed flow, the long axes of the cells become reoriented in the direction of the imposed strain

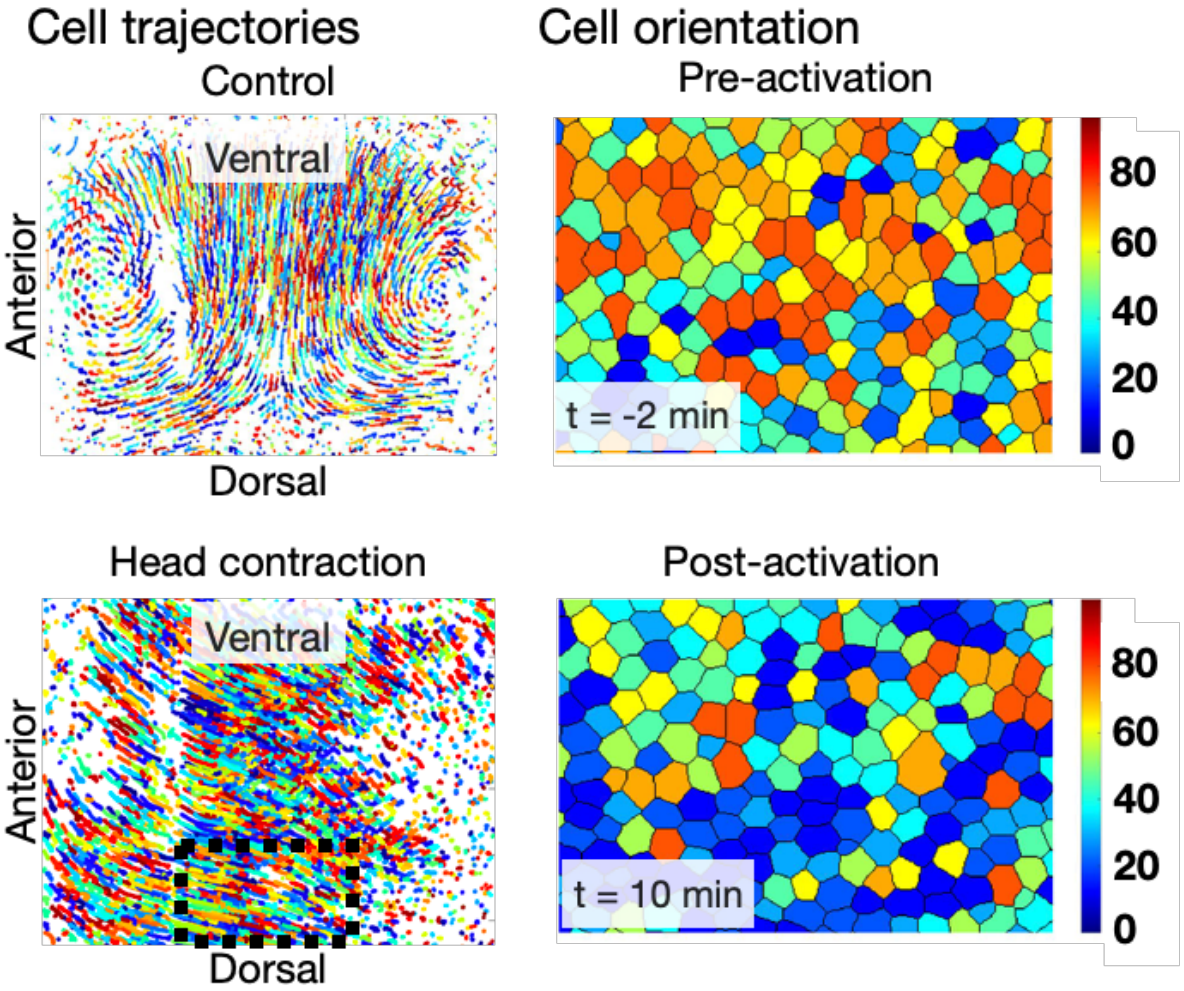

Figure 4.6: Visual confirmation of strain induced by head activation
Left: Comparison of cell trajectories in control (top) and head contracted (bottom) embryos. Images are one half of the embryo laterally (i.e. left or right side). Black dashed box in head contracted embryo shows dorsal region analyzed for cell orientation (right). Right: Heat map of cell orientation 2 minutes before (top) and 10 minutes after (bottom) activation in the region indicated by the black dashed box in the bottom left panel.

(Figure 4.6, bottom right). These measures therefore serve to confirm that the head activation strategy does result in a significant imposed strain in the direction of the A-P axis.

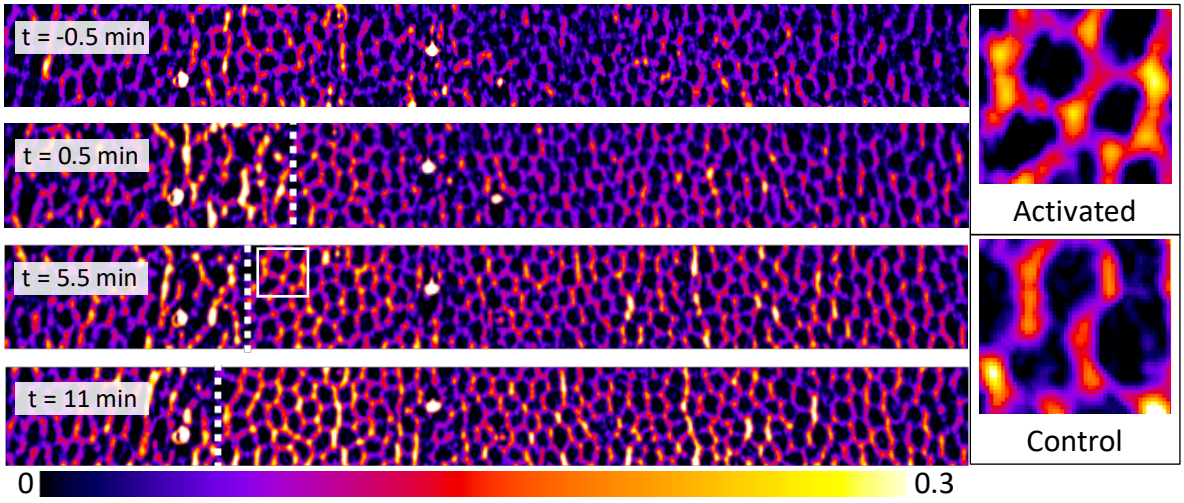

Figure 4.7: Junctional myosin accumulation over time in head activated embryo
Lateral section along A-P axis of an activated embryo. White dashed line shows boundary between activated (left) and unactivated (right) regions. White box denotes region shown in enlarged image to the right (top). Lower panel shows equivalent region in an unactivated, control embryo (bottom).

As with the previous analyses, we quantify changes in the myosin distribution by measuring the junctional myosin accumulation and associated rates in regions adjacent to the activation before and after activation (Figure 4.7). Prior to activation (t = -0.5 min), vertical junctions have begun to recruit myosin, whereas orthogonal junctions have almost no myosin, according to the establishment of the endogenous myosin distribution. Following activation (t = 0.5-11 min), there is a significant increase in myosin on all junctions: the vertical junctions continue to accumulate additional myosin as the VF forms simultaneously with the activation, and horizontal junctions begin to recruit myosin as a result of the induced strain in that direction. The result is vertical junctions with myosin levels very similar to control embryos and horizontal junctions with levels of myosin accumulation comparable to the vertical junctions and therefore much higher than the myosin accumulation to control horizontal

junctions, which is nearly absent (Figure 4.7, right). Finally, quantifying the change in junctional myosin accumulation over time following activation (Figure 4.8) shows that the activation causes a sharp increase in the levels of myosin accumulation on junctions parallel to the A-P axis compared to their pre-activation values. This quantification also indicates that there is about 2 minutes delay between the activation and the recruitment of myosin, which includes both the time between activation and contraction of activated cells (strain generation) and the time between strain generation and myosin accumulation.

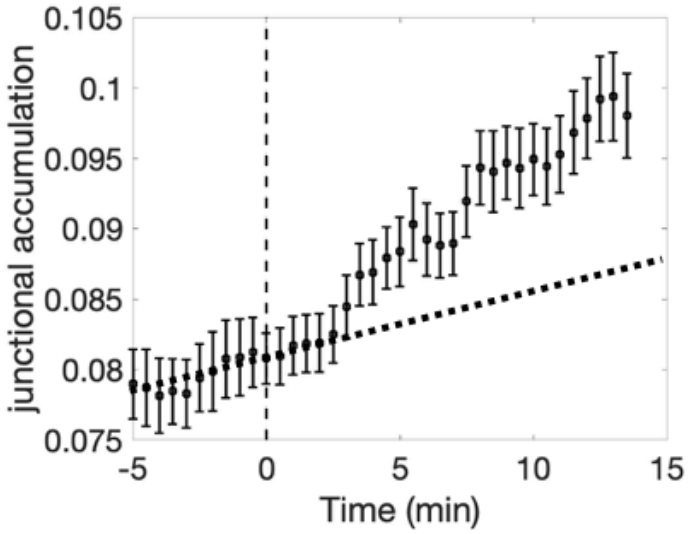

Figure 4.8: Quantification of myosin rate in head activated embryos
Junctional myosin accumulation measured on junctions parallel to the A-P axis in head activated embryos. Time = 0 (gray vertical line) shows time when activation occurs. Black dashed line shows projected myosin accumulation without activation based on the slope of pre-activation myosin rates.

Interestingly, we observe a gradient in the myosin accumulation on horizontal junctions resulting from head activation that is quantitatively similar to the gradient of myosin accumulation observed on vertical junctions during GBE (Figure 3.5). As expected, the head contraction introduces strain that decays from the source, creating a gradient of imposed strain rate that is significantly higher than controls at the activation boundaries and decreases to control levels about 250 um from the boundary (Figure 4.9). Notably, the range of strain rates as well as the distance over which the gradient is measured closely resemble those measured along the D-V axis during GBE (Figure 3.7). Taken together, these results strongly suggest that the

myosin distribution is largely set by the strain profile, wherein cells are competent to undergo a mechanical feedback response irrespective of the strain direction, but the morphogenetic processes, in this case the VF, set the primary strain direction that leads to anisotropic myosin recruitment as that observed during GBE.

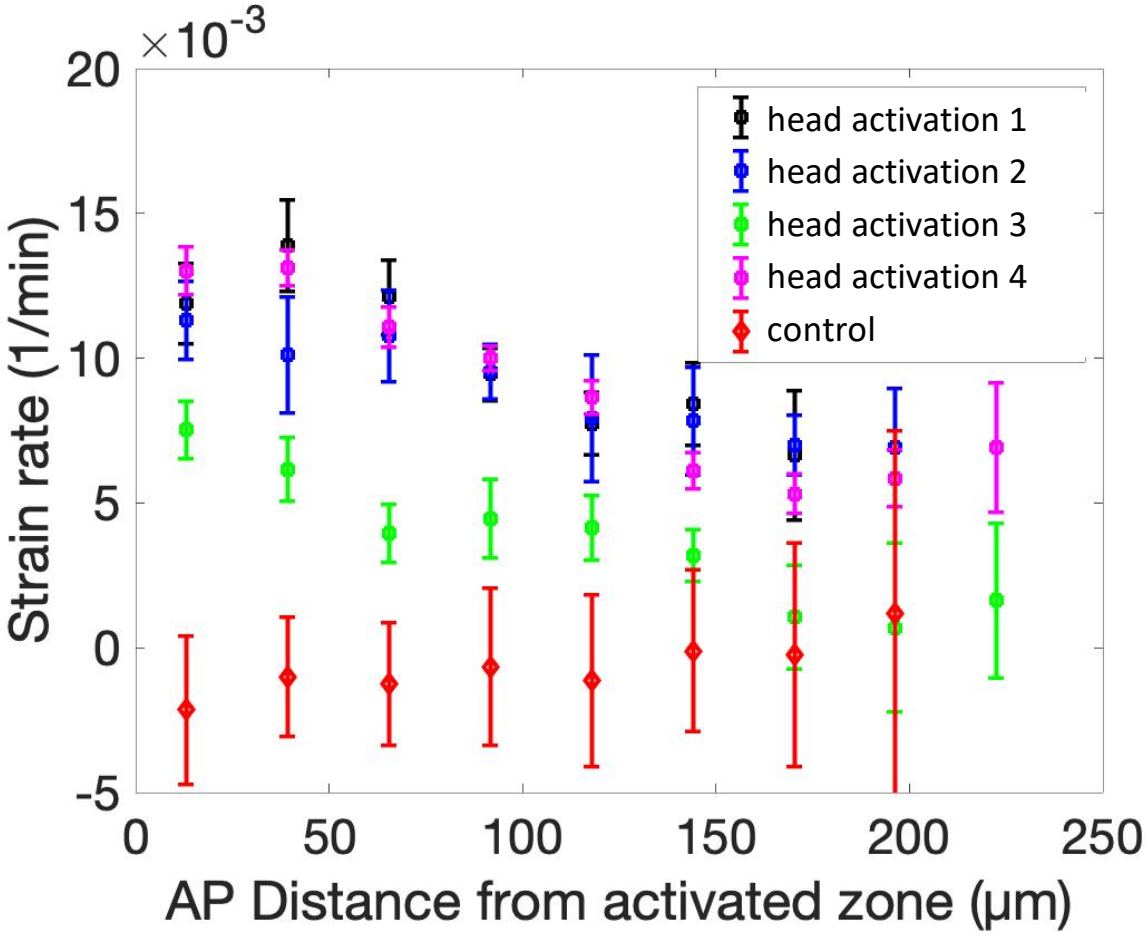

Figure 4.9: Strain rate along A-P axis as a function of distance from activation boundary
Average strain rate on junctions parallel to the A-P axis measured in discrete regions along A-P axis in head activated embryos. Distance is measured from the posterior boundary of the activated region.

The nature of the head activation strategy enabled several additional interesting observations. Considerable effort was made to achieve the near uniform activation in the entire head region, which in turn generates similar levels of pull at all positions around the circumference of the embryo. Nevertheless, the normal developmental process is largely

undisturbed by the activation such that the major morphogenetic processes, in particular VF formation, which normally determines the primary flow pattern, continue despite the redirection of flow. The result is essentially a superposition of flow fields, where the induced flow is added on top of the endogenous flow. The effects of this are clearly visible in the resulting flow field (Figure 4.10.a). On the Dorsal pole, flow is almost exclusively directed toward the head and parallel to the A-P axis. In the lateral regions however, the flow is directed both anteriorly and ventrally, resulting from the two sources of pull: the head activation and the VF, respectively. The differences in the imposed flow are clearly visible in both the cell eccentricity and orientation (Figure 4.10.b,c respectively). While cell eccentricity is somewhat

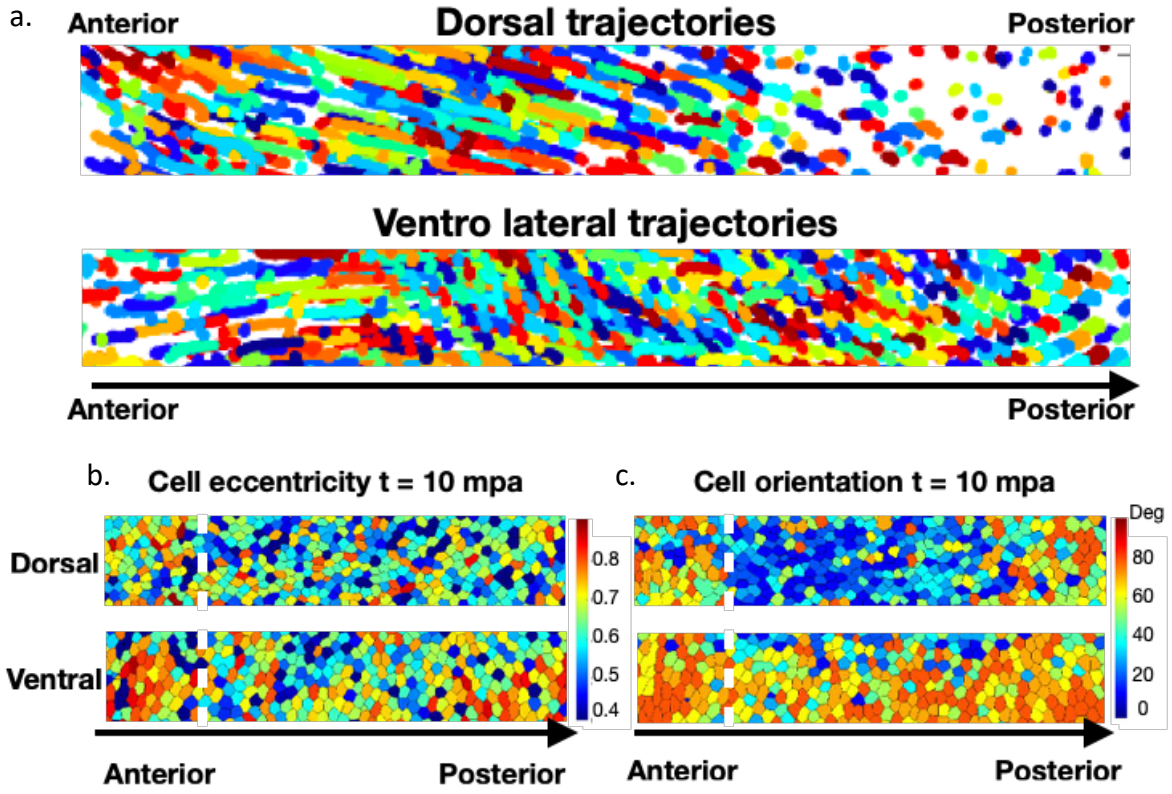

Figure 4.10: Comparison of Dorsal and Ventrolateral regions in head activated embryos

a. Cell flow in a dorsal (top) and ventrolateral (bottom) region along the A-P axis following head activation. Heat maps of cell eccentricity (b) and orientation (c) for the same regions as in (a) 10 minutes post activation (mpa). Degrees are measured relative to A-P axis. White dashed lines show activation boundary.

lower in the dorsal (top) region compared to the ventrolateral (bottom) region, cell orientation is markedly different between the two regions. The cells in the dorsal region (Figure 4.10.c, top) are aligned primarily in the direction parallel to the A-P axis, consistent with the observed flow, whereas the majority of cells in the ventrolateral region (bottom) are more aligned with the D-V axis, although at an angle considerably less than 90 degrees, consistent with the observed flow which exhibits both ventral and anterior directionality.

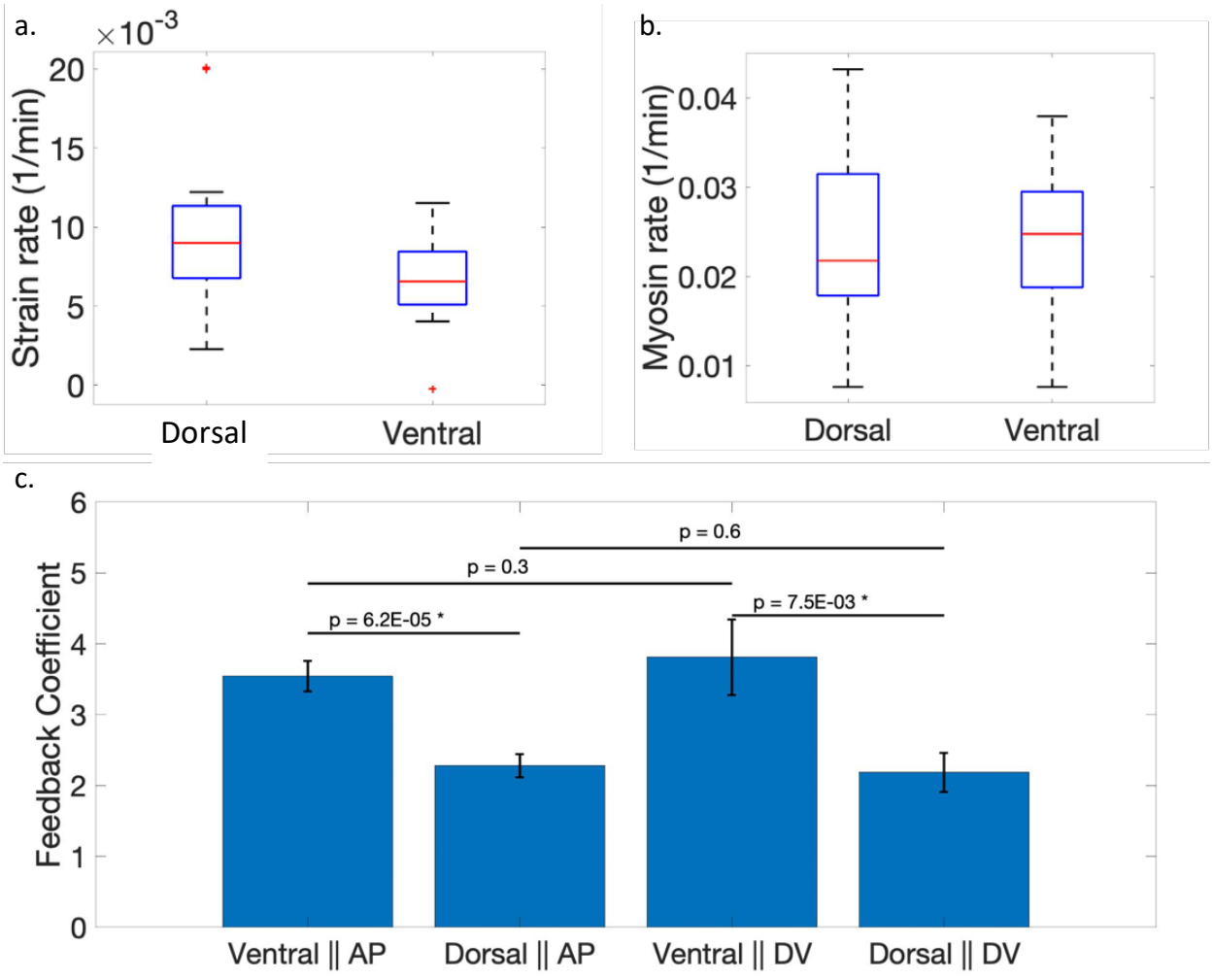

Figure 4.11: Feedback strength according to junction orientation and location
a. Average strain rate induced by head activation in the Dorsal and Ventral regions. b. Average myosin rates measured in response to the strain rates induced in (a). c. Feedback coefficient measured by junction orientation, either parallel to AP axis or DV axis, and region, Dorsal or Ventral.

As a result, the overall strain rates achieved along the D-V axis are nonuniform, and average strain rates in the dorsal regions were significantly higher than those in the ventral regions (Figure 4.11.a). However, we observed that the average measured myosin rates in these regions did not follow the pattern of strain rate, and in fact, the myosin rates were comparable despite the large difference in strain rates (Figure 4.11.b). This observation led us to ask whether the strength of feedback might vary in different contexts. To this end, we measured the relationship between the amount of myosin added to a junction and a given strain rate, i.e. the slope of the strain rate vs. myosin rate plot. Whereas Figure 3.8 pools data from all junctions within the embryo, we instead plotted myosin and strain rates based on their location within the embryo and the orientation of the junction. From each of these plots, we measured the slope of the best fit line, which gives the feedback coefficient for each of the subsets measured. Figure 4.11.c summarizes the measured feedback coefficients for junctions parallel to the A-P or D-V axis and in the Dorsal or Ventral regions. We find that the strength of feedback does not vary depending on the orientation of the junction, and therefore feedback acts isotropically within the cell, but the feedback coefficient was significantly lower for junctions of any orientation in Dorsal regions compared to Ventral regions. This surprising result has two important implications: 1) it is unlikely that the feedback mechanism is downstream of A-P patterning considering that the response is isotropic and 2) the strength of feedback may be genetically modulated by the D-V patterning system.

4.3 Unifying single junction and tissue scale dynamics

Given that the results of our optogenetic perturbations confirmed the existence of a strain based mechanism for myosin recruitment, we decided to revisit the model used to

simulate the single junction dynamics (Chapter 3, Section 5). As demonstrated in the corresponding section, incorporating mechanical feedback into the model was necessary for good agreement between experimental and theoretical results, and the optogenetic data not only validates this aspect of the model but also allows us to measure the feedback coefficient in the associated equation. We therefore asked whether we could extend the junctional model to the tissue level in order to accurately predict the myosin profile and whether adding the D-V modulation of feedback strength would change the accuracy of this prediction. Because the short time scale oscillations are averaged out over longer times, the equations governing the myosin dynamics at the time scales relevant for establishing the global myosin profile are reduced to depend only on the strain rate experienced by the tissue.

While the instantaneous myosin rate on a junction depends on the strain rate of that junction, the cumulative junctional myosin accumulation is the product of the total strain experienced by the junction over time. We therefore measure the integrated strain rate to determine the total strain experienced by the tissue during the corresponding time window and use this as the input into the model to predict the associated myosin levels. As a result, the strength of mechanical feedback is one of the few adjustable parameters in the model. Because we measured a difference in this feedback coefficient across the tissue, we further asked how incorporating the modulation of feedback strength would affect the predicted myosin levels. This is readily implemented in the model by having the value of the feedback coefficient be a function of the D-V position, in which we linearly interpolate between the ventral pole and the dorsal pole according to the pattern measured experimentally.

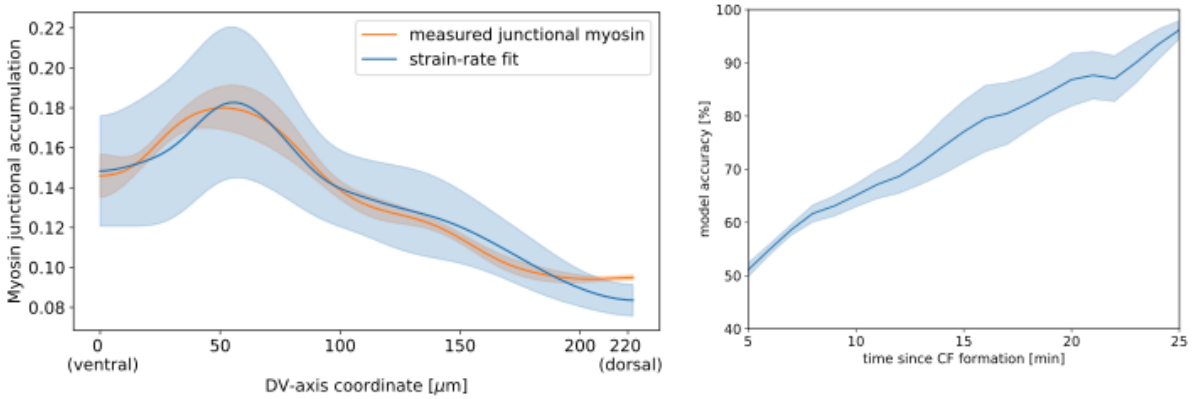

Figure 4.12: Myosin profile predicted from strain rate fit model
Comparison of myosin profile along D-V axis as predicted from strain rate (green) or as measured by junctional accumulation (red). Model accuracy (percent error calculated from fit residual and subtracted from 100) for the prediction from the strain rate integrated between 0 and the time since CF formation given by the X axis.

We compare the myosin profile across the DV axis predicted in this way to the myosin profile measured experimentally and find a surprisingly high level of agreement (Figure 4.12, right). By calculating the residual between the fit and measured curves, we obtain a measure of the model accuracy as a function of time. While the model has relatively low accuracy for early times, the accuracy of the model increases with time to over 90% during the period corresponding to GBE (Figure 4.12, left).

The fact that the myosin profile can be predicted to such levels of accuracy based only on the strain rate experienced by the tissue and without taking into consideration any A-P inputs suggests that mechanical feedback may play the dominant role in establishing the myosin profile. Taken together with the previous observations that A-P patterning mutants display defects in GBE and myosin anisotropy only in the later, slow phase of GBE, the results of our model indicate that strain-based myosin recruitment may be the primary input to establish the myosin gradient, whereas factors downstream of A-P patterning may have a more significant role in maintaining the myosin profile at later times[91].

4.4 Discussion

In this chapter, we have employed an optogenetic tool for inducing actomyosin contractility as a physiologically relevant method to introduce ectopic strain in the embryo. In this way, we have clearly demonstrated, and confirmed quantitatively, that myosin is recruited in response to increases in strain rate. We have further shown that this mechanism is able to recruit myosin in a variety of contexts in which myosin accumulation is not normally observed, such as on the dorsal pole and on horizontal junctions during early gastrulation. Generating strain in these contexts has enabled unambiguous observations of myosin recruitment as well as providing support for the generality of such a mechanism. Furthermore, the different activation strategies and contexts tested allowed us to uncover additional details about the mechanism, namely, that the feedback acts isotropically within the cell but that the strength of feedback is modulated, such that equal strain rates produce less myosin accumulation in dorsal regions compared to ventral regions. Further studies are required to confirm the possibility that this modulation of feedback strength is set by the D-V patterning system. If this is indeed the case, it would suggest that mechanical feedback is a genetically patterned mechanism to ensure robust tissue flows: the D-V gradient of myosin is essential for tissue flow from dorsal to ventral, and therefore the D-V modulation of feedback strength helps to ensure that this gradient is established. Such a possibility provides an intriguing alternative view of development in which the mechanics of the system play a much more integral role in the developmental process than previously recognized.

Interestingly, the activated embryos appear to resume normal development despite large changes in the global myosin pattern due to optogenetic recruitment of RhoGEF (Figure

4.13). Despite the strong induction of an anteriorly directed flow in the embryo, GBE continues relatively normally, as evidenced by the morphological similarity between the unactivated control embryo (Figure 4.13, left) and the head activated embryo 25 minutes after the activation (Figure 4.13, right). Although we observe drastic changes in the endogenous flow and myosin profile both within and outside of the activated region, the activated embryo looks surprisingly similar to a comparable control embryo. Notably, there are significant differences in the magnitude of the flow field, particularly in the head region, yet the pattern of flow characteristic to this time period (refer to Chapter 3 Section 1) is largely conserved after activation. Of particular note, these embryos still form the cephalic furrow even though it falls within the activated region. These findings illustrate a surprising level of robustness in the developmental program and suggest a mechanism to buffer deviations from the normal trajectory, with two important implications. First, it is reassuring that the perturbations we have introduced are not so severe as to prevent survival or even continued development. We find this point of particular importance when considering whether this measured response is relevant to the normal developmental process. As noted previously, many of the insights both into the process of GBE and a possible mechanical recruitment mechanism for myosin have relied on methods that severely disrupt the tissue and consequently normal development. It is therefore difficult if not impossible to conclude from such experiments whether the observations are relevant to the intact system and represent native processes or simply processes employed in worst case scenarios, more akin to a wound response. By employing the cell's own force generating machinery, we have avoided this issue and, in combination with our other findings, can rather confidently assert that our observations are representative of the endogenous tissue behavior that is employed under normal developmental

circumstances. Secondly, the relatively normal development after activation is strong evidence that the mechanical feedback is indeed acting as a mechanism to ensure robust morphogenetic flows. In the case of the head contraction, for example, the recruitment of myosin to horizontal edges serves to balance, and therefore mitigate, the induced anterior flow to the extent possible. It has been shown in previous work that the distribution of myosin within and between cells drives tissue flow, rather than absolute myosin levels[16]. Our results suggest that the feedback mechanism is therefore acting to restore the balance of myosin such that the developmental process may continue even in the presence of such perturbations as the head activation.

Finally, we show that the model we developed to explain the short time scale behaviors observed at the level of single junctions could be utilized to recapitulate the tissue level myosin profile on developmental timescales. Using only the total strain as an input, we accurately predict the myosin profile along the D-V axis during the time frame corresponding to the fast phase of GBE. Considering the complete absence of A-P inputs into the model, it is surprising that we achieve such high levels of predictive value. While we acknowledge that the biological situation is undoubtedly more complex than the simple model described here, our ability to recapitulate the myosin dynamics so accurately taking into account only a small number of parameters suggests that the role of mechanical feedback is likely to be much greater than previously recognized. In fact, our data strongly suggests that our current understanding of how the myosin anisotropy is established may be largely mistaken. In the next chapter, we provide additional evidence for this conclusion by utilizing mutants defective for morphogenetic processes that generate significant strain in wild type embryos to study the effects of reduced strain on the endogenous myosin profile.

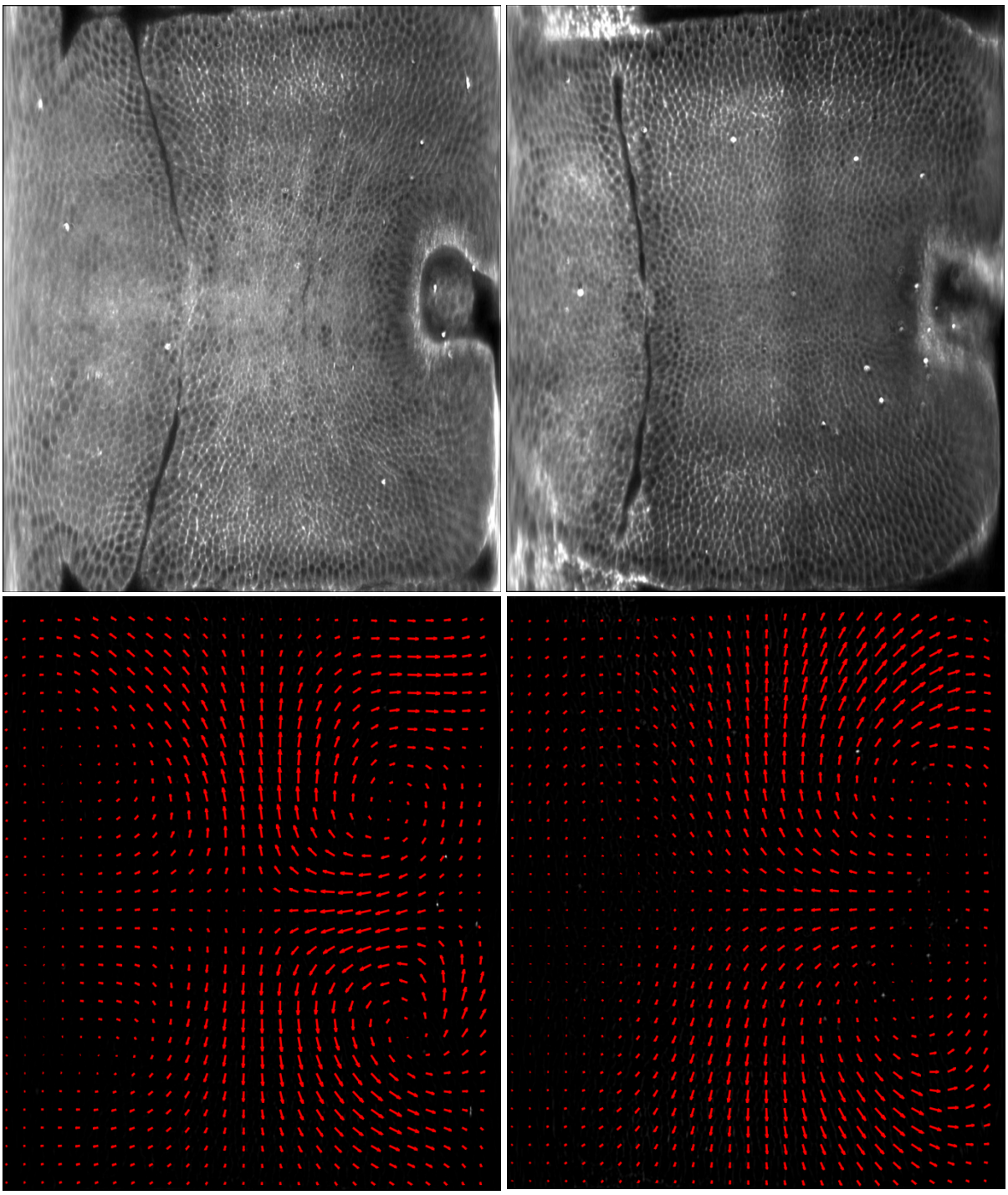

Figure 4.13: Comparison of GBE in control and head activated embryos
Top: Pullbacks of unactivated (left) and head activated (right, same as Figure 4.5) embryos 30 minutes after CF formation begins (25 minutes after activation). Bottom: Flow fields corresponding to the above pullbacks.

Chapter 5:

Effects of reducing strain using genetic mutants

Our optogenetic experiments enabled us to introduce ectopically high strain rates into the embryo to observe the effects on the myosin profile, which allowed us to clearly demonstrate increases in junctional myosin accumulation in response to increased strain. While the mechanism of inducing strain as well as the strain rates achieved through this mechanism closely mimic the endogenous situation, we next sought to determine the importance of this strain-based myosin recruitment for the normal developmental program. To do so, we decided to take advantage of the extensive genetic toolkit available in *Drosophila* and analyze mutants in which a major morphogenetic process is defective. Because strain is generated during embryogenesis, disrupting part of the process should result in changes to the strain profile, in particular, by reducing the tissue strain rates in the area affected by the mutation and its surroundings. For this work, mutants failing to form the ventral furrow were a natural choice,

as our previous analysis has demonstrated the large strain rates introduced by the formation of the VF and strongly implicated the role of these strain rates in setting the myosin profile.

As described in the introduction, Twist and Snail are two transcription factors in the D-V patterning pathway that are known to be upstream of apical myosin recruitment in the cells that form the VF. Pulsed apical actomyosin contractility has been previously reported in *twist* mutants, but failure to stabilize the contracted cell surface prevents productive decrease of cell surface area[92]. In *snail* mutants, in contrast, there are no measurable contractions of the apical cell surface. Therefore it is proposed that Twist and Snail act upstream of distinct steps of a ratchet like mechanism leading to progressive contraction of the apical cell surface: Snail activates components responsible for activating contractility of the medial myosin pool to decrease the area of the apical surface, and Twist activates components responsible for stabilization of the area change against recoil. Nevertheless, both mutations completely block the formation of the VF. Despite this defective morphogenetic process, the embryos continue developing until significantly later in embryogenesis.

Early studies of GBE reported normal axis elongation in these mutants, so it is generally accepted that D-V mutants, such as *twist* and *snail*, do not affect GBE[93]. However, this conclusion was based only on genetic analysis, without taking the mechanics into account. Recent work considering the mechanical consequences of morphogenetic movements has implied a role for the VF in GBE[73]. Furthermore, a recent study analyzing the global myosin profile noted a significant reduction in myosin anisotropy in the germ-band of *twist* mutants[16]. With no clearly established role for *twist* or D-V patterning in establishing the myosin gradient driving GBE, these surprising results warrant further examination.

This apparent discrepancy could potentially be reconciled by several plausible situations. The first is that there is some crosstalk between the two embryonic coordinate axes that has not yet been identified. Although we acknowledge this as a possibility, we consider it rather unlikely that the extensive and rigorous genetic screens undertaken in the early embryo and the later targeted characterization of the A-P and D-V patterning systems did not reveal such a connection. The second possibility is that *twist* and/or *snail* have previously undetected effects outside of their immediate expression domains. Previous work has identified a sharp expression domain for both transcription factors limited to the cells that will form the presumptive mesoderm[94], but their downstream targets could have farther reaching effects. For example, twist is a transcription factor upstream of the secreted ligand fog[95]. This scenario relies on the premise that the diffusion of the secreted fog ligand leads to activation of receptors in the germ-band that consequently leads to myosin accumulation on vertical junctions, contributing to the myosin anisotropy driving GBE. While the diffusion of a secreted ligand could possibly lead to the observed D-V gradient of junctional myosin, there are a number of other issues that arise with this hypothesis. First and foremost, the known receptor for fog has not been detected in the germ-band[96], although fog binding could be promiscuous and therefore bind previously unidentified receptors. How these interactions would lead specifically to an anisotropic myosin localization, however, is difficult to conceptualize. Finally, more recent work has shown that while there is space between the vitelline membrane and the embryo surface in early stages to allow appreciable diffusion, the embryo surface becomes closely apposed to the vitelline membrane following cellularization[89]. This severely limits the capacity for free diffusion of particles, and on the time scale separating *twist* and *snail* transcription and establishment of the myosin anisotropy, attaining significant levels of Fog ligand in the region

of the germ-band seems implausible. Additionally, Snail is upstream of a membrane bound protein Mist, which is the receptor for the Fog ligand[97], and is therefore unable to effect cells in which it is not directly expressed. This allows an opportunity to readily test this possibility: if Fog is secreted and diffuses to affect cells in the germ-band, then mutants for *twist* and *snail* should have significantly different effects on the myosin distribution. In particular, *twist* mutants should exhibit the observed decrease in myosin anisotropy, whereas *snail* mutants should not show measurable differences from the wild type distribution.

The final possibility, as discussed earlier, is that the tissue deformation downstream of Twist and Snail, rather than specific aspects of the genetic pathway, is the important factor to influence the myosin distribution in the germ-band. In this scenario, the invaginating VF causes stretching of the adjacent tissues, namely the germ-band, and the resulting strain recruits myosin to the junctions in the direction of strain[16]. This possibility accounts for several of the observations, thus making it favorable over the others. First, the VF generates strain on edges perpendicular to the furrow, i.e. edges parallel to the A-P axis or vertical junctions. If only strained edges recruit myosin, then the VF intrinsically establishes myosin anisotropy in the direction observed. Secondly, strain will decay with distance from the source, the VF, due to dampening by frictional forces[89]. Strain based recruitment by the formation of the VF would, therefore, also be consistent with the observed gradient in junctional myosin accumulation observed along the D-V axis of wild type embryos. Furthermore, if this is the case, then the *twist* and *snail* mutants should have very similar changes in the myosin anisotropy compared to the wild type profile. We therefore analyze both *twist* and *snail* mutant embryos and measure the strain rates and myosin rates in these mutant backgrounds. Finally, we measure the rate of GBE compared to wild type siblings as an indication of the effects of the mutation on the

normal course of development, aside from its known role in preventing VF formation and later mesoderm development.

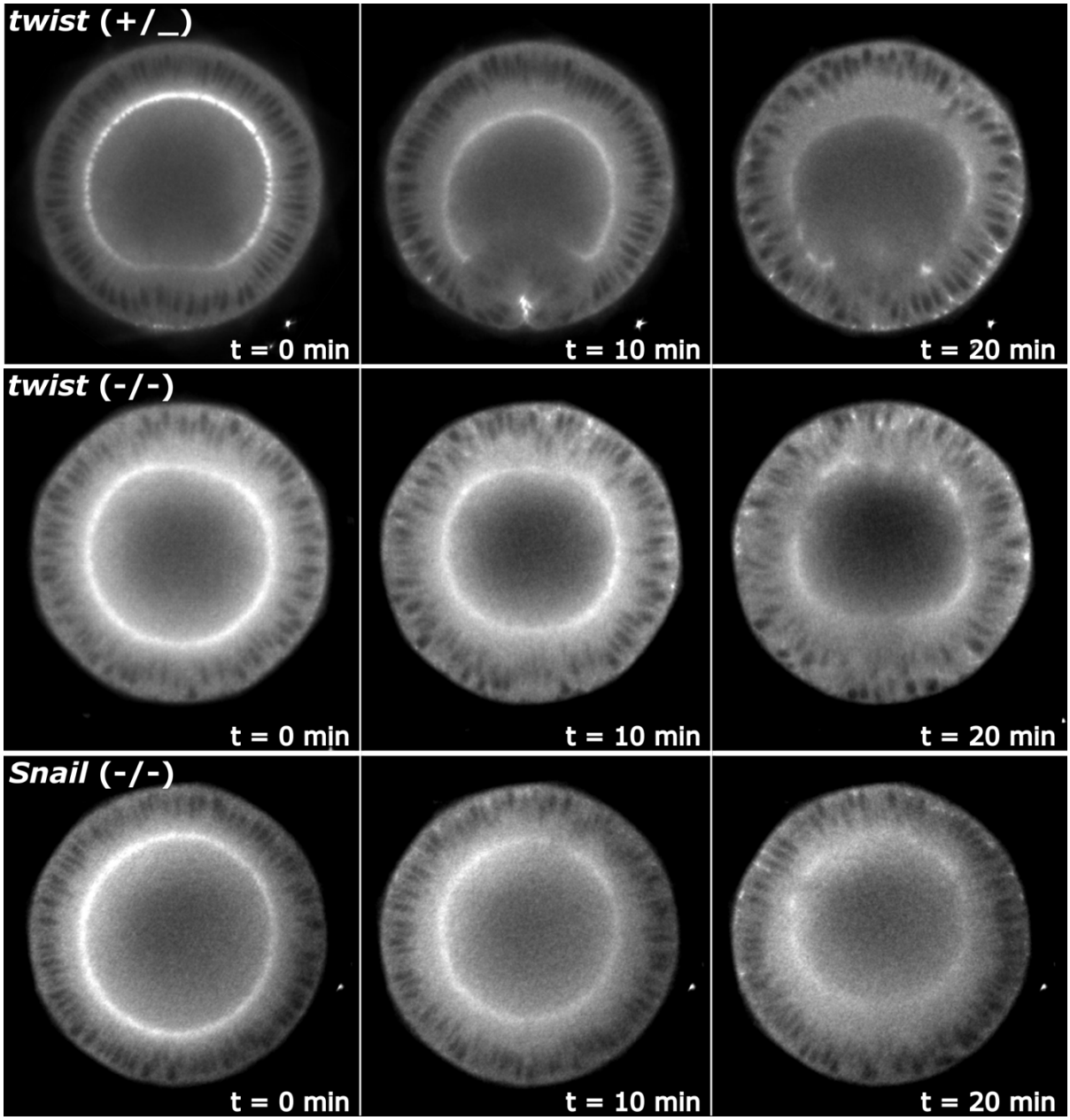

Figure 5.1: Cross sections through WT and mutant embryos during VF formation
Each image is a single cross section through approximately the center of the A-P axis. Dorsal is top and Ventral is bottom. Time stamps are given relative to CF formation. Top: Wild type siblings of *twist* mutant embryos showing normal VF formation. Center: *twist* mutant embryos which fail to demonstrate any signs of normal VF formation. Bottom: *snail* mutants which show phenotype that is nearly indistinguishable from *twist* mutants.

5.1 VF in completely absent in *twist* and *snail* mutants

As expected, both *twist* and *snail* embryos completely fail to show any indication of a VF forming[63], at least at the level of our acquisition. Previous observations that apical constriction without stabilization occurs in *twist* mutants were made at higher spatiotemporal resolution[92], and therefore they may be present in our *twist* mutants but undetectable at the scales we observe. Furthermore, these mutant embryos continue to undergo other morphogenetic processes, albeit slower in the case of GBE as we will demonstrate later, indicating that the failure to form the VF is a specific phenotype and not merely embryos that fail to develop at all. The phenotype is clearly visible in a cross-section of the embryo through the approximate center of it's A-P axis (Figure 5.1). While wild type siblings of mutant embryos show the normal progression: loss of basal myosin followed by apical recruitment in the ventral region, tissue bending due to apical constriction, and finally tissue invagination and furrow fusion, the *twist* and *snail* embryos of equivalent stages show no sign of these processes. In fact, both the basal and apical myosin pools remain uniform during early gastrulation, as seen in Figure 5.1. Given this qualitative absence of the morphogenetic process driving tissue deformation during this stage, we next quantitatively characterized the phenotype by measuring tissue strain rates.

5.2 Tissue strain rates are strongly reduced in VF mutants

The strain profile measured in the wild type embryo indicates that the formation of the VF is the dominant source of strain generation in the early embryo (Figure 3.3). Accordingly, we expect that a mutant failing to form the VF will have a significantly reduced strain profile in these early stages. To confirm this, we measure the strain rates in the embryo along the D-V axis, as with the wildtype embryos characterized in Chapter 3 Section 2.3.

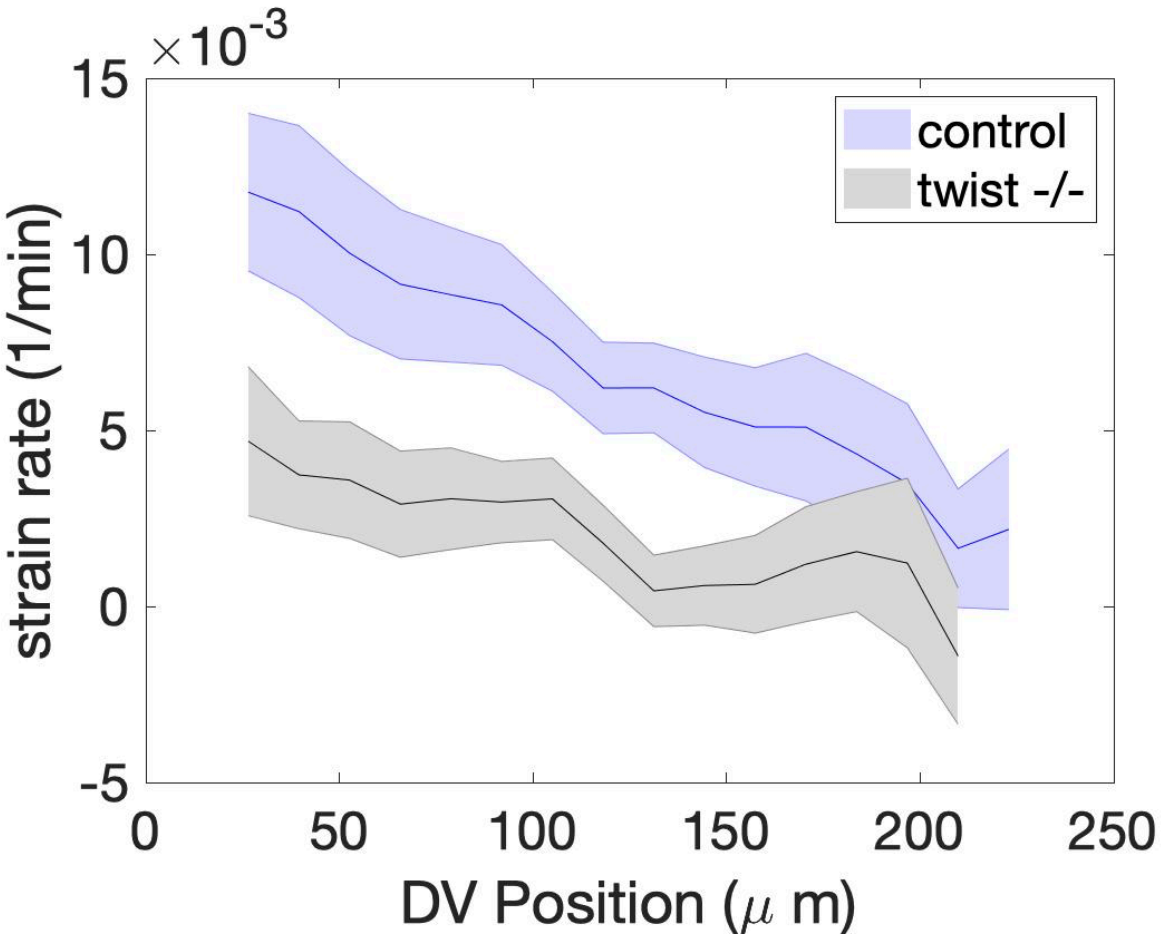

Figure 5.2: Strain rate across D-V axis in wild type and mutant embryos
Strain rate along D-V axis, as measured in Figure 3.4, in wild type siblings (*twist*(+/_), "control") and *twist* mutant embryos (*twist*(-/-)).

Wild type siblings of *twist* and *snail* mutants (*twist* (+/_) and *snail*(+/_), respectively) show the same rates and D-V gradient as the wild type embryos characterized earlier (Figure 5.2, blue, compare to Figure 3.4). In striking contrast, both *twist* and *snail* mutant embryos exhibit strongly reduced strain rates, which we measure to be approximately half of the wild type rates for all positions along the D-V axis (Figure 5.2, gray, Figure 5.5). We therefore conclude that the VF generates much of the strain in the early embryo and that mutants failing to form the VF consequently have greatly reduced strain rates in the period corresponding to

early gastrulation. As a result, we are able to take advantage of these mutants as a method to reduce the endogenous strain profile and measure the effects on the myosin profile.

5.3 Characterization of myosin rates in *twist* and *snail* embryos

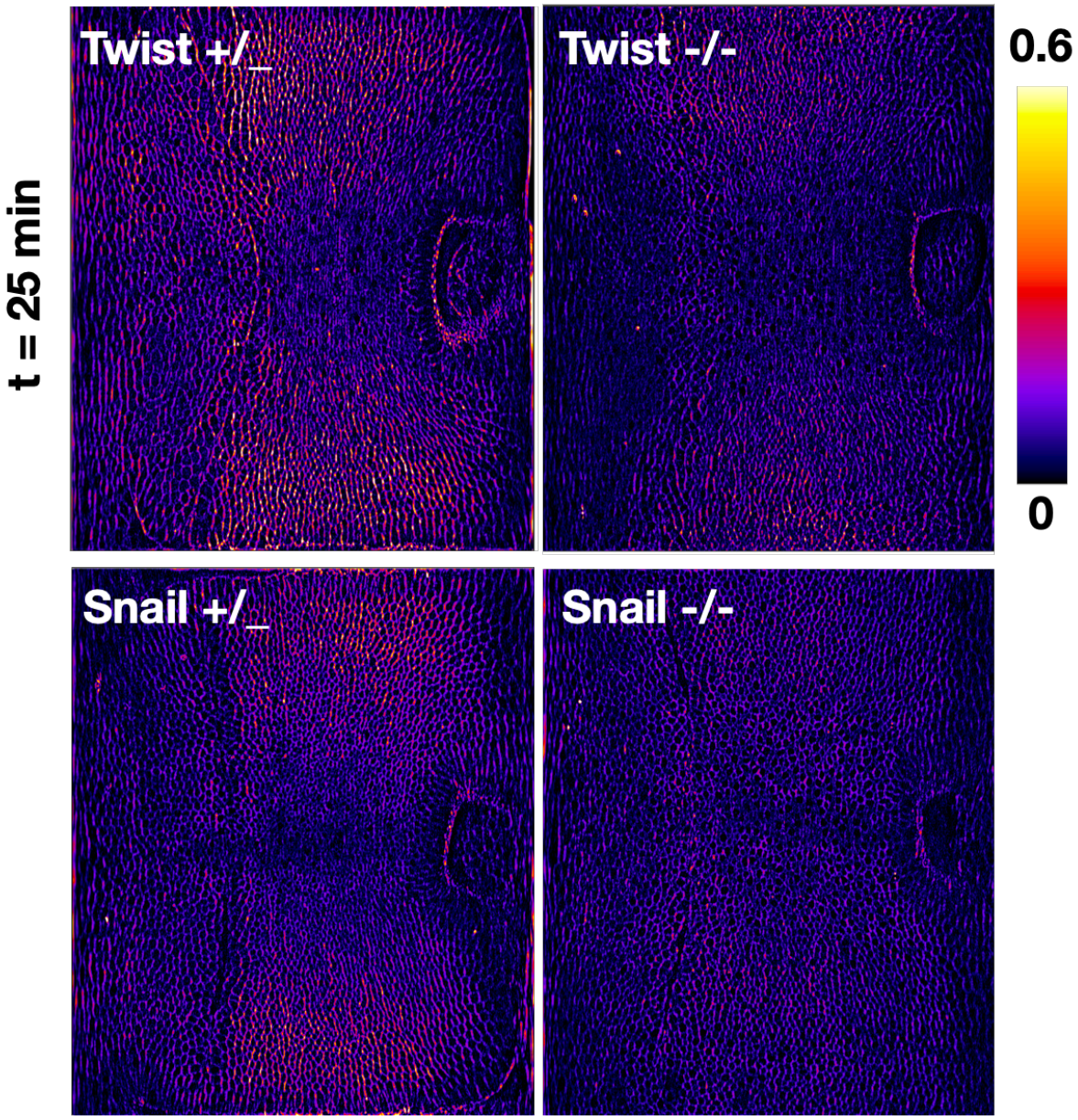

Figure 5.3: Junctional myosin accumulation in WT and VF mutants during GBE
Heat map of junctional myosin accumulation in comparable time points of *twist* (+/_) and *twist* (-/-) (top) and *snail* (+/_) and *snail* (-/-) (bottom) embryos.

We next characterize the myosin profile in these mutants as before, using the junctional myosin accumulation. From the heat map of junctional myosin accumulation in wild type embryos (Figure 5.3, left) compared to *twist* and *snail* mutant embryos (Figure 5.3, right), it is immediately apparent that the mutant embryos have substantially less junctional myosin. Indeed, the quantification of myosin rate across the D-V axis shows an approximately two-fold reduction in myosin rates between wild type and *twist* mutant embryos (Figure 5.4). Notably, the fold reduction in myosin rates is very similar to that in the strain rate. Therefore, like in the optogenetic experiments where an increase in strain rate induces a proportional increase in myosin rate, a reduction of strain rate leads to a proportional reduction in myosin

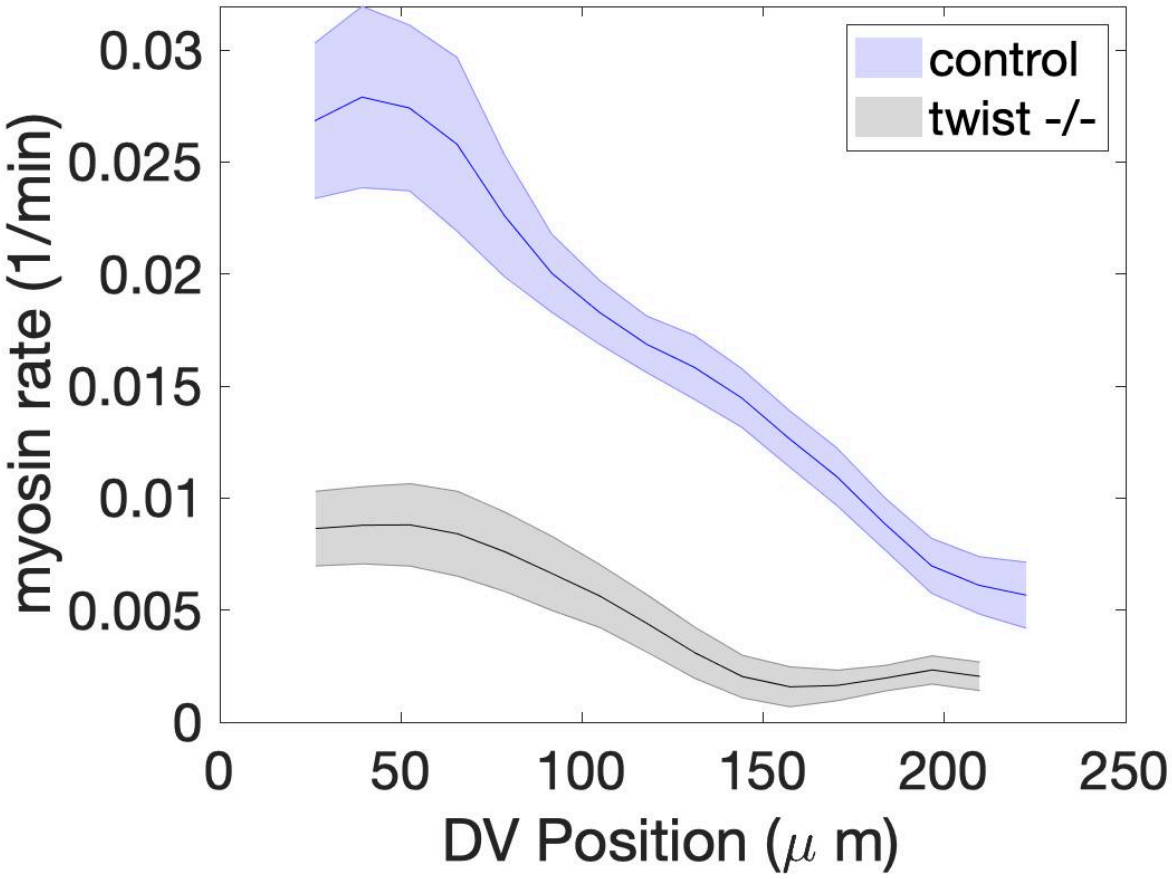

Figure 5.4: Myosin rate across D-V axis in wild type and mutant embryos
Myosin rate along D-V axis, as measured in Figure 3.7, in wild type siblings (*twist*(+/_), "control") and *twist* mutant embryos (*twist*(-/-)).

rate. This is further apparent by plotting the myosin rates vs. strain rates in *twist* and *snail* mutant embryos over the wild type curve (Figure 5.5). The data points fall at lower regions of the plot on both axes, consistent with significant reductions in both strain and myosin rates, but on approximately the same line that represents the relationship between strain rate and myosin rate in wild type embryos (Figure 5.5). This further indicates that neither *twist* nor *snail* mutations effect the strength of mechanical feedback. Our results examining the feedback coefficient suggest that D-V patterning may be upstream of the strength of feedback. However, the retained proportionality in the *twist* and *snail* mutants indicates that the strength of feedback is likely downstream of a patterning element other than *twist* or *snail*.

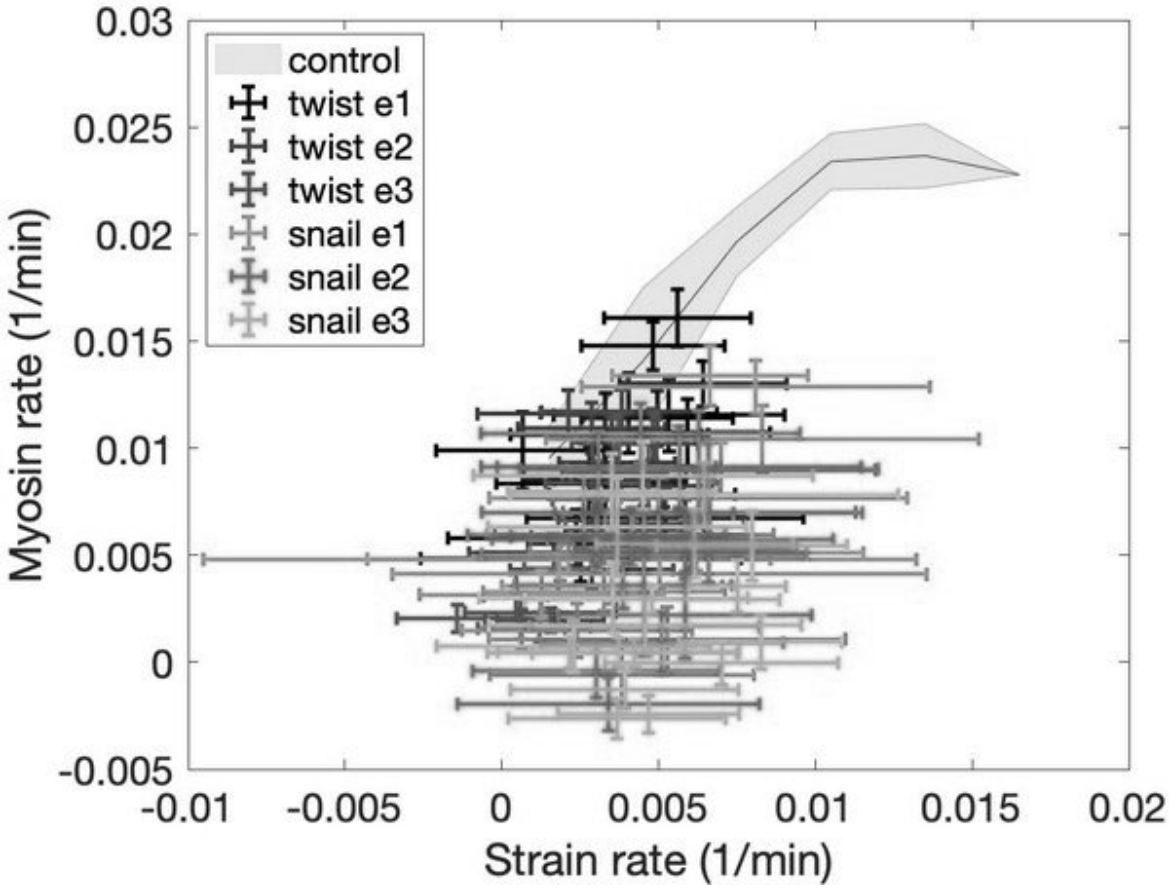

Figure 5.5: Strain rate vs myosin rate plot of *twist* and *snail* mutants
Myosin rates plotted as a function of strain rate for *twist (-/-)* and *snail(-/-)* mutant embryos plotted over the ensemble average WT curve.

5.4 Reduction in myosin profile has significant effect on rate of GBE

Having shown the reduction in strain rate due to the absence of the VF in *twist* mutants and the subsequent reduction in junctional myosin in the germ-band, we next asked whether this reduction in junctional myosin, which is associated with driving GBE, had measurable effects on the process of GBE. The distribution of myosin is known to drive flow[16], so we reasoned that the significant changes in the myosin profile observed would have measurable consequences to the resulting tissue flow. Although previous works have not reported such a defect in GBE in *twist* mutants, we note that many of the methods used previously to determine tissue extension during GBE may not have been sensitive enough to capture the change. Therefore, we reexamine the process of GBE in these mutants making use of our imaging techniques and highly sensitive myosin metric. By imaging the entire embryo in 3D, we are

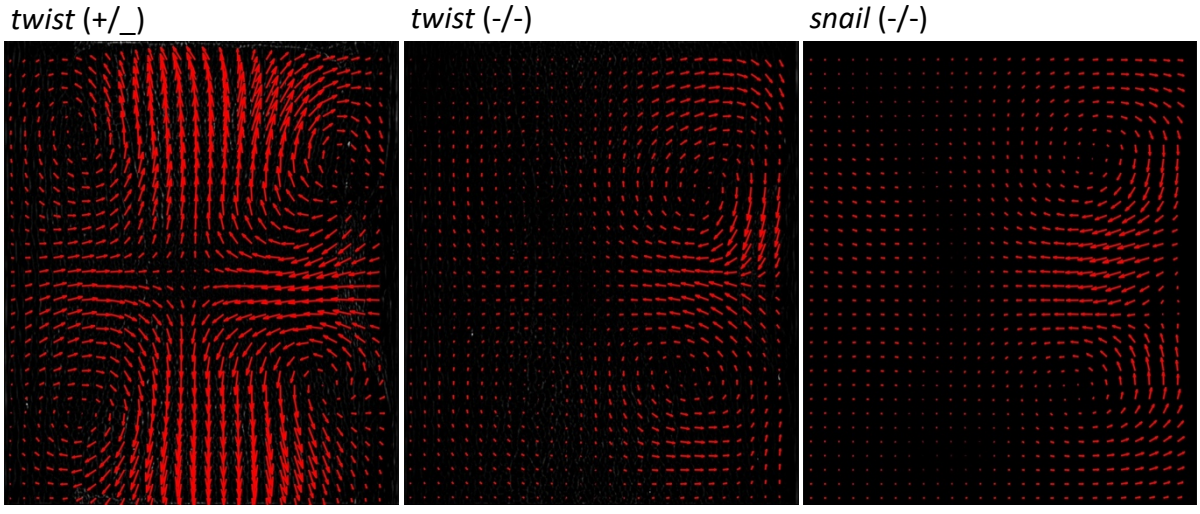

Figure 5.6: Flow fields for wild type and mutant embryos during period of ventral furrow formation
Flow fields calculated from time points corresponding to 10 minutes post CF formation (center timepoint in Figure 5.1) Left: Wild type sibling of *twist* mutant embryos. Center: *twist* mutant. Right: *snail* mutant.

able to more accurately measure the rate of GBE using PIV[98] across the embryo surface to enable a quantitative examination of the global flow.

This is evident from the flow fields during the time period during which the VF forms in wild type embryos (Figure 5.6). As described previously, the formation of the VF and the subsequent invagination of cells into the furrow, generates a strong flow towards the ventral midline that dominates the flow field during this stage. This flow pattern is further characterized by the resulting vortices. *Twist* and *snail* mutants, in contrast, have very little flow towards the ventral midline, leading to a global reduction in the total magnitude of the

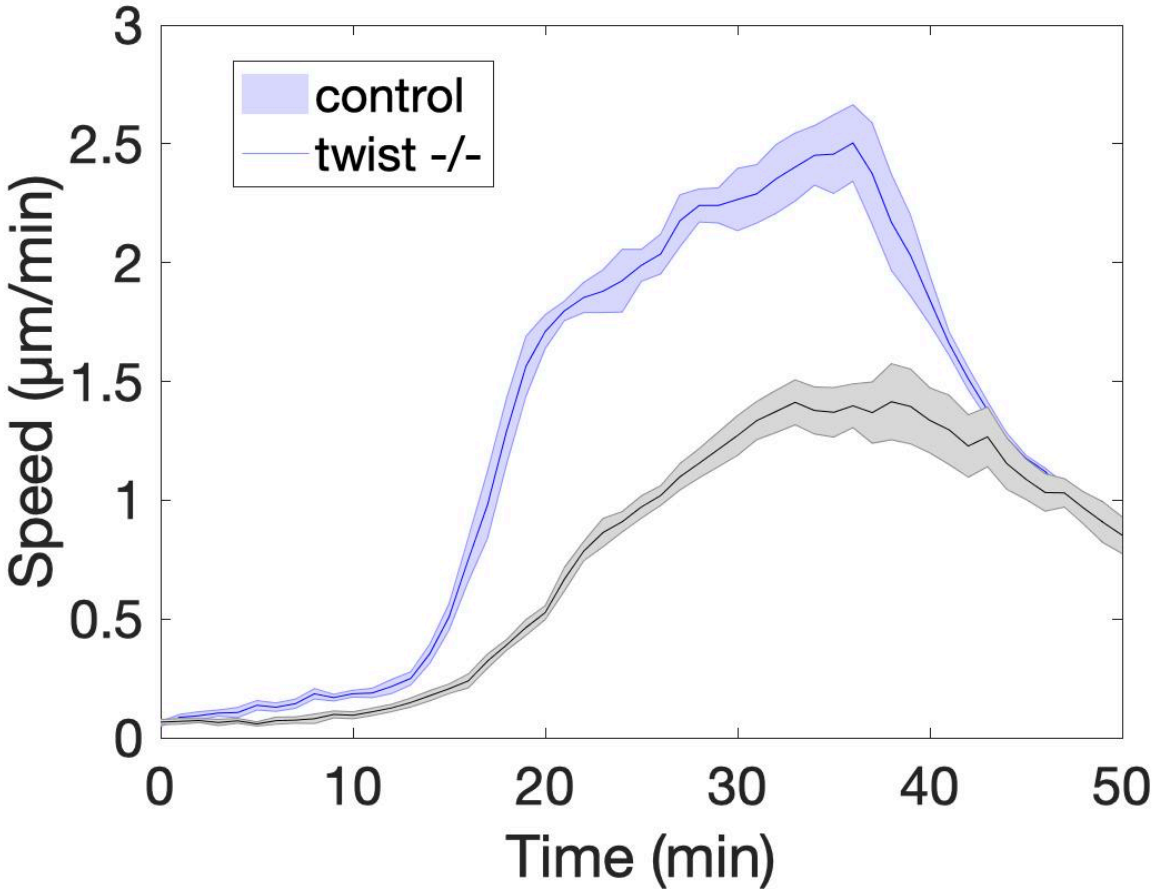

Figure 5.7: Rate of GBE in wild type and *twist* mutant embryos
Ensemble averaged rate of tissue flow measured from PIV of wild type siblings ('control', *twist* (+/_), n = 5) and *twist* (*twist* (-/-), n = 5) embryos from initiation of cephalic furrow formation (t = 0) through the fast phase of GBE (ends at t ~35 min).

flow. The primary features of the flow are nevertheless conserved, including the directions of flow and the resulting vortices. We then quantify this affect by measuring the flow for all timepoints from the end of cellularization through the fast phase of GBE and measure the average speed of tissue flow. In this way, we determine that the rate of GBE is approximately 2-fold reduced in *twist* mutants compared to wild type siblings (Figure 5.7). These results therefore demonstrate that the major flow pattern, with the exception of that directly resulting from the invagination of cells into the VF, is maintained in VF mutants, but the magnitude of the flow is globally reduced in the absence of the VF.

5.5 Discussion

Although early works examining GBE reported normal extension in *twist* and *snail* mutants[93], this was assessed only by measuring the final length of the germ-band at the completion of GBE. However, our results indicate that the absence of the VF reduces the kinetics of GBE, i.e. that GBE occurs at reduced rates. Although it is consistent with the previous findings that the total amount of extension is unchanged in these mutants, these mutants require a significantly longer time window to complete GBE. Therefore, in terms of dynamics, they cannot be said to elongate normally. As we have shown by the intricate dependence of myosin rate on strain rate, the dynamics of the system are an important factor, which modern techniques have enabled us to take into consideration. With these advancements in imaging and analysis, we have demonstrated that the VF generates substantial strain rates in the germ-band as it forms, and consequently, its absence is marked by greatly reduced strain rates in the germ-band. This is consistent with previous findings that measured the strain rate in the embryo during GBE and found them to be reduced in *twist* mutants. We next showed that the myosin

profile is similarly reduced in these mutants, again corroborating previous observations. Our results therefore bridge the previous findings with our hypothesis of a mechanical feedback mechanism for myosin recruitment, which is supported by our optogenetic perturbations. Taken together, our results demonstrate that strain-based myosin recruitment activated by the pull from the VF makes a significant contribution to the myosin profile driving tissue elongation during GBE. This is further evidenced by the reduced rates of tissue flow during GBE in *twist* and *snail* mutants.

Chapter 6:

Conclusions and outlook

In this final chapter, we briefly summarize the main results from the earlier chapters and their significance for our current understanding of *Drosophila* GBE. We then contextualize our new results within the framework established by the previously published literature and discuss remaining gaps in the model. Next we suggest further experiments and detail the possible outcomes and their interpretations with the goal of addressing these open questions. Finally, we contemplate implications for other systems as well as for development as a whole.

6.1 Summary of key results

In this work, we have used global imaging techniques in combination with highly quantitative analysis to characterize the dynamics of strain and myosin during *Drosophila* VF formation and fast phase GBE. Using Mu-Vi SPIM and tissue cartography, we captured whole embryo

images of the myosin distribution and utilized novel analysis techniques to measure the deformation across space and time in the developing embryo as well as the myosin distribution characterized by a metric we designate as the junctional myosin accumulation. In this way, we show that the rate of strain and the rate of myosin accumulation are graded across the D-V axis of the embryo. Additionally, these two values are strongly correlated across the entire embryo. We utilized optogenetically patterned ectopic strain rates to show causality between increases in strain rate and increases in myosin rate. We further showed that this causality is independent of spatial or directional information, although we demonstrate a dependence of feedback strength on D-V position. We next zoomed in to the level of single junctions using confocal microscopy to examine the behavior of strain and myosin at faster time and shorter length scales, allowing us to ask how the myosin on a single junction responds to the strain on that same junction. Correlation analysis showed that strain rate and myosin rate oscillate with a period of about 74 seconds with a phase shift between curves of approximately half a period. These dynamics further showed that a peak in strain rate was followed by an elongated period of positive myosin rate. We adapted a concentration oscillator model to incorporate mechanical feedback and were able to accurately recapitulate our experimental results, both at the single junction and tissue level. Finally, we demonstrated that a reduction in endogenous strain rates, such as that resulting from the loss of the VF, leads to a proportional reduction in the myosin rate with measurable consequences for the rate of GBE. These results therefore represent, to the best of our knowledge, the first documented example of a causal mechanism for strain based myosin recruitment and its relevance to normal development.

6.2 Reconciling results with previous findings and open questions

An intriguing possibility supported by our work reconciles the current discrepancy in the model for GBE uniting isotropic distributions of TLRs with the downstream anisotropy of myosin. As discussed in the introduction, the previously accepted model for myosin anisotropy relies on partially overlapping stripes of different TLR expression patterns, with the receptors expressed isotropically within cells in their expression domain. However, the mechanism linking these distributions to myosin anisotropy is currently unknown. One possibility, therefore, is that TLRs do not confer myosin anisotropy directly, but rather determine a cell's

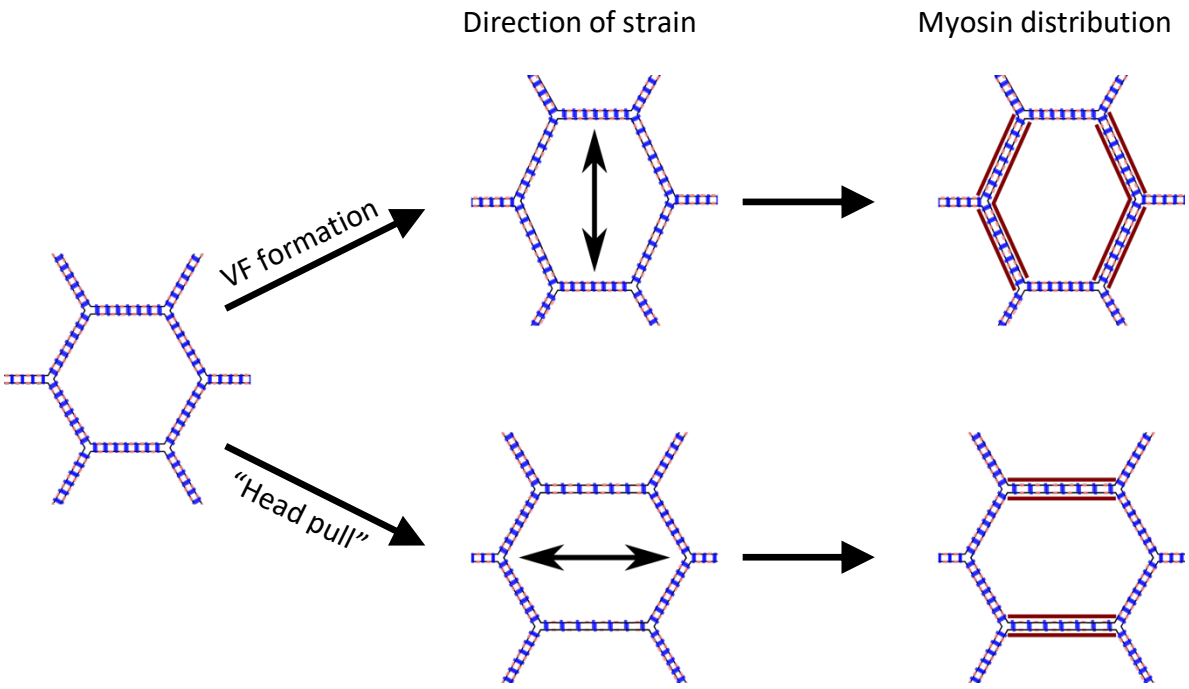

Figure 6.1: Model for establishing anisotropic myosin distribution from isotropic distribution of upstream pathway components using strain direction as an input
Cell uniformly expressing a component of the mechanical feedback mechanism, for example TLRs, is stretched during tissue morphogenesis. In the top example, the VF induces strain in the vertical (D-V) direction, and the cell is stretched accordingly. This leads to the anisotropic myosin pattern observed in GBE, with myosin enriched on vertical (stretched) edges. In the bottom example, as seen with the optogenetic head pulling experiments, strain is induced in the horizontal (A-P) direction. The resulting cell stretching recruits myosin on the horizontal edges, as observed in experiments.

competence for mechanical feedback. In this scenario, isotropically distributed TLRs are activated by the pull from the VF to promote myosin recruitment on stretched edges (Figure 6.1, top row). During normal development, this leads to the observed myosin distribution driving GBE. In other cases, such as the ectopic strain generation in optogenetically activated embryos, the direction of strain is now orthogonal to that in the endogenous situation. Nevertheless, because TLRs are present in all cell edges, the cell is competent to respond to strain in this direction also, which is how myosin accumulation is observed on stretched edges also in the optogenetic experiments like the head activation.

A second possibility is that TLRs are required to set the strength of feedback. As we showed with the optogenetic perturbations, the feedback coefficient, representing the strength of mechanical feedback, is modulated along the DV axis. While it is possible that one of the D-V patterning elements sets this parameter, our results from *twist* and *snail* indicate that the feedback coefficient is preserved in these mutants. Interestingly, recent work has described the gradient in PRG and TLR stripes along the D-V axis and further showed that their predictive model using the TLR patterns recapitulates the D-V but not the A-P gradient of myosin[91]. Although it is still unknown what factors are responsible for the gradation of PRG and TLR stripes along the D-V axis, as they are strictly characterized as A-P dependent, the observed similarity suggests a novel mechanism by which TLRs impact the myosin distribution during GBE.

Thirdly, it is possible that the myosin anisotropy attributed to TLRs is independent of that due to mechanical feedback. In *twist* and *snail* mutants, some residual junctional myosin is observed, indicating that a portion of the myosin distribution may not be attributable to mechanical feedback. In this scenario, A-P patterning through the PRGs and TLRs is

responsible for the portion of the myosin anisotropy maintained in VF mutants, and mechanical feedback contributes the remainder.

Finally, the residual myosin profile in *twist* and *snail* mutants could be attributed to the hoop stress in the embryo due to its geometry[91]. The embryo is under turgor pressure, which must be balance by the surface tension for the embryo to remain intact. Because the characteristic shape of the embryo is much longer along the A-P axis than the width along the D-V axis, the stress is higher along this axis. As a result, mechanical feedback activated by the hoop stress would lead to myosin recruitment parallel to the D-V axis, and the modulation of feedback strength along the same axis would produce the observed gradient of myosin accumulation from the uniform input. This possibility implies that mechanical feedback is the only mechanism for establishing the myosin distribution. Although it may initially seem to contradict previous results for the dependence on A-P patterning, a number of scenarios could remedy this apparent discrepancy. Firstly, A-P patterning, and specifically TLRs, could mediate mechanical feedback as suggested previously, either in strain sensing or in the process mediating strain sensing and myosin recruitment. Alternatively, as we have also suggested already, TLRs could be responsible for the strength of feedback. There are therefore a number of possibilities to reconcile the previous literature with our results, and while some are mutually exclusive, others can be acting in combination.

There are several key experiments that can be carried out to eliminate or support each of these possibilities. One of the first steps would be to rigorously analyze TLR mutants during VF formation and the fast phase of GBE. Previous work demonstrating a role for TLRs in the anisotropic myosin distribution relied on analysis of a relatively small number of cells at a timepoint well into GBE. Therefore, a more complete view of the TLRs role for myosin

anisotropy would be opened up by observing the strain and myosin dynamics across the whole embryo, beginning at the time when VF formation is initiated. Several questions can already be addressed with this analysis. Firstly, do TLR mutants resemble VF mutants? If so, this indicates that TLRs are involved in the mechanical feedback mechanism that is activated by the strain generated during VF formation. If not, are the early dynamics equivalent to WT and only diverge at later time points? This would support a role for TLRs in maintaining the myosin distribution rather than establishing it, as suggested in [91]. Alternatively, are the dynamics of strain and myosin rates qualitatively similar to WT embryos, but the proportionality, i.e. the feedback coefficient, is altered? If so, this would support the proposed possibility that TLRs are responsible for setting the strength of the feedback response, rather than mechanical feedback itself. Not only does answering these questions help bridge our results with those from previous works, but also clearly demonstrates the importance of dynamic, global analyses of morphogenesis, without which distinguishing between these possibilities is impossible without many additional experiments.

The next area for further study is to uncover the pathway responsible for strain based myosin recruitment. Besides candidates implicated in the current literature, our results offer some insights into potential mediators. These two sources are important to help narrow down an otherwise inexhaustive pool of candidates. Firstly, our results indicate that the molecule mediating this response is responding to strain rather than tension, which has instructive implications for the nature of the sensor. Some proteins have been shown to be tension sensing molecules, such as myosin VI[56] and alpha-catenin[99]. Critically, these proteins effectively have two states: a tension activated “on” state and an inactive “off” state. In the case of alpha-catenin, these states are distinguished by the folding and unfolding of the protein. When the

tension across the alpha-catenin protein is insufficient, the domains remain associated, sequestering binding sites. However, when the tension surpasses this threshold, the protein unfolds, revealing the cryptic binding sites, which are now available to form interactions with the proteins that mediate the downstream response. Therefore, the response is binary, whereas we measure a continuous response. This can be seen in the optogenetic experiments, where the induced strain produces a gradient of myosin accumulation from the boundary of activation. In a tension-based response, we would instead expect to observe a region close to the activation, in which the tension generated by the activation is sufficient to activate the response, and a sharp drop off at the distance from the activation at which the dampening by friction lowers the effective tension below the response threshold[100]. Consequently, we can confidently eliminate any proteins that mediate a mechanical feedback response through conformational changes or similar mechanisms.

Instead, strain based mechanical feedback could act through previously suggested mechanisms, such as cadherin dilution[101]. In this model, cadherin molecules inhibit myosin accumulation, and therefore when the density of cadherin molecules is reduced due to dilution from junction stretching, myosin accumulates on the stretched junction. However, the timescale measured in the associated work is an order or magnitude greater than that measured here (5 minutes compared to 30 seconds), and therefore seems unlikely to be consistent with the mechanical recruitment mechanism we have characterized in this system. Additionally, we note that the method of inducing strain (squeezing the embryo) is less developmentally relevant, making the results difficult to interpret.

Nevertheless, other membrane associated proteins could mediate the mechanical feedback response via an analogous mechanism. For example, a dilution mechanism could

explain how TLRs are involved in myosin recruitment: if TLRs prevent myosin accumulation rather than promote it, then decreases in TLR density due to cell edge stretching would lead to increased myosin on those junctions. This would further explain how uniform cellular distribution of TLRs can lead to anisotropic myosin, as the strain stretching cell edges is anisotropic.

Finally, the time scale measured in our experiments, both in the single edge analysis and optogenetic perturbations, gives an approximate range of the total time the signaling cascade activating myosin should take. Protein phosphorylation has been measured to be on the order of 10-30 seconds. This would be consistent with a pathway that is only one or two steps removed from myosin activation. For example, the mechanism could act through Rho, which phosphorylates ROK, which in turn phosphorylates the regulatory light chain, activating myosin. If the strain sensing mechanism is directly upstream of Rho activation, then this pathway could fit within the measured time scales. While Rho has been implicated in a mechanosensitive process for myosin recruitment in cell culture[56], supporting Rho as a candidate to mediate the mechanism identified here, the specific force sensitive component of the pathway is not conserved in *Drosophila*[102]. Therefore, it is still possible that the Rho is the component of the pathway upstream of myosin activation, the force sensing mechanism is likely different. Other possibilities that fit within the criteria outlined should be thoroughly examined, as there are several ways to activate myosin and unknown possibilities for strain sensing. Nevertheless, identifying individual components in the pathway will help narrow down the candidate pool based on known and suspected protein activity and interactions. Finally, we note that although it is not expected due to the surplus of myosin in the cytoplasmic pool, the measured time scale nevertheless thoroughly eliminates any possibility of a

mechanism acting at the level of transcription or translation of myosin or any upstream regulators.

Testing a potential role of candidate proteins in mechanical feedback can be accomplished in a few ways. If genetic mutants are characterized and develop normally through VF formation, then strain and myosin dynamics can be characterized in the mutant background. For a protein to play a role in mechanical feedback, we would expect the mutant to form the VF normally but have a myosin profile and rate of GBE similar to that of *twist* mutants. Although one might expect for the strain profile to be unchanged in this scenario, the myosin recruited as a result of strain further contributes to strain generation, and therefore, the strain profile would likely be reduced, although perhaps not nearly as much as in *twist* mutants. Other options when genetic mutants are not available include RNAi or chemical inhibitors, although they are somewhat less desirable options. A second approach, ideally in combination with the first, is to use fluorescently tagged protein candidates and observe the response to optogenetic perturbations as we've done with myosin. Because the opto-construct is activated by 488 nm light, suitable fusions are limited to those with red or far-red fluorescent proteins. Furthermore, this technique is only useful for proteins that change their localization or density when mechanical feedback is activated. It may be that only the activity of the mediator(s) is affected, in which case an activity biosensor would be required. These are available in some cases, as with Rho biosensors, but the availability for the full candidate pool is likely limited. Nevertheless, most of the candidate proteins should have at least one option available and additional tools can be produced, if not already in progress. With this approach, the proteins involved in the mechanism described here can be identified, though not without substantial effort. For that reason, the task falls to those who would continue this work.

6.3 Closing thoughts

Finally, a direction of great interest is to move beyond *Drosophila* to determine the generality of such a mechanical feedback mechanism. In this system, mechanical feedback is activated by a process of tissue invagination to affect a convergent extensive process. These general morphogenetic movements are common to many developmental systems across species[103,104], suggesting that similar mechanisms may be at work in the development of animals in general. Beyond that, the fact that the various morphogenetic movements are not occurring in isolation, but rather in an integrated system, remains a general principle for all of development, arguing for a more global view of development. Consequently, there are many contexts in which such a mechanical feedback mechanism may play an important role in the processes involved and a global approach can help identify such situations. Therefore, our findings in the fruit fly can help us bridge the gaps in our knowledge of the development of other species, particularly those whose embryonic development is not accessible to experimentation such as humans. A number of common human developmental defects have known connections to genetic mutations, yet out understanding of the misregulated process is often lacking. An appreciation for the importance of mechanics, dynamics, and a glocal approach can guide our understanding of these defects and contribute to a more holistic view of the developmental program.

Appendix:

A1. Light sheet microscopy

A1.1 Mu-Vi SPIM

The Mu-Vi SPIM consists of 2 excitation arms and 2 imaging arms. Laser lines (488 nm and 561 nm OBIS LX Coherent, 941 nm Chameleon Vision II laser system, Coherent Inc.) are coupled with a custom-built laser combiner consisting of dichroic mirrors on kinematic mirror mounts and routed through the optical path feeding into the imaging arms of the microscope. A 50/50 beam splitter (Omega Optical Inc.) optimized for the wavelengths used (488 nm, 561 nm, 941 nm) splits the beams into the two opposing imaging arms. Each illumination arm consists of a galvanometric mirror (Cambridge Technologies), which produces the digital light sheet, a scan lens (Sill Optics), tube lens (200 mm focal length), and a water dipping objective to focus the beam (CFI Plan Fluor 10x, NA 0.3, Nikon). This setup produces a digital light sheet with a waist of 1 um, centered on the location of the sample. Oriented at 90 degrees to the illumination arms are a pair of imaging arms, each consisting of a high NA detection objective (APO LWD 25x, NA 1.1, Nikon), filter wheel (Lambda, Sutter Instruments) with emission filters (FF01-542/27-25, FF01-609/62-25,BLP01-568R-25, BLP01-664R-25, Semrock), and sCMOS camera (Hamamatsu ORCA-Flash 4.0 V3). A custom script run through micromanager is used to sync excitation, translation and rotation of the sample, and image acquisition[105].

A1.2 Sample preparation

For imaging of *Drosophila* embryos with MuVi SPIM, embryos are collected on agar plates from collection cages populated with adults of the desired genotype. Embryos of the correct

stage (typically late cellularization) are selected using Halocarbon oil for visualization on a dissecting scope. Excess oil is removed from the embryo, and the embryo is dechorionated in a 50% bleach in water solution. Embryos are removed from bleach just before the chorion fully ruptures (approx. 1 minute) and the chorion is removed fully by subsequent drying and rehydrating. Once the chorion is fully removed, as evidenced by the change in optical properties of the embryo as well as the absence of the dorsal appendages, the embryo is maintained in a small amount of water to prevent desiccation. During this time, the agarose cylinder is prepared. The embryo is mounted in 1% low melting point (LMP) agarose with multispectral fluorescent beads.

Embryos for optogenetic experiments are prepared in the same manner, with the exception that a dissection scope with a red filter on the light source was used in an otherwise completely dark room for selection and mounting. This prevents any activation of the optogenetic construct during experiment preparation.

A1.3 Image acquisition

Typical imaging parameters are as follows: embryos are imaged from 4 positions at 45 degrees rotation from each of the detection objectives, totaling 8 views. Exposure time is 1 ms, and typical laser powers used are 0.5-2 mW. For each view, the embryo is imaged at 1.2-1.5 um Z steps. With these parameters, acquisition of a single time points in completed in approximately 18 seconds. Time resolution is 30 seconds for all optogenetic experiments and 60 secs for *twist* and *snail* datasets.

For confocal datasets, embryos were prepared as above for selection and dechorionation. Dechorionated embryos were positioned on a No. 1 35 mm glass bottom dish (MatTek) in water and imaged on a Leica SP8 confocal microscope (HC PL Apo CS2 40x, NA 1.1, Water, Leica Inc.). 9 z stacks containing the adherens junctions were taken at 1 micron intervals with a lateral resolution of 0.08 microns. Image stacks were acquired every 4.6 seconds beginning at the end of cellularization through the fast phase of GBE. Because the region included in the field of view is effectively planar, a MIP of the imaged stacks is used for analysis without the need for surface fitting.

A1.4 Data fusion

Fluorescent beads (Fluoresbrite multifluorescent 0.5-μm beads 24054, Polysciences Inc.) serve as fiducial markers for point matching and data registration. The Fiji plugin "Multiview-reconstruction" from Stephen Preibisch is used for data registration[80] and deconvolution[81]. A difference of a gaussian filter is used for bead detection to automatically locate beads in the image volume based on size and intensity. Bead positions in each of the 8 views are matched using the fast 3D geometric hashing (rotation invariant) algorithm with all-to-all time point matching (global optimization). Views are then registered based on bead matching using an affine transformation model regularized to a rigid model with lambda value of 0.10. Registered views were then fused and deconvolved with an efficient Bayesian iteration. The PSF estimation used for deconvolution was extracted from the beads. Resulting images have an isotropic resolution of 0.2619 um.

A2. Pullbacks

A2.1 Spherelike fitter

Primary pullbacks were generated according the the procedure described in [82]. Briefly, the 3D image stack of a single timepoint is imported into ilastik[83]. A pixel classification workflow is used to train the background and sample as two distinct classes. From the probability matrix, a point cloud is defined as the boundary between background and foreground classes, according to threshold values set in the ImSAnE script. This results in a very good approximation of the 3D embryo surface. The detected surface is then fit by an ellipse that varies in X and Y radii, centerpoint, and eccentricity with the embryo long axis. The resulting fitted surface is projected onto a plane using a cylinder projection. This projection method results in faithful projection of the trunk region, where our analysis is focused. All calculations for downstream analysis are corrected using a metric tensor[82]. The fitted surface is shifted to a slightly basal position from the apical surface, defined the center layer. This layer is normally evolved by 2 pixels for 25 steps inward (toward the embryo center) and outward (toward the image boundaries) to produce 51 total layers roughly centered about the adherens junctions,

forming a 3D Z stack with a depth of approximately 26 um. This Z stack is then used for the subsequent fitting step.

A2.1 Planar fitter

Small deviations in the true embryo surface from the fitted surface result in a central image layer that sometimes passes slightly above (apically) or below (basally) the adherens junctions. In order to minimize the number of pullback layers analyzed, we implement a secondary fitting step. The first step is analogous to the spherelike fitter: the Z stack is uploaded to a pixel classification workflow in Ilastik. Background and foreground are trained as separate classes, and the resulting predictions are imported into the ImSAne planar fitter script. A point cloud of the embryo surface is detected as before and fitted with a thin plate spline fit. This fitted surface is shifted to the level of the adherens junctions and then normally evolved by 2 pixels for 7 layers above and below the central layer. From these pullbacks, the 6 layers best containing the adherens junctions are selected.

A2.2 Final MIPs

From the 15 layers resulting from the planar fitting step, the 6 layers containing the majority of the signal corresponding to the adherens junctions are selected. A maximum intensity projection (MIP) is made from these layers, and used in all subsequent analysis. This final MIP therefore represents a total depth of 2.6 microns just below the apical surface.

A3. Segmentation

A single pullback layer approximately 5 um below the adherens junctions from the secondary fitting step is loaded into an ilastik Auto-context (2 stage) work flow. In the first stage, a pixel classification algorithm is trained for three classes: high myosin (junctions), low myosin (cytoplasm), and background (nuclei). From the output of this first classification, two subclasses are defined: junctions and cell body (cytoplasm plus nuclei). The predictions from this algorithm are inoput into a custom MatLab script (Sebastian Streichan) that identifies

individual edges in each frame, matched edges between frames based on centroids of the enclosed cells and tracks the edge length and myosin signal over time.

A4. Quantitative analysis

A4.1 Strain rate

Strain rate is measure based on the segmentation of the myosn signal described above. The end points of junctions are tracked over time, from which the junction length is measured at each time point. During the period studied (VF formation and early GBE) the change in junction length is linear (See figure 3.2). Therefore, strain rate is calculated as the slope of the line fit through this period of linearity.

A4.2 Myosin junctional accumulation

Myosin junctional accumulation is measures as the ratio of the difference between the junctional and cytoplasmic signal normalized to the cytoplasmic signal ($I_{junction} - I_{cytoplasm}/I_{cytoplasm}$). The cytoplasmic signal is determined using a top hat transformation with a disc with radius of approximately cell size as the structuring element. The myosin signal is then calculated as the ratio of the image intensity to the cytoplasmic intensity, giving a measure of the myosin signal in units of the cytoplasmic intensity. This measure therefore has a value of 1 in the cytoplasm and greater than one on the junctions. For simplicity, we then subtract 1 from this ratio, such that the junctional accumulation in the cytoplasm is 0 and greater than zero on the junctions. To determine myosin rate, junctional myosin accumulation is measured over time in defined regions, for example diving the embryo into bins along the D-V axis. As with strain rate, we observe that the increase in junctional myosin accumulation is linear during the period studied (see Figure 3.6). Myosin rate is similarly obtained by measuring the slope of the line that fits this linear regime.

A4.3 Rate of GBE

Velocity of tissue flows are measured from pullbacks over time using particle image velocimetry (PIV)[98]. PIV fields from multiple wildtype and mutant embryos were time aligned and an average flow field was calculated for each genotype. The average velocity per time point was calculated from the resulting ensemble averaged flow[16].

A5. Optogenetics

A5.1 Construct

The optogenetic construct utilized in this work consists of two parts: 1) a plasma membrane anchored GFP fused to CIBN[85] and 2) Cry2 fused to RhoGEF2[86]. Both constructs are under UAS control and therefore are not expressed in the absence of GAL4. For expression in the embryo, we utilize an oskar>GAL4 construct. This results in adequate accumulation of the optogenetic fusion proteins in the embryo to allow activation that does not seem to be impeded by abundance of either component of the system. For visualization of myosin, a fly line expressing both the osk>GAL4 construct and a mCherry tagged *spaghetti squash* was crossed to the line carrying the optogenetic constructs.

A5.2 Maintenance and crosses

Fly lines are maintained in normal conditions. Virgin females were selected from pmGFP:CIBN;Cry2-RhoGEF2 flies and crossed to sqh:Cherry/Cyo;osk>Gal4/TM3 males. Once virgin female and male flies are placed in the vial together, the vial is moved to dark conditions. All sorting is then conducted in the dark using only red light sources. From the progeny, female flies of the correct genotype (pmGFP:CIBN/sqh:Cherry; Cry2:RhoGEF2/osk>Gal4) are selected for by selecting against Cyo and TM3. Females are placed into an embryo collection cage with males of any genotype (although the same genotype was selected for simplicity). Once populated, the embryo cage is returned to the dark incubator.

A5.3 Activation

Activation is achieved using a tunable femto-second laser set to 940 nm and relies on the two-photon effect. To activate in a particular region, the optimal embryo position was determined before the experiment begins. This position is stored for the later activation. Before activation, several timepoints, typically 10 or 5 minutes are recorded to allow time alignment of the embryo as well quantification of myosin and strain rates before the perturbation. Once the pre-activation imaging acquisition is completed, the embryo is moved to the predetermined position. The femto-second laser shutter is opened for the desired activation length, which varies with experiment type. For parallel activations, the shutter is opened, and the embryo is translated about 5 z steps (of 1 micron each), dwelling at each position for 3 seconds, with the shutter open. This results in a total activation time of about 18 seconds and an activation width of about 5 microns. For head activation experiments, the protocol is modified somewhat, and the activation period is significantly longer to allow larger strain generations. Pre-activation acquisition is equivalent to the parallel activation. To activate, the embryo is lowered with the manual X stage until only the head region is within the light sheet. Then, the embryo is activated in a manner very similar to the normal imaging routine, with a few adjustments. Firstly, rather than the 4 positions (8 views) used for imaging, 4 additional positions are specified for a total of 8, such that the embryo is imaged every 22.5 degrees. Secondly, the Z step is reduced to 0.5 micron, and the exposure is set to 10 ms. These settings help ensure a relatively uniform activation in the head. The total acquisition time using these imaging parameters is 180 seconds. The full experimental procedure is as follows: 1) pre-activation imaging 2) lower embryo 3) open shutter and begin activation acquisition 4) close shutter, return embryo to initial position, and 5) run post-activation acquisition. Post- activation acquisition uses settings equivalent to the pre-activation and all other imaging (See Imaging in Lightsheet microscopy above) and typically runs for the 20 – 30 minutes following activation.

Bibliography

1. Niisslein-Volhard, C., Wieschaus, E. & Kluding, H. Roux's Archives of Developmental Biology Mutations affecting the pattern of the larval cuticle in Drosophila melanogaster I. Zygotic loci on the second chromosome. *Arch Dev Biol* **193**, 267–282 (1984).

2. Anderson, K. v, Bokla, L. & Niisslein-Volhard, C. Establishment of Dorsal-Ventral Polarity in the Drosophila Embryo: The Induction of Polarity by the To// Gene Product. *Cell* **42**, 791–798 (1985).

3. Roth, S., Stein, D. & Niisslein-Volhard, C. A Gradient of Nuclear Localization of the dorsal Protein Determines Dorsoventral Pattern in the Drosophila Embryo. *Cell* **59**, 1189–1202 (1989).

4. Rusch, J. & Levine, M. Threshold responses to the dorsal regulatory gradient and the subdivision of primary tissue territories in the Drosophila embryo. *Current Opinion in Genetics and Development* **6**, 416–423 (1996).

5. Schüpbach, T. Germ line and soma cooperate during oogenesis to establish the dorsoventral pattern of egg shell and embryo in Drosophila melanogaster. *Cell* **49**, 699–707 (1987).

6. Montell, D. J., Keshishian, H. & Spradling, A. C. Laser ablation studies of the role of the Drosophila oocyte nucleus in pattern formation. *Science (1979)* **254**, 290–293 (1991).

7. The Drosophila dorsoventral patterning gene gurken produces a dorsally localized RNA and encodes a TGF alpha-like protein - PubMed. https://pubmed.ncbi.nlm.nih.gov/7691414/.

8. Nüsslein-Volhard, C., Frohnhöfer, H. G. & Lehmann, R. Determination of Anteroposterior Polarity in Drosophila. *Science (1979)* **238**, 1675–1681 (1987).

9. Papatsenko, D. & Levine, M. The Drosophila Gap Gene Network Is Composed of Two Parallel Toggle Switches. *PLoS ONE* **6**, 21145 (2011).

10. Rivera-Pomar, R. & Jäckle, H. From gradients to stripes in Drosophila embryogenesis: filling in the gaps. *Trends in Genetics* **12**, 478–483 (1996).

11. Umulis, D., O'connor, M. B. & Othmer, H. G. 2 Robustness of Embryonic Spatial Patterning in Drosophila melanogaster. (2008) doi:10.1016/S0070-2153(07)81002-7.

12. Paré, A. C. *et al.* A positional Toll receptor code directs convergent extension in Drosophila. *Nature* **515**, 523–527 (2014).

13. Johnson Miller, C. & Davidson, L. A. The interplay between cell signalling and mechanics in developmental processes. *Nature Publishing Group* (2013) doi:10.1038/nrg3513.

14. Serwane, F. *et al.* In vivo quantification of spatially-varying mechanical properties in developing tissues.

15. Heer, N. C. *et al.* Actomyosin-based tissue folding requires a multicellular myosin gradient. *Development* **144**, 1876 (2017).

16. Streichan, S. J., Lefebvre, M. F., Noll, N., Wieschaus, E. F. & Shraiman, B. I. Global morphogenetic flow is accurately predicted by the spatial distribution of myosin motors . *Elife* **7**, e27454 (2018).

17. Lecuit, T. & Lenne, P.-F. Cell surface mechanics and the control of cell shape, tissue patterns and morphogenesis. *Nature Reviews Molecular Cell Biology* **8**, 633–644 (2007).

18. Lenne, P.-F. *et al.* Physical Biology Roadmap for the multiscale coupling of biochemical and mechanical signals during development Roadmap for the multiscale coupling of biochemical and mechanical signals during development. *Phys. Biol* **18**, 41501 (2021).

19. Campàs, O. A toolbox to explore the mechanics of living embryonic tissues. *Semin Cell Dev Biol* **55**, 119–130 (2016).

20. Polacheck, W. J. & Chen, C. S. Measuring cell-generated forces: a guide to the available tools. *Nature Methods 2016 13:5* **13**, 415–423 (2016).

21. Sugimura, K., Lenne, P. F. & Graner, F. Measuring forces and stresses in situ in living tissues. *Development* **143**, 186–196 (2016).

22. Kasza, K. E. & Zallen, J. A. Dynamics and regulation of contractile actin-myosin networks in morphogenesis. *Curr Opin Cell Biol* **23**, 30–8 (2011).

23. Levayer, R. & Lecuit, T. Biomechanical regulation of contractility: Spatial control and dynamics. *Trends in Cell Biology* **22**, 61–81 (2012).

24. Murrell, M., Oakes, P. W., Lenz, M. & Gardel, M. L. Forcing cells into shape: the mechanics of actomyosin contractility. *Nature Publishing Group* (2015) doi:10.1038/nrm4012.

25. Lecuit, T., Lenne, P. F. & Munro, E. Force generation, transmission, and integration during cell and tissue morphogenesis. *Annu. Rev. Cell Dev. Biol.* **27**, 157–184 (2011).

26. Sellers, J. R. Myosins: a diverse superfamily. *Biochimica et Biophysica Acta (BBA) - Molecular Cell Research* **1496**, 3–22 (2000).

27. Heissler, S. M. & Sellers, J. R. Myosins. *Encyclopedia of Cell Biology* **2**, 597–607 (2016).

28. Niederman, R. & Pollard, T. D. Human platelet myosin. II. In vitro assembly and structure of myosin filaments. *Journal of Cell Biology* **67**, 72–92 (1975).

29. Verkhovsky, A. B. & Borisy, G. G. Non-sarcomeric mode of myosin II organization in the fibroblast lamellum. *Journal of Cell Biology* **123**, 637–652 (1993).

30. Martin, A. C. Pulsation and stabilization: Contractile forces that underlie morphogenesis. *Developmental Biology* **341**, 114–125 (2010).

31. Houdusse, A. & Sweeney, H. L. How Myosin Generates Force on Actin Filaments The Product-Release Steps on Actin. *Trends in Biochemical Sciences* **41**, (2016).

32. Jung, H. S., Komatsu, S., Ikebe, M. & Craig, R. Head-Head and Head-Tail Interaction: A General Mechanism for Switching Off Myosin II Activity in Cells. *Molecular Biology of the Cell* **19**, 3234–3242 (2008).

33. Gonzalcz-Noriega, J., Grubb, A., Talkad, J. H. & Sly, V. *L£ II ERSTO NATURE Light-chain phosphorylation controls the conformation of vertebrate non-muscle and smooth muscle myosin molecules*. *J. Cell Bioi* vol. 255 (1980).

34. Somlyo, A. P. & Somlyo, A. v. Signal transduction by G-proteins, Rho-kinase and protein phosphatase to smooth muscle and non-muscle myosin II. *The Journal of Physiology* **522**, 177–185 (2000).

35. Matsumura, F. Regulation of myosin II during cytokinesis in higher eukaryotes. *Trends in Cell Biology* **15**, 371–377 (2005).

36. Amano, M. *et al.* Phosphorylation and Activation of Myosin by Rho-associated Kinase (Rho-kinase). *Journal of Biological Chemistry* **271**, 20246–20249 (1996).

37. Takai, Y., Sasaki, T., Tanaka, K. & Nakanishi, H. Rho as a regulator of the cytoskeleton. *Trends in Biochemical Sciences* **20**, 227–231 (1995).

38. Watanabe, N., Kato, T., Fujita, A., Ishizaki, T. & Narumiya, S. Cooperation between mDia1 and ROCK in Rho-induced actin reorganization. *Nature Cell Biology* **1**, 136 (1999).

39. Kühn, S. & Geyer, M. Formins as effector proteins of Rho GTPases. *Small GTPases* **5**, (2014).

40. Hodge, R. G. & Ridley, A. J. Regulating Rho GTPases and their regulators. *Nature Reviews Molecular Cell Biology 2016 17:8* **17**, 496–510 (2016).

41. Rossman, K. L., Der, C. J. & Sondek, J. GEF means go: turning on RHO GTPases with guanine nucleotide-exchange factors. *Nature Reviews Molecular Cell Biology* **6**, 167–180 (2005).

42. Reymann, A. C. *et al.* Actin Network Architecture Can Determine Myosin Motor Activity. *Science* **336**, 1310 (2012).

43. Structure and Organization of Actin Filaments - The Cell - NCBI Bookshelf. https://www.ncbi.nlm.nih.gov/books/NBK9908/.

44. Pollard, T. D. Regulation of Actin Filament Assembly by Arp2/3 Complex and Formins. *http://dx.doi.org/10.1146/annurev.biophys.35.040405.101936* **36**, 451–477 (2007).

45. Afshar, K., Stuart, B. & Wasserman, S. A. Functional analysis of the Drosophila diaphanous FH protein in early embryonic development. *Development* **127**, 1887–1897 (2000).

46. Coravos, J. S. & Martin, A. C. Apical Sarcomere-like Actomyosin Contracts Nonmuscle Drosophila Epithelial Cells. *Developmental Cell* **39**, 346–358 (2016).

47. Stachowiak, M. R. *et al.* Mechanism of Cytokinetic Contractile Ring Constriction in Fission Yeast. *Dev Cell* **29**, 547 (2014).

48. Heer, N. C. & Martin, A. C. Tension, contraction and tissue morphogenesis. *Development* **144**, 4249–4260 (2017).

49. Reymann, A. C. *et al.* Actin Network Architecture Can Determine Myosin Motor Activity. *Science* **336**, 1310 (2012).

50. Ennomani, H. *et al.* Architecture and Connectivity Govern Actin Network Contractility. *Current Biology* **26**, 616–626 (2016).

51. Halbleib, J. M. & Nelson, W. J. Cadherins in development: cell adhesion, sorting, and tissue morphogenesis. (2006) doi:10.1101/gad.1486806.

52. Rimm, D. L., Koslov, E. R., Kebriaei, P., Cianci, C. D. & Morrow, J. S. α1(E)-catenin is an actin-binding and -bundling protein mediating the attachment of F-actin to the membrane adhesion complex. *Proc Natl Acad Sci U S A* **92**, 8813–8817 (1995).

53. Goldmann, W. H. *Mechanosensation: A basic cellular process*. *Progress in Molecular Biology and Translational Science* vol. 126 (Elsevier Inc., 2014).

54. Luo, T., Mohan, K., Iglesias, P. A. & Robinson, D. N. Molecular mechanisms of cellular mechanosensing. *Nature Materials* **12**, 1064–1071 (2013).

55. Wozniak, M. A. & Chen, C. S. Mechanotransduction in development: a growing role for contractility. *Nature Reviews Molecular Cell Biology* **10**, 34–43 (2009).

56. Acharya, B. R. *et al.* A Mechanosensitive RhoA Pathway that Protects Epithelia against Acute Tensile Stress. *Developmental Cell* **47**, 439-452.e6 (2018).

57. Duda, M. *et al.* Polarization of Myosin II Refines Tissue Material Properties to Buffer Mechanical Stress. *Developmental Cell* **48**, 245 (2019).

58. Fernandez-Gonzalez, R., Simoes, S. de M., Röper, J.-C., Eaton, S. & Zallen, J. A. Myosin II dynamics are regulated by tension in intercalating cells. *Dev Cell* **17**, 736–43 (2009).

59. Bailles, A. *et al.* Genetic induction and mechanochemical propagation of a morphogenetic wave. *Nature* **572**, 467–473 (2019).

60. Abreu-Blanco, M. T., Verboon, J. M. & Parkhurst, S. M. Cell wound repair in Drosophila occurs through three distinct phases of membrane and cytoskeletal remodeling. *The Journal of Cell Biology* **193**, 455 (2011).

61. Early Drosophila Development - Developmental Biology - NCBI Bookshelf. https://www.ncbi.nlm.nih.gov/books/NBK10081/.

62. Campos-Ortega, J. A. (José A. & Hartenstein, V. The embryonic development of Drosophila melanogaster. 405 (1997).

63. Leptin, M. twist and snail as positive and negative regulators during Drosophila mesoderm development. *Genes Dev* **5**, 1568–1576 (1991).

64. Dawes-Hoang, R. E. *et al.* folded gastrulation, cell shape change and the control of myosin localization. *Development* **132**, 4165–4178 (2005).

65. Parks, S. & Wieschaus, E. The drosophila gastrulation gene concertina encodes a Gα-like protein. *Cell* **64**, 447–458 (1991).

66. Kölsch, V., Seher, T., Fernandez-Ballester, G. J., Serrano, L. & Leptin, M. Control of drosophila gastrulation by apical localization of adherens junctions and RhoGEF2. *Science (1979)* **315**, 384–386 (2007).

67. Barrett, K., Leptin, M. & Settleman, J. The Rho GTPase and a Putative RhoGEF Mediate a Signaling Pathway for the Cell Shape Changes in Drosophila Gastrulation. *Cell* **91**, 905–915 (1997).

68. Leptin, M. Drosophila Gastrulation: From Pattern Formation to Morphogenesis. *Annu Rev Cell Dev Biol* **11**, 189–212 (1995).

69. Irvine, K. D. & Wieschaus, E. Cell intercalation during Drosophila germband extension and its regulation by pair-rule segmentation genes. **841**, 827–841 (1994).

70. Bertet, C., Sulak, L. & Lecuit, T. Myosin-dependent junction remodelling controls planar cell intercalation and axis elongation. *Nature* **429**, 667–671 (2004).

71. Rickoll, W. L. & Counce, S. J. Morphogenesis in the embryo ofDrosophila melanogaster ? Germ band extension. *Wilhelm Roux's Archives of Developmental Biology* **188**, 163–177 (1980).

72. Paré, A. C. & Zallen, J. A. Cellular, molecular, and biophysical control of epithelial cell intercalation. *Current Topics in Developmental Biology* **136**, 167–193 (2020).

73. Butler, L. C. *et al.* Cell shape changes indicate a role for extrinsic tensile forces in Drosophila germ-band extension. *Nature Cell Biology* **11**, 859–864 (2009).

74. Lye, C. M. *et al.* Mechanical Coupling between Endoderm Invagination and Axis Extension in Drosophila. *PLOS Biology* **13**, e1002292 (2015).

75. Zusman, S. B. & Wieschaus, E. F. Requirements for zygotic gene activity during gastrulation in Drosophila melanogaster. *Developmental Biology* **111**, 359–371 (1985).

76. Sweeton, D., Parks, S., Costa, M. & Wieschaus, E. Gastrulation in Drosophila : the formation of the ventral furrow and posterior midgut invaginations. **789**, 775–789 (1991).

77. Noll, N., Mani, M., Heemskerk, I., Streichan, S. J. & Shraiman, B. I. Active tension network model suggests an exotic mechanical state realized in epithelial tissues. *Nature Physics* **13**, 1221–1226 (2017).

78. Krzic, U., Gunther, S., Saunders, T. E., Streichan, S. J. & Hufnagel, L. Multiview light-sheet microscope for rapid in toto imaging. *Nature Methods* **9**, 730–733 (2012).

79. Medeiros, G. de *et al.* Confocal multiview light-sheet microscopy. *Nature Communications 2015 6:1* **6**, 1–8 (2015).

80. Preibisch, S., Saalfeld, S., Schindelin, J. & Tomancak, P. Software for bead-based registration of selective plane illumination microscopy data. *Nature Methods 2010 7:6* **7**, 418–419 (2010).

81. Preibisch, S. *et al.* Efficient Bayesian-based multiview deconvolution. *Nature Methods 2014 11:6* **11**, 645–648 (2014).

82. Heemskerk, I. & Streichan, S. J. Tissue cartography: compressing bio-image data by dimensional reduction. *Nature Methods* **12**, 1139–1142 (2015).

83. Berg, S. *et al.* ilastik: interactive machine learning for (bio)image analysis. *Nature Methods* doi:10.1038/s41592-019-0582-9.

84. Deisseroth, K. Optogenetics. *Nature Methods 2011 8:1* **8**, 26–29 (2010).

85. Guglielmi, G., Barry, J. D., Huber, W. & de Renzis, S. An Optogenetic Method to Modulate Cell Contractility during Tissue Morphogenesis. *Dev Cell* **35**, 646–60 (2015).

86. Izquierdo, E., Quinkler, T. & de Renzis, S. Guided morphogenesis through optogenetic activation of Rho signalling during early Drosophila embryogenesis. *Nature Communications* **9**, 2366 (2018).

87. Denk, W., Strickler, J. H. & Webb, W. W. Two-Photon Laser Scanning Fluorescence Microscopy. *Science (1979)* **248**, 73–76 (1990).

88. Rauzi, M., Lenne, P. F. & Lecuit, T. Planar polarized actomyosin contractile flows control epithelial junction remodelling. *Nature* **468**, 1110–1115 (2010).

89. D'Angelo, A., Dierkes, K., Carolis, C., Salbreux, G. & Solon, J. In Vivo Force Application Reveals a Fast Tissue Softening and External Friction Increase during Early Embryogenesis. *Current Biology* **29**, 1564-1571.e6 (2019).

90. Dierkes, K., Sumi, A., Solon, J. & Salbreux, G. Spontaneous Oscillations of Elastic Contractile Materials with Turnover. *Physical Review Letters* **113**, 148102 (2014).

91. Lefebvre, M. F., Claussen, N. H., Mitchell, N. P., Gustafson, H. J. & Streichan, S. J. Geometric control of Myosin-II orientation during axis elongation. *bioRxiv* 2022.01.12.476069 (2022) doi:10.1101/2022.01.12.476069.

92. Martin, A. C., Kaschube, M. & Wieschaus, E. F. Pulsed contractions of an actin–myosin network drive apical constriction. *Nature 2008 457:7228* **457**, 495–499 (2008).

93. Simpson, P. Maternal-Zygotic Gene Interactions during Formation of the Dorsoventral Pattern in Drosophila Embryos. *Genetics* **105**, 615 (1983).

94. Thisse, B., Stoetzel, C., Gorostiza-Thisse, C. & Perrin-Schmitt, F. Sequence of the twist gene and nuclear localization of its protein in endomesodermal cells of early Drosophila embryos. *The EMBO Journal* **7**, 2175 (1988).

95. Manning, A. J., Peters, K. A., Peifer, M. & Rogers, S. L. Regulation of epithelial morphogenesis by the G protein-coupled receptor mist and its ligand fog. *Sci Signal* **6**, ra98 (2013).

96. Kölsch, V., Seher, T., Fernandez-Ballester, G. J., Serrano, L. & Leptin, M. Control of drosophila gastrulation by apical localization of adherens junctions and RhoGEF2. *Science (1979)* **315**, 384–386 (2007).

97. Manning, A. J., Peters, K. A., Peifer, M. & Rogers, S. L. Regulation of Epithelial Morphogenesis by the G-Protein Coupled Receptor Mist and its Ligand Fog*. *Sci Signal* **6**, ra98 (2013).

98. Adrian, R. J. Twenty years of particle image velocimetry. *Experiments in Fluids* **39**, 159–169 (2005).

99. Ishiyama, N. *et al.* Force-dependent allostery of the α-catenin actin-binding domain controls adherens junction dynamics and functions. *Nature Communications 2018 9:1* **9**, 1–17 (2018).

100. Gustafson, H. J., Claussen, N., Renzis, S. de & Streichan, S. J. Patterned mechanical feedback establishes a global myosin gradient. *bioRxiv* 2021.12.06.471321 (2021) doi:10.1101/2021.12.06.471321.

101. Sumi, A. *et al.* Adherens Junction Length during Tissue Contraction Is Controlled by the Mechanosensitive Activity of Actomyosin and Junctional Recycling. *Developmental Cell* **47**, 453–463 (2018).

102. Garcia De Las Bayonas, A., Philippe, J. M., Lellouch, A. C. & Lecuit, T. Distinct RhoGEFs Activate Apical and Junctional Contractility under Control of G Proteins during Epithelial Morphogenesis. *Current Biology* **29**, 3370-3385.e7 (2019).

103. Heisenberg, C. P. & Bellaïche, Y. Forces in tissue morphogenesis and patterning. *Cell* **153**, 948–962 (2013).

104. Tada, M. & Heisenberg, C. P. Convergent extension: using collective cell migration and cell intercalation to shape embryos. *Development* **139**, 3897–3904 (2012).

105. Edelstein, A. D. *et al.* Advanced methods of microscope control using μManager software. *J Biol Methods* **1**, e10 (2014).